To the Graduate Council:

I am submitting herewith a dissertation written by Zhiyu Hu entitled "Thin Film Stress Studies Using Microcantilevers and Microcantilever Sensors." I have examined the final copy of the dissertation for form and content and recommend that it be accepted in partial fulfillment of the requirements for the degree of Doctor of Philosophy, with a major in Physics.

Robert J. Warmack, Major Professor

We have read this dissertation
and recommend its acceptance:

Marianne Breinig

William R. Hamel

Accepted for the Council:

Associate Vice Chancellor and
Dean of the Graduate School

THIN FILM STRESS STUDIES USING MICROCANTILEVERS AND MICROCANTILEVER SENSORS

A Dissertation

Presented for the

Doctor of Philosophy

Degree

The University of Tennessee, Knoxville

Zhiyu Hu

May 2000

Copyright © Zhiyu Hu, 2000

All rights reserved

DEDICATION

I would like to dedicate this dissertation to my parents,

Professor Wenguo Hu

and

Professor Ping Li

who have given me two lives:

a physical life and a life in physics.

The dedication is also for my lovely wife

Hongzhi Li

and our two beautiful daughters

Lydia Yawen and Liana Yaxin

who have sacrificed so much for me and their love is the foundation of my life.

ACKNOWLEDGMENTS

The last five years have been very important for my life, and many things have occurred during this period. The process of earning a Ph.D. has transformed me into a new person. It is not only about knowledge gained and laboratory work, but also about the changes of my life philosophy and my view of the world. There are many people who have offered me enormous help and support at different points. Without their help, it would have been impossible for me to accomplish what I have done. My gratitude towards them can hardly be expressed.

I wish to express my deep appreciation to my major professor, Dr. Robert J. (Bruce) Warmack, for his invaluable guidance, encouragement, patience and generous support throughout this study. I also would like to express my special thanks to Dr. Thomas G. Thundat for his generous advice and help during the completion of this dissertation. This dissertation could not be completed without their support. I have often wondered how I have been so fortunate to be able work with them.

I am very grateful for Drs. Marianne Breinig and William R. Hamel who graciously agreed to take their precious time, serving on my doctoral committee and offering many valuable suggestions. Appreciation is also extended to faculty members at the Department of Physics and Astronomy for their help during my studies and at difficult times. In particular, I would like to thank Drs. C. C. Shih, J. J. Quinn, A. Zucker, T. A. Callcott, W. M. Bugg, G. S. Canright, J. E. Parks and the department head, L. L. Riedinger, all of whom have helped me and taught me many things. I

would like to acknowledge experimental help and guidance at various stages of my experiments from Dr. P.I. Oden and other members of the Molecular Imaging Group, and to members of the Nanoscale Science and Devices Group at ORNL. The electronic sensor array was the result of another UTK dissertation project by R. L. Jones and was developed by Dr. C. L. Britton and other members of the Instrumentation and Controls division of ORNL. The use of this in my work is gratefully acknowledged.

Without the important education and guidance in my early years from my parents Wenguo Hu and Ping Li, who are professors in physics themselves, I would not have been exposed to the profound and wonderful world of physics. They have given me two lives: a physical life and a life in physics. My gratitude to my lovely wife and my best friend, Hongzhi Li, is hardly expressed by any words. Her unconditional love and encouragement always accompany me and has allowed me to overcome the most difficult times in my life. Our two beautiful daughters, Lydia Yawen and Liana Yaxin, are our sweet hearts and our angels who have always brought peace to me with smile and love. I am forever indebted to my brother Zhihua Hu and his wife Tao Yang for their loving support and guidance through hard times.

I would like to express my special thank to Mr. David L. Hedden who helped me read through this dissertation and for giving me much helpful advice concerning writing skills.

This research was supported by the Oak Ridge National Laboratory managed by UT-Battelle, LLC, for the U.S. Dept. of Energy under contract DE-AC05-

00OR22725. Support from the DOE Office of Biological and Environmental Research is gratefully acknowledged.

ABSTRACT

Microcantilever-based sensors have attracted much attention due to their potential as a platform for the development of myriad physical, chemical, and biological sensors. Studies have shown that thin bi-material microcantilevers undergo bending (deflection) due to differential stresses caused by exposure to such environments. Because of their very small spring constants (less than 0.01 N/m), microcantilevers are sensitive to stress differentials between the substrate and coating layer. Taking advantage of the ultra-high stress sensitivity of micrometer-sized microcantilevers, vapor adsorption on solid surfaces and adsorption-induced stress in thin metal films were investigated. Experimental results show that experimental systems can detect ppb (part-per-billion) or ppt (part-per-trillion) levels of hydrogen or mercury, respectively.

Thin, coated cantilevers undergo bending if they are exposed to various biological, chemical and physical environments. This bending is due to a differential surface stress caused by stress changes that are induced during the adsorption process. Depending on the nature of analyte-substrate interactions (adsorption or absorption), the adsorption-induced stress in the thin film can be expressed as either a surface stress (N/m) or a bulk stress (N/m^2). Such stress effects can be used to create extremely sensitive sensors and can be much larger than mass-induced frequency shifts of the fundamental resonance.

During the experiments, thin metal films were coated on one side of silicon or silicon-nitride based microcantilevers. Both optical and electrical cantilever deflection detection methods were employed. The two systems were selected to study two different interaction mechanisms:

1. Palladium-coated microcantilevers were employed to investigate the bulk-like absorption of hydrogen that diffuses into palladium and causes volume expansion.
2. Gold-coated microcantilevers were employed to study surface-like adsorption when mercury atoms adsorb onto the gold surface, thus changing the film stress.

Adsorption-induced stress on bi-material microcantilevers can produce bending, which can be related to gas or vapor concentration. The sensitivity of microcantilevers (Si or SiN based) is in the pico-newton range. Bi-material cantilevers can be used to measure thin film stress or as a chemical sensor platform using selected coatings.

For bulk-like absorption, vapors do not stop at the gas/solid interface on the film but actually penetrate the entire thickness of the film. An example is hydrogen adsorption in palladium that induces a volume expansion of the palladium film. The sensitivity of coated cantilevers is adjustable in a certain range by controlling the coating layer thickness.

For surface-like adsorption, both stress and resistance changes depend only upon the number of adsorbate atoms adsorbed on the adsorbent surface. Film

thickness has little effect on the sensitivity of coated cantilevers. An example is mercury adsorption onto a gold surface that causes a stress decrease.

Novel simultaneous cantilever bending and electrical resistance measurements indicate that adsorption onto or absorption into thin metal films can induce stress changes and resistance changes at different rates. These differences may or may not vary with gas or vapor concentration depending on the interaction mechanisms; and they imply more complex chemical reactions during the adsorption process than were known before this study. Additional investigations will be required to ascertain such details.

The investigation of mercury adsorption-induced stress on thin gold film described is believed to be the first complete work in this area. A surface adsorption model is proposed and shows excellent agreement with experimental data as well as that reported outside this dissertation. The model may serve as a guide for future studies in surface adsorption.

Bi-material microcantilevers have shown ultra-high stress sensitivity that may be utilized to study thin film stress or employed as a sensor platform. Investigations of the two-adsorption mechanisms help to provide a clear understanding of gas (or vapor) adsorption onto solid surfaces as well as the associated stress. Both theoretical models and experimental results could be used to design and improve the performance of microcantilever-based sensors. Effects of environmental influences, such as relative humidity and temperature, were also investigated.

Table of Contents

CHAPTER		PAGE
1	Introduction	1
	1.1 Microcantilevers and Microcantilever Sensors	1
	1.1.1 Microcantilevers and Atomic Force Microscope	1
	1.1.2 Microcantilevers Sensors	4
	1.2 Thin Film and Its Properties	6
	1.2.1 Preparation of Thin Film	6
	1.2.2 Mechanical Properties of Thin Films	7
	1.2.3 Electrical Properties of Metallic Thin Films	10
	1.3 Physical and Chemical Adsorption & Absorption	11
	1.4 The Scope of This Thesis	13
2	Theory	16
	2.1 Theory of Microcantilevers	16
	2.1.1 Simple Beam Theory and Cantilever Deflection	16
	2.1.2 Natural Frequency of Cantilever	18
	2.1.3 Volume Expansion of Bi-material Microcantilevers	22
	2.1.4 Thermal Effects	25
	2.2 Diffusion Theory	26
	2.2.1 Diffusion in Solids	26
	2.2.2 Diffusion Equations	29
	2.3 Stress and Surface Energy	32
	2.3.1 Stress and Strain	32
	2.3.2 Surface Energy and Surface Stress	34
3	Experimental	37
	3.1 Detection Methods	37
	3.1.1 Optical Cantilever Deflection Detection Technique	37

3.1.2 Electrical Detection Method and MUMPS Microcantilever 40
3.2 Thin Film Conductivity and Small Resistance Measurement 42
3.3 Experimental Setup 45
3.3.1 Gas Cell 45
3.3.2 Optical Detection Unit 48
3.3.3 Four-point Resistance Measurement Unit 48
3.3.4 Gas Mix and Control Unit 49
3.3.5 Data Acquisition System 52
3.4 Thin Film Preparation 53
3.5 MUMPS Chip Experiment 57
4 Analysis of Palladium-Hydrogen System 59
4.1 Introduction 59
4.1.1 Palladium and Hydrogen 60
4.1.2 Hydrogen Adsorption in Palladium 61
4.1.3 Hydrogen Diffusion in Palladium 63
4.2 Hydrogen Adsorption-Induced Stress in Palladium Film 67
4.2.1 Hydrogen Adsorption-Induced Cantilever Bending 69
4.2.2 Hydrogen Charge and Discharge Time 74
4.2.3 Coating Film Thickness Dependence 79
4.3 Hydrogen-Induced Resistance Changes in Palladium Film 83
4.4 Discussions 88
4.4.1 Hydrogen Adsorption in Palladium 88
4.4.2 Hydrogen Diffusion Time Delay and Palladium Surface Model 93
4.4.3 Hydrogen Detection and Microcantilever Sensors 103
5 Analysis of Gold-Mercury System 105
5.1 Introduction 105
5.1.1 Gold and Mercury 105
5.1.2 Mercury Adsorption on Gold Surface 107
5.2 Surface Stress and Cantilever Deflection 108
5.3 Surface Adsorption Model 112

5.4 Mercury Adsorption-Induced Stress in Gold Film 121
5.4.1 Mercury Adsorption-Induced Cantilever Bending 121
5.4.2 Cantilever Bending Rate and Adsorption-Induced Stress 125
5.4.3 Monolayer Coverage and Long Time Exposure 125
5.4.4 Gold Film Thickness Dependence 129
5.5 Mercury Adsorption-Induced Resistance Changes in Gold Film 129
5.6 Discussions 135
5.6.1 Mercury Adsorption on Gold Surface 135
5.6.2 Microcantilever Stress Sensor 139
6 Summary 141
Bibliography 144
Appendices 155
Appendix A Mathcad Evaluation for A Plate Sheet Diffusion 156
Appendix B Calculation of Cantilever Beam Natural Frequency 165
Appendix C Microcantilever Data Sheet 168
C.1 Ultralevers 168
C.2 Microlevers 169
Appendix D MUMPS Microcantilever and Readout System 172
Appendix E Properties of Palladium, Hydrogen, Mercury and Gold 175
Appendix F Surface Adsorption Model 176
F.1 Surface Adsorption Model 174
F.2 Surface Rejection Coefficient 175
VITA 179

List of Figures

FIGURE		PAGE
Figure 1.1	Array for microcantilevers with a human hair on the top.	2
Figure 1.2	An atomic sharp tip is mounted at the end of cantilever	2
Figure 1.3	Schematic diagram of a bi-material V-shaped cantilever beam	5
Figure 2.1	Uniformly loaded cantilever	17
Figure 2.2	Four normal mode vibration frequencies of a V-shaped cantilever	21
Figure 2.3	Theoretical curve of thickness dependence of a bi-material cantilever	24
Figure 2.4	Schematic of a jump step in interstitial diffusion	28
Figure 3.1	Schematic diagram of optical position-sensitive detection system	38
Figure 3.2	MUMPS microcantilever	41
Figure 3.3	Thin film four-point resistance measurement	44
Figure 3.4	Schematic diagram of experiment setup with both cantilever deflection unit and thin film 4-point resistance measurement unit	46
Figure 3.5	Laboratory instrument setup	47
Figure 3.6	Schematic diagram of gas mix and control setup	50
Figure 3.7	Coated microcantilevers	56
Figure 4.1	Hydrogen atom concentration distribution diagram at different time t in a plant sheet	65
Figure 4.2	Concentration distribution as a function of time at $x = d$ surface	66
Figure 4.3	Hydrogen diffusion in and our curves	68
Figure 4.4	Palladium-coated microcantilever bending in hydrogen gas	70
Figure 4.5	Cantilever bending amplitude and bending rate	73
Figure 4.6	Hydrogen charge and discharge rate	75
Figure 4.7	Bending respondents of cantilevers with different thickness of Pd film to 1% hydrogen	80
Figure 4.8	Bending rate sensitivity vs. thickness ratio	82
Figure 4.9	Typical Palladium resistance response to hydrogen	84
Figure 4.10	Palladium film resistance responses to hydrogen	85

Figure 4.11 Cantilever bending and resistance response to hydrogen..... 87
Figure 4.12 Cantilever deflection vs. low hydrogen concentration in the gas cell ... 89
Figure 4.13 Cantilever responses to hydrogen concentration in the gas cell 91
Figure 4.14 Relative adsorption-induced expansion coefficient vs. hydrogen concentration in the gas cell 92
Figure 4.15 Sputter coated Palladium film exposed to hydrogen at first time..... 94
Figure 4.16 Schematic of hydrogen diffusion model on the oxidized Palladium film surface 99
Figure 4.17 Palladium surface reactivation..... 101
Figure 5.1 Schematic of bending cantilever with the radius of curvature 110
Figure 5.2 A model of the surface adsorption process..... 114
Figure 5.3 Theoretical model of the adsorbate atoms accumulate on the adsorbent surface under a constant flow rate..... 120
Figure 5.4 Typical gold-coated cantilever bending responses to mercury vapor.. 122
Figure 5.5 Gold-coated cantilever is exposed to various mercury vapors..... 123
Figure 5.6 Gold-coated cantilever bending rate vs. mercury concentration 126
Figure 5.7 Long time mercury exposure of gold-coated cantilever..... 127
Figure 5.8 Gold thin film thickness dependences of mercury vapor..... 130
Figure 5.9 Gold-coated cantilever bending and resistance changes in mercury vapor..... 131
Figure 5.10 Gold-coated cantilever bending vs. gold film resistance change in mercury vapor 133
Figure 5.11 The response time differences between cantilever bending and gold film resistance change 134
Figure 5.12 Comprehensive MUMPS chip test for both hydrogen and mercury exposures 138
Figure 5.13. MUMPS microcantilevers coated with various thicknesses of palladium, gold and aluminum response to relative humidity..... 139
Figure A.1 Hydrogen atom concentration distributions at various times in a plate sheet..... 158

Figure A.2 Concentration distributions inside palladium film as a function of time t on the impermeable surface ($x = l$) for various concentrations at gas-solid surface ($x = d$). 160
Figure A.3 Hydrogen introduced into palladium when diffusion coefficients vary with concentrations 162
Figure A.4 Hydrogen diffusion-out palladium when diffusion coefficients vary with concentrations 164
Figure B.1 Cantilever deflection 165
Figure C.1 Ultralever diagram 168
Figure C.2 Microlever diagram 169
Figure D.1 MUMPS chip and readout circuit 172
Figure F.1 Surface rejection coefficient vs. the total exposure time 178

List of Tables

FIGURE		PAGE
Table 1.1	Thin film preparation methods	8
Table 4.1	Hydrogen charge/discharge time	78
Table C.1	Ultralever Properties	168
Table C.2	Microlever Properties	169
Table D.1	Dimensions of MUMPS cantilever	170
Table E.1	Properties of palladium, hydrogen, mercury and gold	173

Chapter 1

INTRODUCTION

1.1 Microcantilevers and Microcantilever Sensors

1.1.1 Microcantilevers and Atomic Force Microscope

The microcantilever was first used as a scanning probe in the atomic force microscope (AFM) or scanning force microscope (SFM), which was introduced by Binnig et al. in 1986. [1-3] The original hand fabricated wire cantilevers gave way to micro-fabricated foils making these instruments a practical reality. Like the scanning tunneling microscope (STM), the SFM was used to investigate the topography of various surfaces at atomic level resolution. [4-17]

"Cantilever" is a structural term that refers to a long beam having one of its ends fixed on a supporting base with another end standing freely. Cantilevers used in SPM usually are very short (less than ~ 300 micrometers) and have a thickness not more than a few micrometers. This is called a microcantilever. As shown in Figure 1.1 a microcantilever is a long and thin flexible beam that is V-shaped or bar-shaped depending on its application. Silicon and silicon nitride are the most common materials used to fabricate microcantilevers with an atomically sharp tip mounted near the freestanding end (Figure 1.2). Other materials have also been reported for making

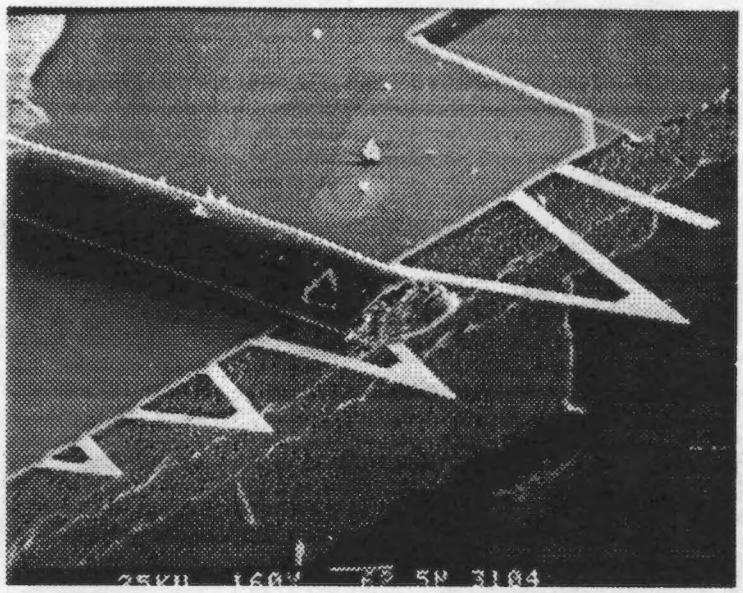


Figure 1.1: Array for microcantilevers with a human hair on the top.

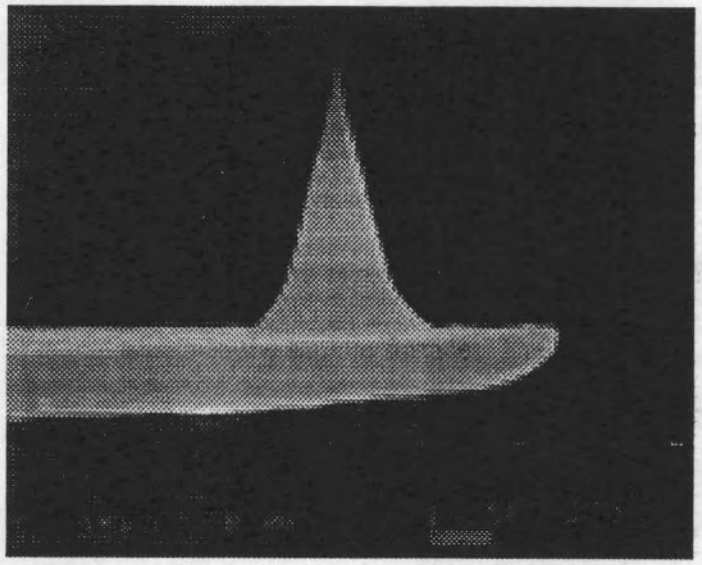


Figure 1.2: An atomic sharp tip is mounted at the end of cantilever.

microcantilevers, including piezoelectric materials, plastic materials and various metals. [18-24]

The premise of the AFM is based upon the fact that cantilevers have a spring constant (<< 1 N/m) that is much less than the equivalent spring constant on the contacted material surface. For a cantilever with a spring constant of 0.01 N/m, when a static load of 10^{-8} N is applied results a static deflection of 10^{-6} m, which means that even structures of several nanometers height will be subject to an almost constant force, whether it is controlled or not. When the cantilever is brought down to a very close distance (~10^{-10} m) to the surface, the force between the tip and the sample surface causes deflection in the cantilever. Such small deflections (< 1 nm) can be detected by several methods. [1-3, 5-8, 10, 21] But in today's market, the optical deflection technique is the most common method used to monitor cantilever deflection. A laser beam emitted from a laser diode is focused and guided to the backside of the microcantilever. The reflected laser beam projects on an optical position-sensitive detector (PSD), where the microcantilever deflection is monitored in a very precise fashion. [25] The microcantilever tip rasters over the sample surface, while the microcantilever deflection records the relative height. Processed signals are sent to a computer for reconstruction of a 3-D topography image of the sample surface.

There are two basic operational modes for AFM: contact-mode AFM (CMAFM) and tapping-mode AFM (TMAFM). For the CMAFM the microcantilever tip remains in constant contact with the sample surface in order to map the surface. For the TMAFM a built-in piezoelectric tip holder is employed to excite the

microcantilever to its resonance frequency. When the tip scans over the sample, the tip senses the force derivative of the tip-sample interaction through changes in the oscillation amplitude. The tip gently touches the surface at each of its extreme downward excursions without dragging in contact with the surface. This operational mode can reduce the surface damage caused by the tip-surface shear force and is especially useful for imaging soft materials such as biological samples. Unlike STM there is no electrical conduction required between the tip and sample surface during imaging for AFM. Thus AFM can be used to investigate both conducting and non-conducting samples and could be operated in vacuum, air and even in liquids. The active element of the AFM is, of course, the microcantilever exploited as a chemical sensor in the thesis.

1.1.2 Microcantilever Sensors

Recently, microcantilever based sensors have attracted much attention due to their potential as a platform for the development of myriad physical, chemical, and biological sensors. [26-41] Studies have shown that thin bi-material microcantilevers undergo bending (deflection) due to differential stresses caused by exposure to such environments. [18, 19, 27, 42-55] Because of their very small spring constants (less than 0.01 N/m), the microcantilevers are sensitive to stress differentials between the substrate and coating layer.

A schematic diagram of a bi-material cantilever beam is shown in Figure 1.3 in which a V-shaped cantilever beam with a thickness of t_1 is covered by a coating layer

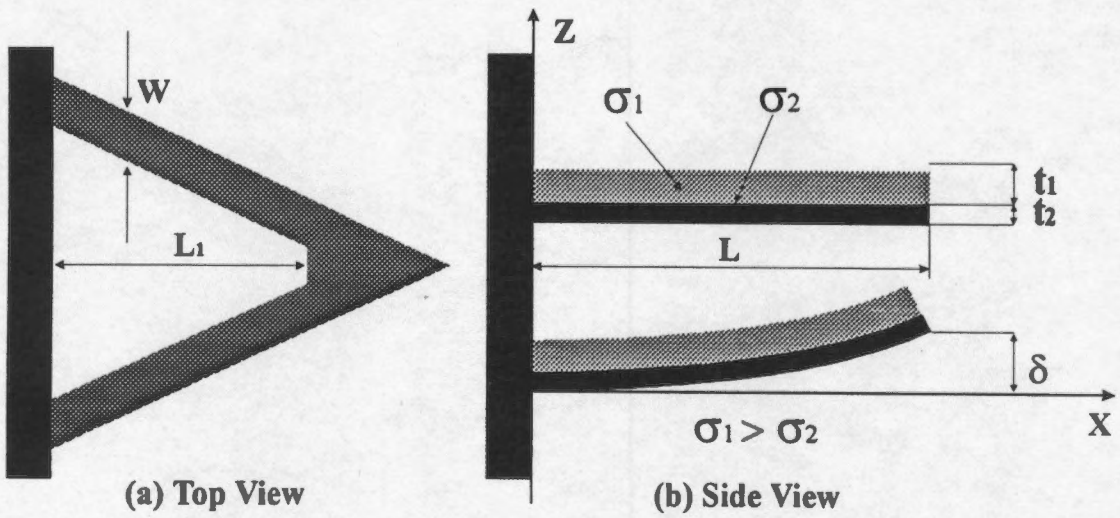


Figure 1.3: Schematic diagram of a bi-material V-shaped cantilever beam.

with a thickness of t_2. When the stresses, σ_1 and σ_2, on both sides are equal ($\sigma_1 = \sigma_2$), the cantilever remains level. When stress on one side is larger than that on other side, the cantilever will bend towards one side and have a deflection displacement δ at its freestanding end as shown in Figure 1.3(b). This displacement can be precisely detected by various methods. In this thesis both optical and electrical detection techniques are discussed. The detailed descriptions will be introduced in the later chapters.

For a given cantilever with specially designed coating layer(s), the deflection yields information about the environments to which the cantilever is exposed. Arrays of cantilevers with different coating configurations could be embedded in one silicon chip with multi-target detection capabilities. Thus, a new generation of compact, portable, low-power consuming, very sensitive sensors could be developed based on microcantilever techniques.

1.2 Thin Film Properties

1.2.1 Preparation of Thin Films

Thin films are thin layers of depositions applied to a thicker substrate. Deposition layers and the substrate are generally made of different materials. Depending on the actual applications and fields (such as semiconductor device manufacture, biological sample preparations, etc.), the thicknesses of the films can be varied over a wide range from a few nanometers up to millimeters. With the

improvements of thin film preparation techniques and analytical techniques, sub-micron-thick films are widely used and will be used in this study. [56-59]

Research in preparing thin films was started more than a century ago. According to recorded literature, the first thin solid films were obtained by electrolysis in 1838. Using a chemical reaction and glow-discharge sputtering respectively Bunsen and Grove also obtained metal films. In 1857, Faraday coated metal films onto a current-carrying metal wire in an inert atmosphere. Today, there are many methods that have been developed to prepare thin films under various conditions as listed in Table 1.1, which briefly summarizes thermal, cathodic, and chemical methods. [59]

In this thesis all samples were prepared by either vacuum evaporation or sputtering. When a thin film is prepared using these methods, a vacuum chamber is used to house the sample. A condensed-phase material is in the vacuum chamber and is heated or sputtered into the gaseous phase. The vapor traverses the space between the evaporation source and the substrate at reduced gas pressure and arrives at the substrate where it condenses onto the sample surface. The deposition thickness can be monitored using a mass-sensitive device (such as a quartz-crystal microbalance) or by optical density means.

1.2.2 Mechanical Properties of Thin Films

Compared to bulk materials, thin films show some very interesting mechanical characteristics that have drawn much attention. Properties such as adhesion, stress and

Table 1.1: Thin film preparation methods*

Preparation Methods	Thermal Evaporation	Cathodic Sputtering	Chemical Deposition
Techniques	Resistive heating Multi-source RF heating Electron-beam Flash evaporation Arc evaporation Laser evaporation Exploding-wire	Glow discharge (diode) Ion plating Asymmetric AC and DC bias Triode (assisted Ionization) RF sputtering Ion-beam sputtering Reactive sputtering	Electrolysis Anodization Pyrolysis Hydrogen reduction Disproportionation Transfer reaction Polymerization Electroless deposition

* Summarized from reference [59].

tensile directly relate to film formation processes. [57-76] The film structural defects formed during the nucleation and growth processes often largely determine the properties of films. Even for the same material, the changes of substrate temperature and deposition rate cause the wide variety of crystal or grain sizes. Controlled thermal annealing processes are used to reduce stress, structural defects and resize the crystals.

Intrinsic stress is a residual internal stress and is different from the stress caused by thermal expansion differences between the film and substrate. Total stress σ observed in a film is equal to the sum of any externally applied stress plus thermal plus intrinsic components as [59, 68]

$$\sigma = \sigma_{\text{external}} + \sigma_{\text{thermal}} + \sigma_{\text{intrinsic}} \tag{1.1}$$

The definition of stress is the force F divided by the area A it is applied upon $\sigma = F / A$.[77] Thus, intrinsic stress $\sigma_{\text{intrinsic}}$ is the result of internal force F_{internal} and applied area A_{internal} as

$$\sigma_{\text{internal}} = \frac{F_{\text{internal}}}{A_{\text{internal}}}. \tag{1.2}$$

Even though a film may undergo creep and plastic deformation, it is found that very high strengths (i.e., yield stress) are obtained in thin films with values up to 200 times as large as those found in the corresponding bulk material. [57, 59, 68] The yield stress $\delta\sigma^*_{\text{film}}$ observed in a film is equal to the sum of bulk behavior, imperfections and a thickness effect, namely

$$\delta\sigma^*_{\text{film}} = \sigma_{\text{bulk}} + \sigma_{\text{imperfection}} + \sigma_{\text{thickness}} \tag{1.3}$$

where σ_{bulk} is the annealed configuration, $\sigma_{imperfection}$ is the additional stress arising from the formation to the film and resultant pinning of the dislocations, and $\sigma_{thickness}$ results from a thickness dependent imperfection density also taking into account line tension or surface effects. [59, 68]

Traditionally the mechanical stress σ of crystalline materials is believed to be largely controlled by the grain size d often described by the Hall-Petch relationship

$$\sigma^{*}_{film} = hd^{-1/2} + \sigma_0 . \qquad (1.4)$$

Here h is a constant taking into account the effect of restricting the thickness on the dislocation motion, and σ_0 is the bulk stress corresponding to the some lattice defect structure as the film. [59, 68]

1.2.3 Electrical Properties of Metallic Thin Films

Electrical properties of metallic thin films are mainly concerned with their electron transport properties such as conductivity and can be significantly different from those observed for bulk materials. Very thin films are frequently discontinuous, where the electrical conductivity is many orders of magnitude smaller that that of the bulk material and is generally characterized by a negative temperature coefficient of resistivity (TCR). The conductivity is found to vary exponentially with the inverse of temperature, suggesting that the conduction mechanism is thermally activated. It is ohmic at low applied fields, but nonlinear at high fields. [57, 59, 68, 69, 72, 73, 78]

According to the free-electron-gas theory electrical conductivity of a metal is directly proportional to the mean free path l of the conduction electrons and is given by [59, 68, 79, 80]

$$\eta = \frac{ne^2 l}{m_e V_e}, \tag{1.5}$$

where n is the number of free electrons per unit volume

$$n = \frac{8\pi}{3}\left(\frac{mV_e}{h}\right)^3 \tag{1.6}$$

where e is the electronic charge, m_e is the effective mass of the electron, V_e is the average velocity of the electron at the surface of the Fermi distribution, and h is Planck's constant. When the film thickness is of similar magnitude as the mean free path, the conductivity of continuous metal films depends strongly on film thickness, because of diffuse conduction-electron scattering from both surfaces of the film. [81] Thus, the film resistivity ρ_F is the sum of contributions of ideal lattice scattering ρ_B, surface scattering ρ_S and imperfections ρ_I, including impurities, and is written as

$$\rho_F = \rho_B + \rho_S + \rho_I . \tag{1.7}$$

1.3 Physical and Chemical Adsorption & Absorption

Adsorption occurs when a gas or vapor reaches equilibrium on a solid or liquid surface, the concentration of gas molecules is always found to be greater in the immediate vicinity of the surface than in the free gas phase regardless of the nature of

the gas or surface. Atoms at the solid or liquid surface are subject to an attractive force normal to the surface plane that is partially balanced by the adsorption of gas molecules. The solid or liquid is called the adsorbent, and the gas or vapor is the adsorbate or analyte. Absorption is also used to describe the diffusion process of gas penetrating into the bulk of solid or liquid. [56, 82-85] In literature, adsorption and absorption are interchanged. In this thesis, adsorption will be used in this thesis to describe our systems.

Adsorption of a gas at the solid surface is a spontaneous process and causes the reduction of the free energy G of the two phases (gas/solid) system. Because the gas adsorbed at the solid surface has fewer degrees of freedom than in its gaseous state, the entropy change ΔS of the whole system and the enthalpy change ΔH are negative [56]

$$\Delta G = \Delta H - T\Delta S. \tag{1.8}$$

Adsorption processes may be classified as physical or chemical, depending on the nature of the force involved. Physical adsorption is driven by van der Waals forces resulting from the interaction of fluctuating dipoles. The formation of a physically adsorbed layer may be likened to the condensation of a vapor forming a liquid. The enthalpy of physical adsorption (or the binding energy of the adsorbate) is of similar magnitude to that of the corresponding heat of condensation of the gaseous adsorbate. [84] Chemical adsorption, on the other hand, is a chemical reaction that involves the transfer of electrons between the solid and gas and formation of a chemical compound.

The difference between the physical adsorption and chemical adsorption is distinguishable by the following criteria: [56]

1. The heat of physical adsorption is of the same order of magnitude as the heat of liquefaction of the adsorbate, where the heat of chemical adsorption is of the same order as that of the corresponding bulk chemical reaction.
2. Like condensation, physical adsorption could occur in any gas-solid system at suitable temperature and pressure, but chemical adsorption will take place only if the gas is capable of forming a chemical bond with the surface atoms.
3. Physical adsorption is reversible by removing gas pressure at the same temperature at which adsorption took place, although the process may be slow as gas atoms diffuse out from the solid. To reverse the chemical adsorption normally requires more effort even to remove the chemisorbed layer at the surface.
4. Under suitable conditions of temperature and pressure physically adsorbed layers several molecular diameters in thickness are frequently found. In contrast, chemisorption is complete once a monomolecular layer is built up, although physical adsorption may occur on top of the chemisorbed monolayer.

1.4 The Scope of This Thesis

Recent developments in MEMS (Micro-Electro-Mechanical Systems) have demonstrated the possibility of fabricating complex structures of microscale electro-mechanical devices. MEMS based solid-state sensors and actuators are gaining importance and interest. [36, 39, 42-45, 47-49, 51-55, 86-89] In order to sense

physical and chemical environmental changes, different coating layers are utilized. As the structural scale reduces to the microscale the limits to the conventional description of certain phenomena need to be reestablished. New mechanisms (such as adsorption and stress) of these thin films that may come into play at these very small dimensions need to be explored and studied.

The objective of this thesis is to understand the adsorption and adsorption-induced stress of thin metal films at micrometer scale using the ultra-high sensitivity of microcantilevers. In order to do so, palladium (Pd) and gold (Au) coated microcantilevers were exposed to hydrogen (H_2) gas and mercury (Hg) vapor respectively (properties of Pd, Au, H_2 and Hg may be found in Appendix E). Theoretical discussions about bi-material microcantilevers, diffusion, free surface energy and stress are introduced in Chapter 2. Chapter 3 is a detailed description of microcantilever deflection detection methods, experimental setup, thin film preparation and its resistance measurement, data acquisition and MUMPS chip. The experimental results, analyses and discussions will be included in Chapter 4 and 5 for hydrogen-palladium and mercury-gold systems respectively.

Experimental results indicate that hydrogen gas induces bulk-like adsorption onto palladium film and causes stress and electrical resistivity (or conductivity) changes in palladium films. Surface-like adsorption was found for mercury vapor on thin gold films as shown by induced stress and the electrical resistivity (or conductivity) changes in gold film. Film thickness as a function of sensitivity and response time were systematically studied.

A novel and simple experimental method was also developed to enable measurement of adsorption-induced stress and electrical resistivity changes simultaneously for the first time. The response time delay between the adsorption-induced stress and electrical resistivity change reveals the special properties of thin metal films during the adsorption process. This newly discovered phenomenon implies that there are complex mechanisms that have not been discussed in previous works. Influences of temperature and relative humidity at the thin films were also investigated.

Since both hydrogen gas and mercury vapor are hazardous, explosive, or toxic, they cause threats to safety and environment in working places. Finding low-cost, lightweight, small size, and high sensitivity sensors is a continuous effort. [38, 45, 49, 70, 78, 90-115] The MUMPS (Multi-User MEMS Process) chip developed by Oak Ridge National Laboratory (ORNL) is a cantilever-based micro-mechanical sensor platform. Up to 30 cantilevers have been integrated into one half-inch-square silicon chip with capability for both wired and wireless multi-channel readout allowing multi-target detection. The discussion of MUMPS design and comprehensive detection results will be found in Chapter 3, 4 and 5 accordingly. A summary will be presented in Chapter 6.

Chapter 2

THEORY

2.1 Theory of Microcantilevers

2.1.1 Simple Beam Theory and Cantilever Deflection

According to simple beam theory, the general differential equation of the elastic curve is given as [116]

$$\frac{d^2Z}{dx^2} = \frac{M}{EI}, \tag{2.1}$$

where x is the distance from the fixed-end of cantilever, Z is the vertical deflection of the sensor at a position x along its length L, M is the external moment, I is the moment of inertia of the section of the beam with respect to the neutral axis and E is Young's modulus of elasticity of the material.

Considering the case of an uniform load $w(x) = w$ along the cantilever as shown in Figure 2.1(a), we can use Eq.(2.1) to evaluate it and obtain the deflection curve of the cantilever beam. Taking the moment $M = \frac{w}{2}(L-x)^2$ into Eq.(2.1), we have

$$\frac{d^2Z}{dx^2} = \frac{w}{2EI}(L-x)^2. \tag{2.2}$$

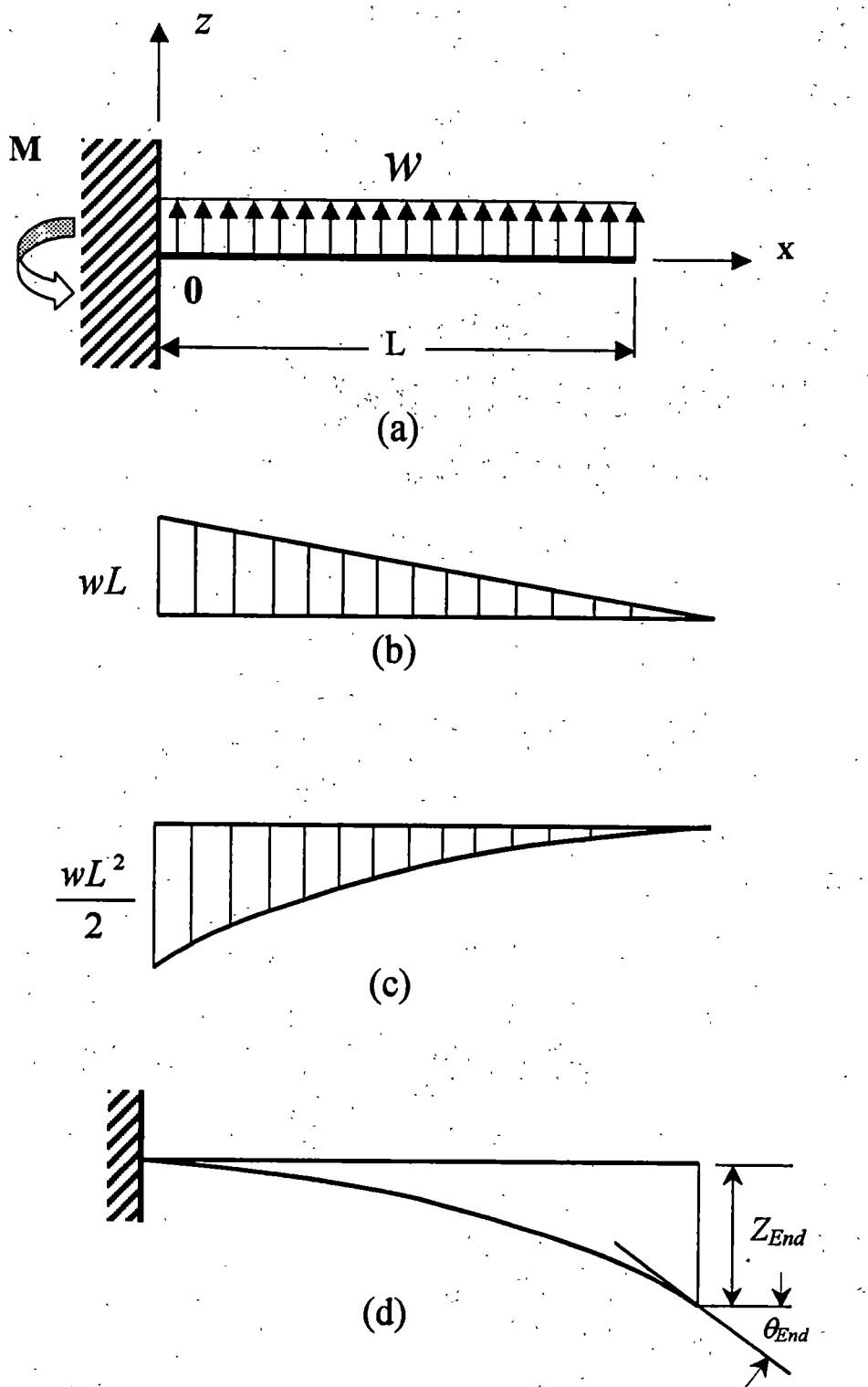


Figure 2.1: Uniformly loaded cantilever. (a) Loaded beam; (b) Loading diagram; (c) Moment diagram; and (d) Curvature diagram.

After integrating the above equation once and twice, the equation becomes

$$\frac{dZ}{dx} = -\frac{w}{6EI}(L-x)^3 + A, \tag{2.3}$$

$$Z(x) = \frac{w}{24EI}(L-x)^4 + Ax + B, \tag{2.4}$$

where A and B are the integration constants and may be determined by applying the boundary conditions: $Z(0) = 0$ and $dZ(0)/dx = 0$. Then the integration constants are

$$A = \frac{wL^3}{6EI} \text{ and } B = -\frac{wL^4}{24EL}. \tag{2.5}$$

Therefore, the cantilever displacement (deflection) $Z(x)$ as a function of the position x is given as

$$Z(x) = \frac{wL^4}{24EI}[(1-\frac{x}{L})^4 + (4\frac{x}{L} - 1)]. \tag{2.6}$$

At the free end of cantilever, shown in Figure 2.1(d), the cantilever has a maximum displacement that is

$$Z_{End}(x = L) = \frac{wL^4}{8EI}. \tag{2.7}$$

2.1.2 Natural Frequency of Cantilever

As mentioned in the previous chapter, most commercially available AFM microcantilevers are either V-shaped or bar-shaped and made from silicon (Si) or

silicon nitride (Si_3N_4). The theoretical calculation of mechanical properties associated with cantilever beams may be found in many engineering or structural dynamic books. [116-118]

Cantilevers are basically represented as a mass on a spring and thus possess a set of eigenfrequencies or resonances, the lowest of which is referred to as its natural or resonance frequency, f_0. The value of f_0 is dependent upon the cantilever's mass and mass distribution along the cantilever, the load placed on the cantilever and load distribution on the cantilever, the material properties and the dimensions of the cantilever plus the damping effects caused by the surrounding environment. For an undamped rectangular cantilever with a mass of m_b and length L, its natural frequency f_0 is expressed as [10, 116, 118]

$$f_0 \approx \frac{1}{2\pi}\sqrt{\frac{3EI}{L^3(m+0.24m_b)}}, \tag{2.8}$$

where EI is the flexural rigidity of the beam and m is a concentrated mass at its end. The derivation of this equation may be found in Appendix B.

In general, the equation of motion of the cantilever for an undamped system is given by

$$\frac{\partial^2}{\partial x^2}(EI\frac{\partial^2 Z}{\partial x^2})+\rho_c A_c\frac{\partial^2 Z}{\partial t^2}=0, \tag{2.9}$$

where E is the Young's modules, I is the moment of inertia , A_c is the cross-sectional area at position x, and ρ_c is the density of the cantilever. The classical solution of normal modes of cantilever is given as [10, 46]

$$f_n = \frac{\kappa_n^2}{2\pi}\sqrt{\frac{EI}{\rho A}}, \tag{2.10}$$

where κ_n is a parameter determined by the properties of cantilever. For a cantilever with uniform, rectangular cross section, κ_0 is about 1.875 for the first serial values f_0. In general, V-shaped cantilevers have been treated as two rectangular (bar) beams in parallel. [10, 46, 119, 120]

For a silicon cantilever as shown in Figure 2.2, the author used a laser spot to measure the vibration amplitudes at the different position along the cantilever beam and for different normal modes of oscillation. Data was taken from a C-type Microlever using BioScope (Digital Instrument, CA) in ambient without external driving (Brownian excitation only). The results are shown in Figure 2.2 for four resonant frequencies (f_1 = 6 kHz; f_2 = 37.5 kHz; f_3 = 41.75 kHz; and f_1 = 67.5 kHz). The dimensions of the cantilever are: overall length L = 320 μm, inside clearance L_1 = 280 μm, width W = 22 μm, thickness t_1 = 0.6 μm, and spring constant k = 0.01 N/m. The x-axis in the plot is expressed by the relative position toward the free end of the cantilever. The left y-axis is the peak amplitude of vibration frequency in mV and the right y-axis is the equivalent cantilever displacement in nm (deflection sensitivity = 90.5 nm/V). Each spot in the plot is a measurement point of a 20-μm diameter laser spot with an average spacing of ~10 μm between points.

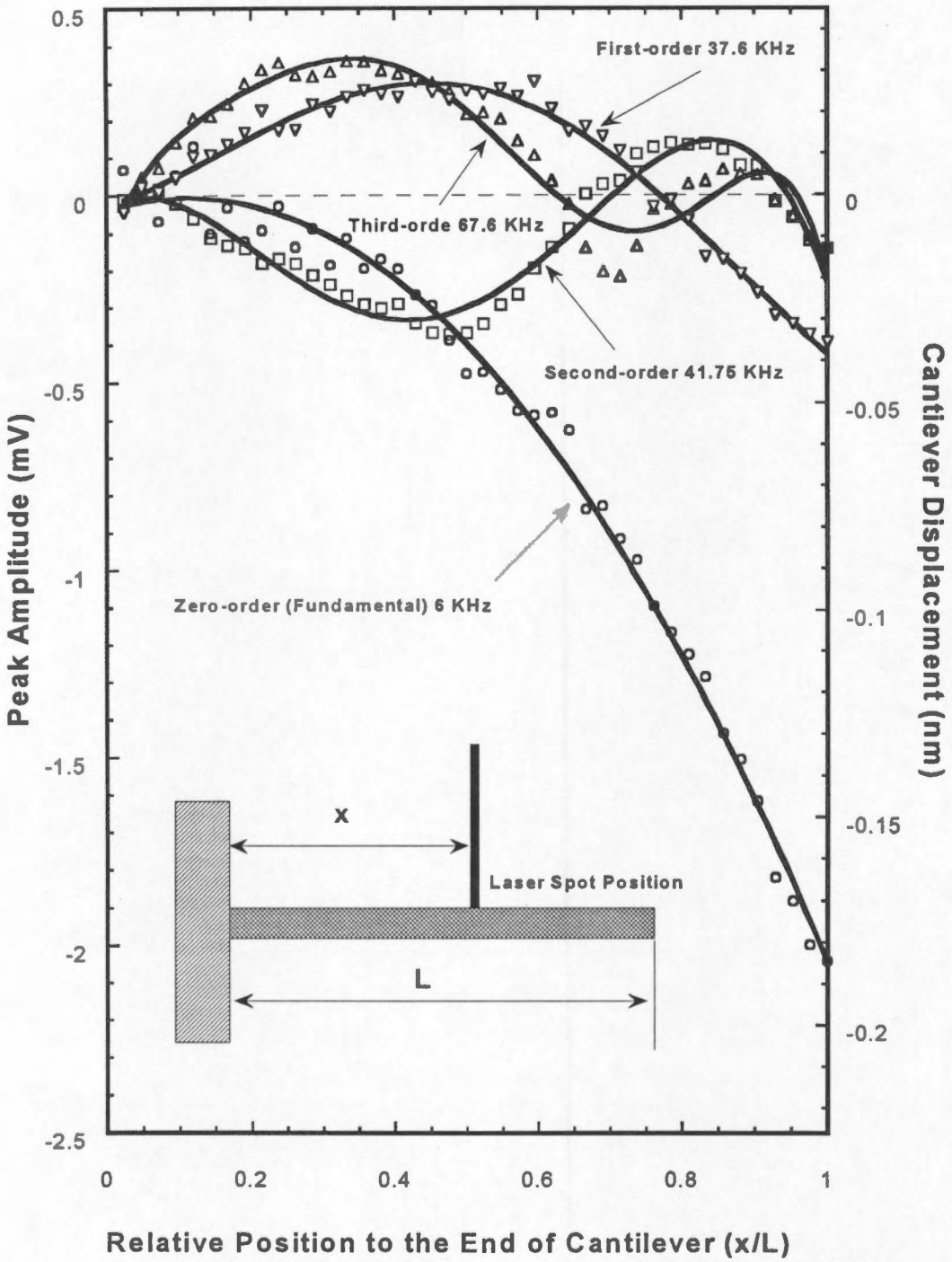


Figure 2.2: Four normal mode vibration frequencies of a V-shaped silicon cantilever. Data was taken from a C-type Microlever using BioScope (Digital Instrument, CA) in ambient without external driving (Brownian excitation only).

2.1.3 Volume Expansion of Bi-material Microcantilevers

The Si or Si_3N_4 microcantilevers used in the experiments have been coated with a layer of metal (palladium for the hydrogen experiment) resulting in so-called bi-material cantilevers. To analyze the bi-material cantilever beam systems, we consider bending of the cantilever caused by the differential volume expansion during gas adsorption. Since the length of the cantilever is much greater than its thickness and width, it is treated as a single-degree-of-freedom system in spite of the complexity of the real system. Although both V-shaped and Π-shaped cantilevers have been employed in our experiment, for simplicity we model the sensor as a rectangular beam with one degree of freedom. From the literature it is clear that this simplification is good for modeling cantilever motion. [46, 50]

For a bi-material beam with different expansion coefficients, the differential equation Eq.(2.1) becomes [121]

$$\frac{d^2Z}{dx^2} = 6(\alpha_1 - \alpha_2)(\frac{t_1 + t_2}{t_2^2 K})C(x), \qquad (2.11)$$

where $t_{i=1,2}$ and $\alpha_{i=1,2}$ are layer thickness and expansion coefficient with the subscripts referring to the two layers of the sandwich structure respectively. Here the quantity $C(x)$ is a generalized load that in our case corresponds to gas concentration. The quantity K in Eq.(2.11) is given by:

$$K = 4 + 6(\frac{t_1}{t_2}) + 4(\frac{t_1}{t_2})^2 + (\frac{E_1}{E_2})(\frac{t_1}{t_2})^3 + (\frac{E_2}{E_1})(\frac{t_2}{t_1})$$

If it is assumed that the gas concentration is uniformly along the length of the cantilever, then $C(x)$ is a constant for position x. It is also assumed that the Young's moduli do not change during the adsorption (the adsorption variation is negligible especially for low concentration). [122-124] Eq.(2.11) can be solved in a similar fashion for a cantilever with uniform load. The cantilever deflection can now be expressed as: [121]

$$Z_A = 3(\alpha_{A1} - \alpha_{A2})(\frac{t_1 + t_2}{t_2^2 K})CL^2. \qquad (2.12)$$

where L is the length of the cantilever at room temperature, and α_A is the adsorption induced expansion coefficient for each material.

Eq.(2.12) shows that for any given gas concentration C, the cantilever displacement Z_A varies as a function of each of the coating thicknesses and can be optimized for maximum response. Illustrated in Figure 2.3 is a calculation of the deflection of a palladium coated silicon cantilever in equilibrium with dilute hydrogen gas. The palladium thickness, t_1, is varied and choose $L = 85$ μm, $t_2 = 0.7$ μm, $E_1 = 12.1 \times 10^{11}$ N-m^{-2}, $E_2 = 1.79 \times 10^{11}$ N-m^{-2}. Experiments indicate that for low hydrogen concentration (< 2000 ppm) the adsorption-induced linear expansion coefficient is about $\alpha_{A1} = 1 \times 10^{-3}$ ppm^{-1}. The predicted detection sensitivity initially increases with the coating film thickness, reaches its maximum value, and then falls more slowly to zero again for a single material. The maximum deflection sensitivity is obtained when the thickness ratio is about 0.2 for this particular configuration.

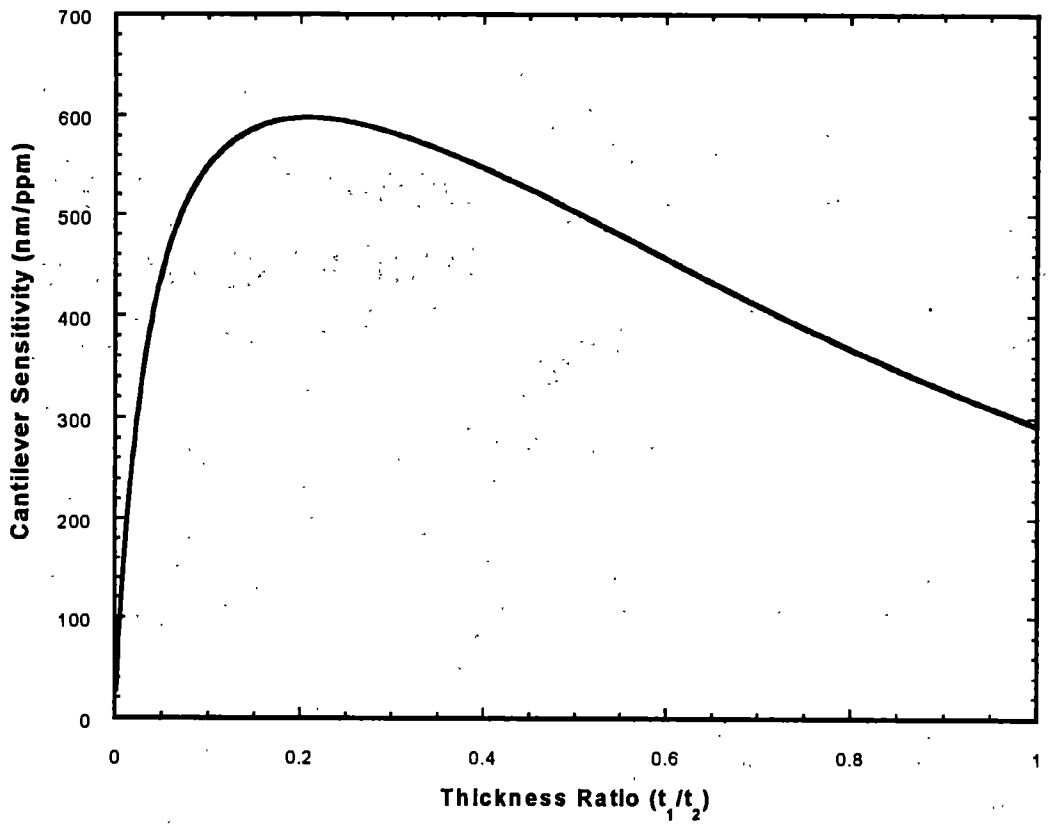


Figure 2.3: Theoretical curve of thickness dependence-sensitivity for a bi-material cantilever. The calculation was based on a 700 nm thick and 85 mm long silicon cantilever coated with palladium film.

The optical detection method, which will be introduced in the later part of this chapter, is used for small angles. The cantilever deflection is proportional to the output voltage of the photodiode and can be defined as $\delta = \eta \Delta V$. Deflection sensitivity η can be obtained from experiments. [46]

For the case where $\alpha_{A2} \approx 0$, a good approximation for Si and Si_3N_4 used in this thesis, α_{A1} may be determined from

$$\alpha_{A1} = \frac{\eta t_2^2 K}{3(t_1 + t_2)L^2} \frac{\Delta V}{C}. \tag{2.13}$$

2.1.4 Thermal Effects

Similar to Eq.(2.11) the differential equation for a bi-material cantilever due to the different thermal expansions of two materials is

$$\frac{d^2 Z}{dx^2} = 6(\tau_1 - \tau_2)\left(\frac{t_1 - t_2}{t_2^2 K}\right)[T(x) - T_0]. \tag{2.14}$$

Here $\tau_{i=1,2}$ is the thermal expansion coefficient with the subscripts referring to the two layers of the sandwich structure, and $T(x) - T_0$ is the profile of the temperature difference relative to the ambient temperature along the length of the cantilever beam.

If the cantilever is in a temperature bath (uniform temperature), the cantilever thermal deflection Z_T can be expressed as

$$Z_T = 3(\tau_1 - \tau_2)\left(\frac{t_1 - t_2}{t_2^2 K}\right)[T - T_0]L^2. \tag{2.15}$$

Obviously, the total deflection of the cantilever is the sum of adsorption-induced deflection plus the heat-induced deflection

$$Z_{total} = Z_A + Z_T . \qquad (2.16)$$

At 40 ^{0}C the thermal expansion coefficient for palladium is 1.176 x 10^{-5} /^{0}C. [125] Hydrogen adsorption-induced linear expansion coefficient measured experimentally is about $10^{-4} \sim 10^{-3}$ ppm^{-1}. Thus, it is important to reach the thermal equilibrium before any experiment can be conducted.

2.2 Diffusion Theory

As mentioned in Chapter 1 gas adsorption on a solid surface does not always involve only a few layers of atoms at the solid surface. Sometimes gas atoms can migrate through the bulk of the material and dissolve within the solid. It is necessary to have some basic understanding about how this process takes place. The theory used to describe the atom (or molecule) migration is called diffusion theory. In this section the diffusion theory and related equations that will help us to explain the results from our experiments will be introduced.

2.2.1 Diffusion in Solids

Diffusion is a process in which atoms or molecules are transported from one position to another. Such atomic migration is a random motion for individual atoms and can occur within gas, liquid and solid materials. [77, 126-128] The diffusion that

takes place in a pure substance is called self-diffusion as energetic atoms jump to the lattice defects. Diffusion that occurs at the interface of two substances is called binary diffusion or interstitial diffusion. In fact, this kind of diffusion can be found at almost any interface combination among gases, liquids and solids such as gas-gas, gas-solid or solid-solid interface, etc. The smaller atoms such as gases like hydrogen, nitrogen and oxygen may migrate into solid materials such as steel, palladium, nickel, and polymers. [122-124, 127-155]

Vacancy, interstitial, interstitialcy and exchange are four main types of diffusion mechanisms. For each of these there are many possible variations. For example, in the multi-vacancy case, diffusion occurs in a different manner from the one in the single vacancy case. [129] As shown in Figure 2.4, the interstitial mechanism is the simplest and also the most common diffusion mechanism. It is also called the direct interstitial mechanism. Because of interatomic forces the potential energy is a function of diffusion atom location. Experiments have indicated that the rate of diffusion (the coefficient of diffusion) varies exponentially with temperature. [127-129, 131, 137, 147, 148] The temperature dependent coefficient of diffusion D for interstitial diffusion may be expressed as

$$D = D_0 \exp(-\frac{Q}{k_B T}), \tag{2.17}$$

where D_0 is the pre-exponential factor and is relatively independent of temperature. Q is the activation energy for diffusion, k_B is the Boltzmann constant and T is the absolute temperature.

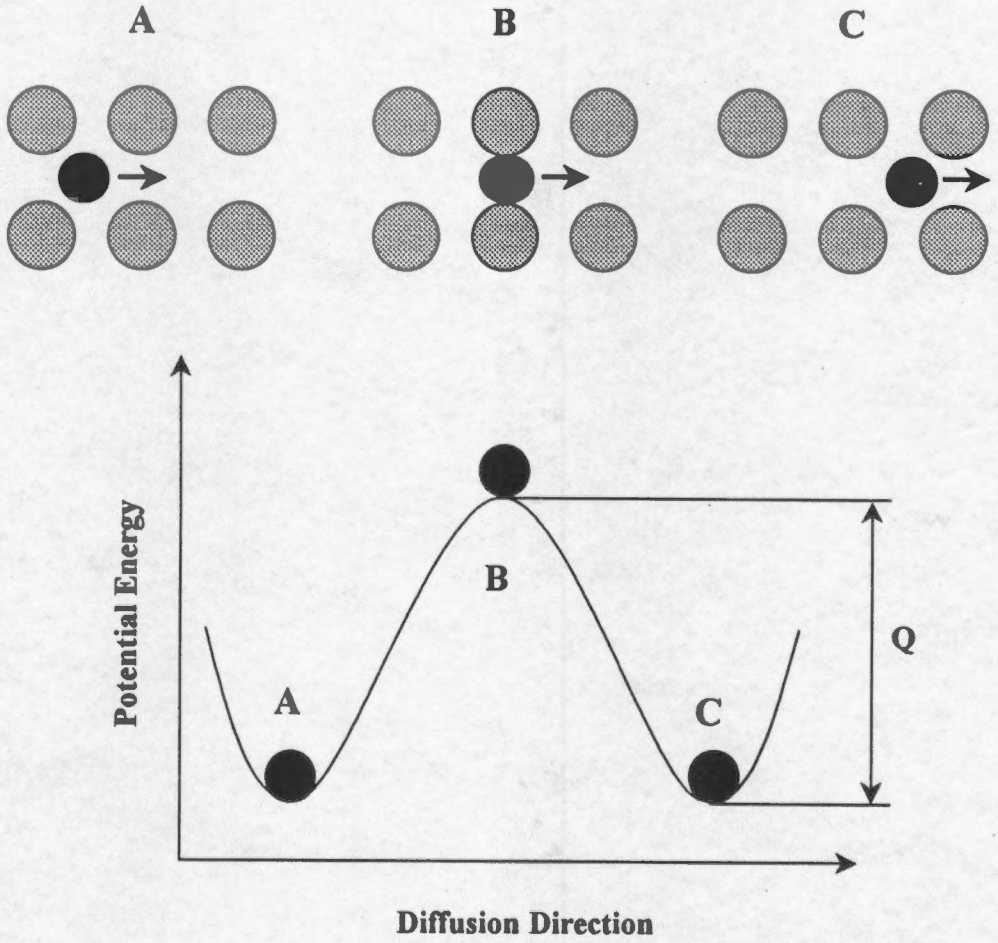


Figure 2.4: Schematic of a jump step in interstitial diffusion.

In this thesis all experiments are conducted at room temperature except for those involving temperature dependences. Thus the coefficient of diffusion is treated as a constant unless stated otherwise.

2.2.2 Diffusion Equations

In 1855 Fick first introduced the following equation and put diffusion on a quantitative basis by adopting the mathematical equation of heat conduction derived some years earlier by Fourier (1822). For one-dimensional diffusion, the diffusion current (flux) without an applied force is

$$J = -D\frac{\partial C}{\partial x}, \tag{2.18}$$

where D is the coefficient of diffusion for the substance under consideration, C is the concentration of the diffusion substance and x is the coordinate chosen perpendicular to the reference surface. Generally Eq.(2.18) is referred as Fick's first law.

Because matter is conserved the time dependent concentration indicates

$$\frac{\partial C}{\partial t} = -\nabla \cdot \vec{J} = \frac{\partial}{\partial x}(D\frac{\partial C}{\partial x}) \tag{2.19}$$

If D is a constant, then Fick's second law is expressed as

$$\frac{\partial C}{\partial t} = D\frac{\partial^2 C}{\partial x^2}. \tag{2.20}$$

In this thesis thin metal films were coated onto silicon (or silicon nitride) cantilevers. Gas adsorption into the metal film induced film expansion and stress change thus causing bending of the cantilever and thin film resistance variation. Therefore, it is necessary to know the diffusion processes of gas atoms into metal films. Experiments were performed when one side of the bi-material cantilever was composed of gas active metal film and the other side was a gas inert substrate. Coated cantilevers were always exposed to constant gas concentrations. The diffusion processes in the following two cases are here calculated. Case one is the case of diffusion in a plate of sheet where both sides of the sheet have constant concentrations. Case two is the case of diffusion in a plate sheet when both sides of the sheet have impermeable surfaces in which the concentration gradient is zero.

Case 1: *Initial concentration distribution is $f(x)$ in the region $0 < x < l$ and the concentrations at both ends are constants.*

In the case in which the ends are kept at constant concentrations C_1 and C_2 find the following boundary conditions:

$$\text{At time } t \geq 0, \qquad C = C_1, \qquad x = 0; \tag{2.21}$$

$$\text{At time } t \geq 0, \qquad C = C_2, \qquad x = l; \tag{2.22}$$

$$\text{At time } t = 0, \qquad C = f(x), \qquad 0 < x < l. \tag{2.23}$$

The solution for Eq. (2.20) in the form of a trigonometric series is [156-158]

$$C(x,t) = C_1 + (C_2 - C_1)\frac{x}{l} + \frac{2}{\pi}\sum_1^\infty \frac{C_2 \cos n\pi - C_1}{n} \sin\frac{n\pi x}{l} \exp(-Dn^2\pi^2 \frac{t}{l^2})$$

$$+ \frac{2}{l}\sum_1^\infty \sin\frac{n\pi x}{l} \exp(-Dn^2\pi^2 \frac{t}{l^2}) \int_0^l f(x') \sin\frac{n\pi x'}{l} dx' . \qquad (2.24)$$

If at time $t = 0$, the concentration distribution $f(x)$ is zero, the last term of the above equation vanishes.

Case 2: *Initial concentration distribution is $f(x)$ in the region $0 < x < l$ and the surfaces at both ends are impermeable.*

An impermeable surface is one in which the concentration gradient is zero. This condition holds at the central plane of a sheet provided that the boundary conditions are symmetric about the plane. It follows, therefore, that the symmetric solutions already given for the plane sheet occupying the region $-l < x < l$ apply also to the sheet $0 < x < l$ when the face $x = 0$ is impermeable. If both surfaces $x = 0$ and $x = l$ are impermeable and the initial distribution is $f(x)$, the solution is [156, 158]

$$C(x,t) = \frac{1}{l}\int_0^l f(x')dx' + \frac{2}{l}\sum_{n=1}^\infty \exp(-Dn^2\pi^2 \frac{t}{l^2}) \cos\frac{n\pi x}{l} \int_0^l f(x') \cos\frac{n\pi x'}{l} dx' \qquad (2.25)$$

Diffusion from one layer to another may be calculated by treating the system as a single layer with impermeable boundaries in which the distribution at time $t = 0$ is as follows:

$$f(x) = C_0, \qquad 0 < x < d; \qquad (2.26)$$

$$f(x) = 0, \qquad d < x < l. \tag{2.27}$$

Then the solution for this particular case becomes

$$C(x,t) = C_0\left[\frac{d}{l} + \frac{2}{\pi}\sum_{n=1}^{\infty}\frac{1}{n}\sin\frac{n\pi h}{l}\exp(-Dn^2\pi^2\frac{t}{l^2})\cos\frac{n\pi x}{l}\right]. \tag{2.28}$$

Eq.(2.28) can be used to calculate the concentration distribution for diffusion into a coating layer. For the process of diffusion out simply reverse the diffusion direction and assume at time $t = 0$ the concentration inside the solid is C_0. The concentration distribution inside the solid then may be described by the following equation [126]

$$C(x,t) = C_0 - C_0\left[\frac{d}{l} + \frac{2}{\pi}\sum_{n=1}^{\infty}\frac{1}{n}\sin\frac{n\pi h}{l}\exp(-Dn^2\pi^2\frac{t}{l^2})\cos\frac{n\pi x}{l}\right]. \tag{2.29}$$

For the case of hydrogen diffusion in palladium, the numerical evaluations are shown in Appendix A under different concentrations and diffusion coefficients. More discussions about palladium-hydrogen system will be introduced in Chapter 4.

2.3 Stress and Surface Energy

2.3.1 Stress and Strain

The conventional definition of stress is

$$\sigma = \frac{F}{A}, \tag{2.30}$$

where F is applied force and A is the area upon which the force is applied.[77] The change ΔL in a length divided by the original length L_0 before any stress is applied is defined as the linear strain ε as

$$\varepsilon = \frac{\Delta L}{L_0} . \tag{2.31}$$

For the elastic isotropic material, the transverse strain can then be defined as

$$\varepsilon_{tr} = \frac{\Delta r}{r_0} , \tag{2.32}$$

where Δr is the change in cross-sectional length, and r_0 is the original length. The ratio ν of the transverse strain ε_{tr}, in a direction perpendicular to the applied stress, to the normal strain ε is given by

$$\nu = \frac{\varepsilon_{tr}}{\varepsilon} , \tag{2.33}$$

where ν is called Poisson's ratio which is a constant for an isotropic material. As long as the deformed body is in its elastic regime, there will be a linear relationship between the stress and the strain

$$\delta = E\varepsilon , \tag{2.34}$$

where E is Young's modulus.

2.3.2 Surface Energy and Surface Stress

Atoms at a surface or interface are in a very different position and environment compared with those atoms in the bulk. The asymmetrical atomic structure and surface anisotropy are the sources of the extra interatomic force tensed surface stress, which is parallel to the solid surface. Surface energy is stored at the surface keeping a stable surface formation and boundary. Changes of surface energy may cause changes of surface stress or vice versa. The energy at the surfaces can be changed if the physical areas of the surface vary or the atomic positions at the surface change through elastic deformation. [159]

To create a surface it is necessary to do work on the system, break bonds or remove neighboring atoms. Under conditions of equilibrium at constant temperature T and pressure P, the reversible surface work $dW_{surface}$ required to increase the surface area A by an amount dA in a one-component system is given by

$$dW_{surface(T,P)} = \gamma dA\,, \tag{2.35}$$

where γ is called the surface energy and its units are J/m^2 or (N/m).

In the absence of any irreversible process the reversible surface work $dW_{surface(T,P)}$ is equal to the change in the total free energy of the surface dW_{free}. The change of total surface work $W_{surface}$ is thus equal to the change of specific surface free energy $G_{surface}$ times the surface area A

$$dW_{surface(T,P)} = d(G_{surface}A)\,. \tag{2.36}$$

Consider two ways to form a new surface: (a) simply increasing the surface area or (b) stretching the existing surface. Eq.(2.36) may be rewritten as

$$dW_{surface\,(T,P)} = G_{surface}\,dA + (\frac{\partial G_{surface}}{\partial A})_{T,P}\,A\,. \tag{2.37}$$

If the new surface is created by increasing the area, the specific surface free energy $G_{surface}$ is independent of the surface area so that $(\frac{\partial G_{surface}}{\partial A})_{T,P} = 0$, then the surface work is given by

$$dW_{surface\,(T,P)} = G_{surface}\,dA\,. \tag{2.38}$$

Comparing Eq.(2.38) with Eq. (2.35), it is easy to see $G_{surface} = \gamma$, which means that the surface energy is equal to the specific surface free energy.

The elastic deformation of a solid can lead to a new surface due to strain and be expressed in terms of a surface elastic strain tensor $\varepsilon_{i,j=1,2}$. Define a surface stress tensor $S_{i,j}$ with the variation in γA and the total excess free energy of the surface due to the strain $d\varepsilon_{i,j}$ as [132, 160]

$$S_{ij} = \frac{1}{A}\frac{d(\gamma A)}{d(\varepsilon_{i,j})} = \gamma\delta_{i,j} + \frac{d\gamma}{d\varepsilon_{ij}}\,. \tag{2.39}$$

This equation shows that the surface stress tensor $S_{i,j}$ changes may be due to the variation of surface free energy γ and the energy gains from the relaxation of the surface strain. For high-symmetry surfaces the surface stress is isotropic and can be taken as a scalar quantity. The total surface energy γ is a scalar as well. [159] Thus Eq.(2.39) may be expressed as

$$S = \gamma + \frac{\partial \gamma}{\partial \varepsilon}. \tag{2.40}$$

If the total free surface energy γ is a constant, the surface stress is equal to the change of surface free energy per unit change in elastic strain of the surface. This relationship may help explain mercury adsorption on a gold surface (Chapter 5) and the creation of a stress that causes bending of the microcantilever.

Chapter 3

EXPERIMENTAL

3.1 Detection Methods

Two methods have been utilized to detect the small deflection of microcantilevers. Optical position-sensitive detection (PSD) was used to measure the deflection of commercially available AFM microcantilevers, and an electrical detection technique was used to measure the cantilever bending on the MUMPS chips. The two detection methods will be introduced separately in this section.

3.1.1 Optical Cantilever Deflection Detection Technique

As shown in Figure 3.1 the movement of a microcantilever can be detected using a laser beam that reflects from the backside of the cantilever (opposite from tipped-side). This is the most common means for commercial AFM heads. In fact, a commercial head with built-in laser, cantilever holder and optical detector was used in these experiments (Digital Instrument, Santa Barbara, CA). A reflected laser beam projects onto the segmented photodiode sensors. Cantilever deflection causes a vertical displacement in the reflected laser beam that is amplified by the optical projection system since the projected laser spot travels a much greater

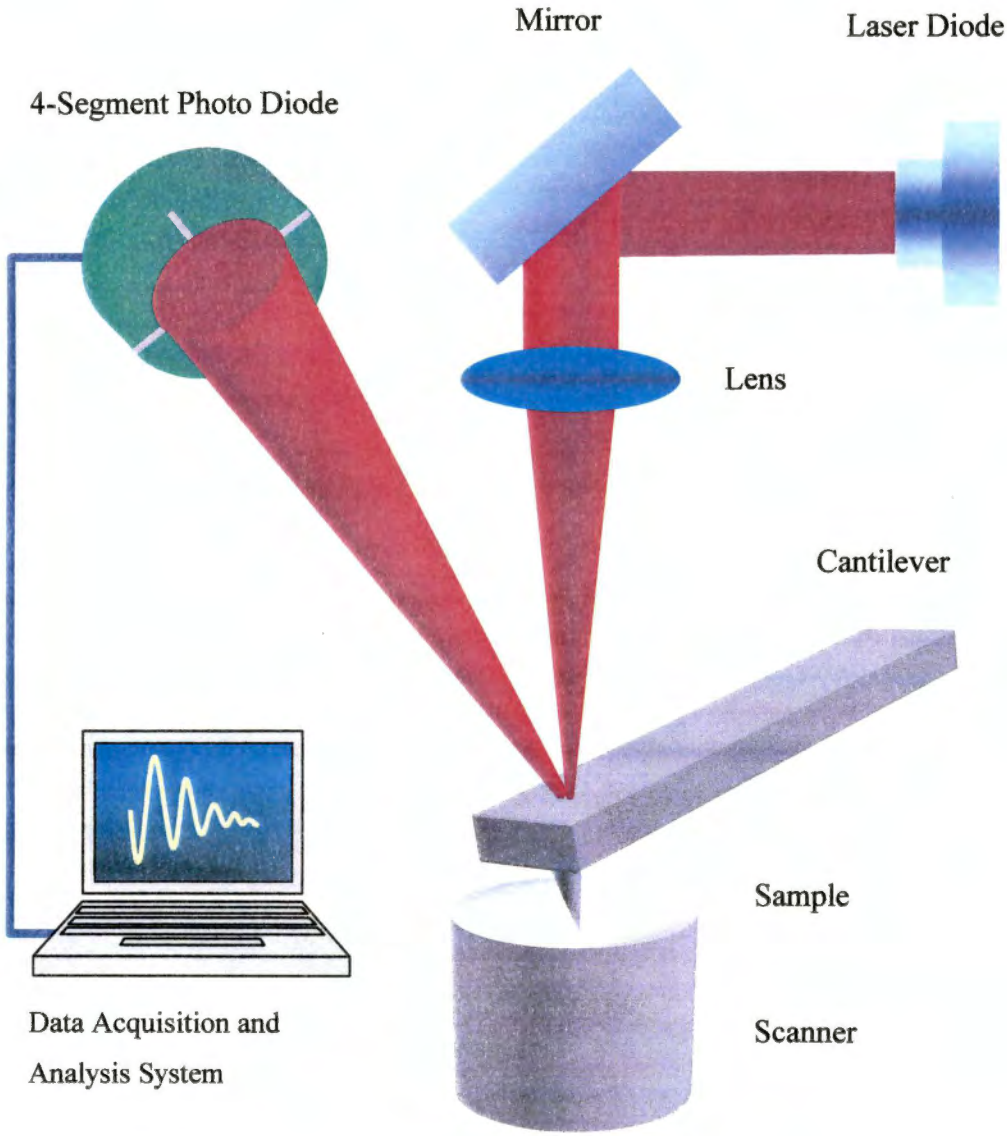


Figure 3.1: Schematic diagram of optical position-sensitive detection system.

distance on the photodiode, which can generate more detectable signals. The differential signals obtained from the segmented photodiodes are sent out to a computerized data acquisition and analysis system. The optical position-sensitive detector (PSD) used in this thesis can precisely measure the displacements of the cantilever with better than 10^{-10} m accuracy. For small deflections, the deflection is approximately equal to the slope ath the cantilever end. [46] Thus, we can define the optical deflection sensitivity η as

$$\eta = \frac{\delta}{\Delta V}, \tag{3.1}$$

where deflection sensitivity η can be measured experimentally, δ is the deflection of the cantilever and ΔV is the readout voltage from the output device. In order to measure the deflection sensitivities for different cantilevers, the cantilevers were placed within the AFM head in such a way that the cantilever tip gently touched the top of the piezoelectric scanner. Then voltages were applied to the piezoelectric scanner making the top of the scanner move up and down. The cantilevers then moved up and down along with the scanner top causing a corresponding change in the photo detector output voltage. The vertical movements of the scanner could thus be precisely calibrated from the voltages applied to the scanner. The output changes of the optical detector permitted measurement of the corresponding vertical displacements of the cantilevers. For C-type and D-type silicon Ultralevers their deflection sensitivities were found to be about 62 nm/V and 63.9 nm/V respectively. The detailed description and mechanical characteristics of Ultralevers and Microlevers may be found in Appendix C.

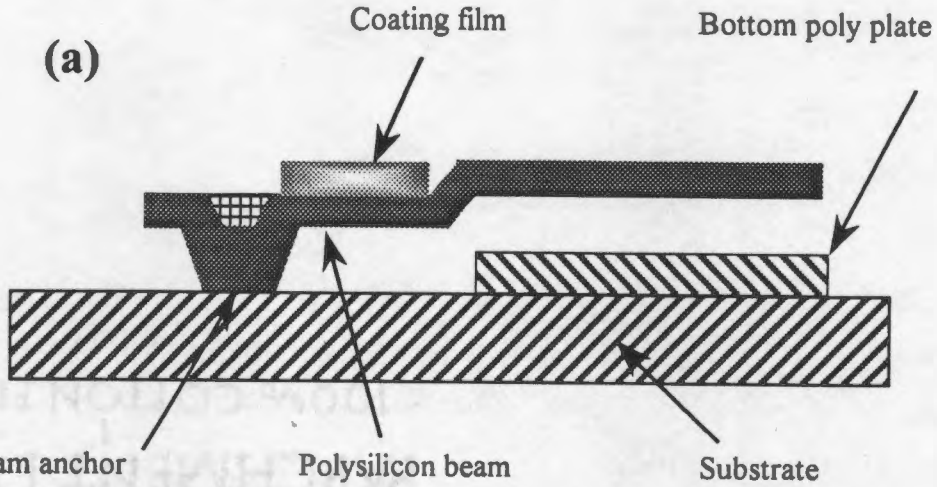
3.1.2 Electrical Detection Method and MUMPS Microcantilever

Since the optical detection method requires special designed and arranged optical devices and mechanical components, alignment difficulties and other problems (i.e., only can read one cantilever at one time) limit its application and portability despite its many advantages. Using the MUMPS (Multi-User MEMS Process, Chronos International Microsystems, Inc, Research Triangle Park, NC) fabrication technique, π-shaped cantilevers were developed at Oak Ridge National laboratory (ORNL). [43-45, 48, 55, 86] The cross-section view and top view of a MUMPS microcantilever are shown in Figure 3.2 and more information about the MUMPS chip can be found in Appendix D.

As shown in Figure 3.2(a) & (b), the cantilevers act electrically like a capacitor. Neglecting fringing, the capacitance of a parallel plate capacitance is defined as

$$C = \frac{\varepsilon_0 A_C}{d}, \tag{3.2}$$

where A_C is the plate surface area, ε_0 is the dielectric constant of air (8.85×10^{-12} F/m), and d is the distance between the plates. The cantilevers on the MUMPS chip have an area of 56×10^{-9} m^2 and a typical plate separation of 2×10^{-6} m. This gives a calculated capacitance of 0.25 pF. The measured capacitance of these cantilevers using a Roberts Loop has typically been between 0.5 and 1 pF. [48] The disparity in these numbers can be attributed to a variety of different reasons including fringing effects, stray capacitance, bending of the cantilevers due to residual stress and silicon



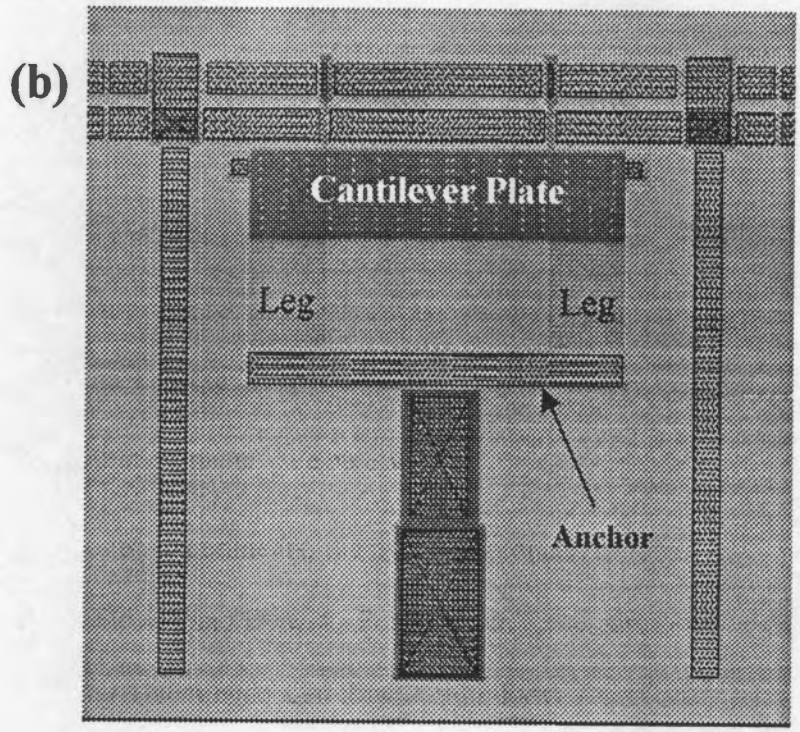


Figure 3.2: MUMPS microcantilever. (a) Cross-section with lower plate; (b) Top view of a MUMPS microcantilever.

dioxide remaining between the cantilever and the lower plate thereby changing the dielectric constant of the capacitor.

An approximation of the deflection of a cantilever tip for small angles of deflection can be determined from the measured capacitance value by [161]

$$C = \frac{\varepsilon_o a}{\phi} \ln\left[\frac{2d_0 + b\phi - 2Z_m}{2d_0 - b\phi - 2Z_m}\right], \tag{3.3}$$

where d_0 is the distance between the parallel plates prior to any movement, a is the width of the cantilever plate, and b represents the length of the overlap between the plates. The ϕ in the equation represents the angle between the two plates, and Z_m is a measure of the distance between two plates at the midpoint of overlap.

3.2 Thin Film Conductivity and Small Resistance Measurement

The resistance R of a sheet has a length of L, width a and thickness d is defined as

$$R = \rho \frac{L}{ad} \tag{3.4}$$

where ρ is called the coefficient of resistivity.

As mentioned in Chapter 1 thin metal films have some special electrical conduction properties compared to their bulk materials. If the films are in discontinuous formation, electrons may transfer between the disconnected nucleation islands by tunneling or thermionic emission. [79] For a continuous film as was the

case here, Fuchs indicated that the conductivity of the metal films is strongly dependent on film thickness. [59, 79-81, 162] The conduction-electrons scatter from both surfaces of the film if the film thickness is as the same order as the mean free path. Furthermore, unlike bulk metals, where lattice scattering is the main reason for having electrical resistivity, electron scattering from the grain boundaries and impurities also have noticeable contributions to the increase in resistivity. These effects cause dramatic changes in thin metal film conductivity.

Developing upon Fuchs' theory, Sondheimer derived the following equation for the thickness d dependent resistivity [163]

$$\rho(d) = \rho_0 + \frac{3}{8}\rho_0 \frac{1}{d}(1-p), \tag{3.5}$$

where ρ_0 is its bulk resistivity and p is a scatter related parameter.

Obtaining a precise measurement of a thin metal film is not simple, especially when the film resistance is small. A contact point resistance existing between the meter probe and film surface is often large enough to cause reduced accuracy of the measurement when the normal two-point (wire) method is used. To avoid this problem, (as shown in Figure 3.3) an improved 4-point (wire) method is generally preferred for low-resistance measurements. These measurements can be made using a digital multimeter (DMM), micro-ohmmeter, or a separate current source and voltmeter. With this configuration, the test current I is forced through the test resistance R_S through one set of test leads, while the voltage V_M across the film is measured through a second set of leads called sense leads. Some small current may

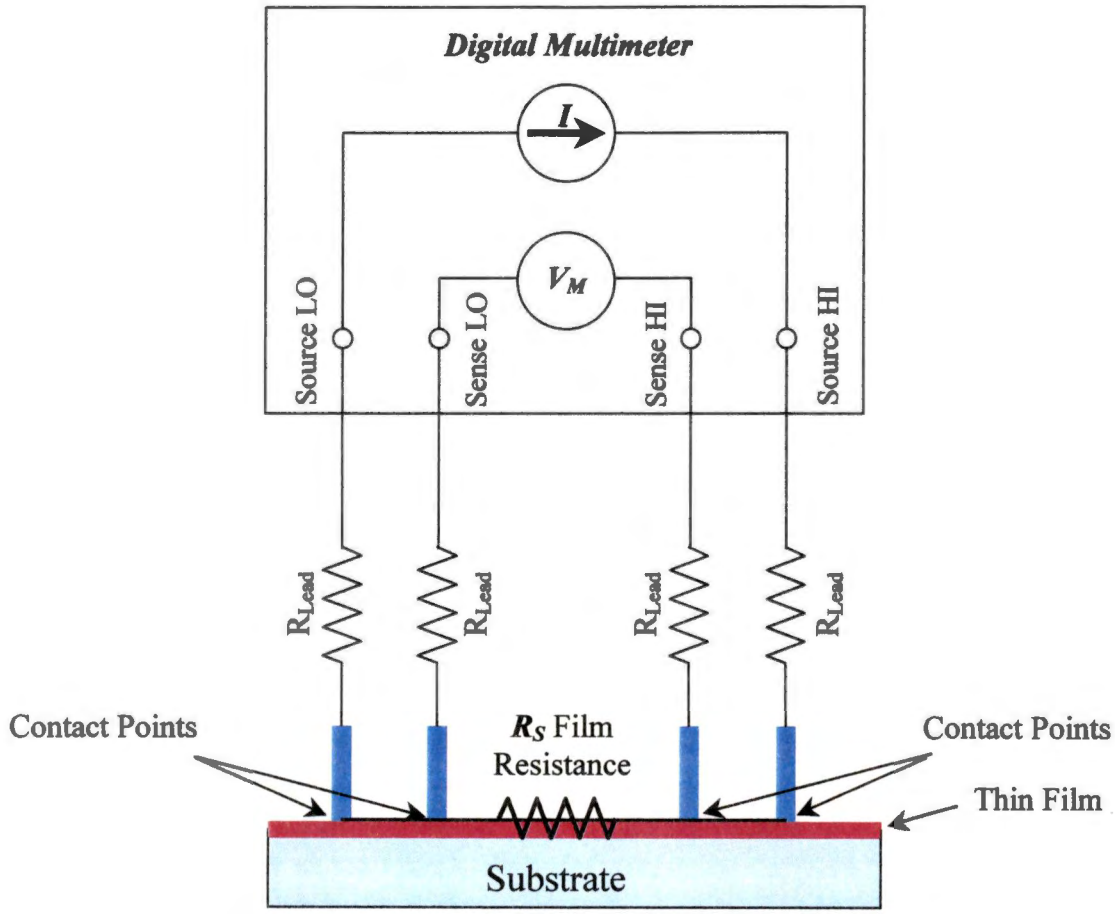


Figure 3.3: Thin film four-point resistance measurement.

flow, which can generally be ignored for all practical purposes. Since the voltage drop across the sense leads is negligible, the voltage measured by the meter V_M is essentially the same as the voltage V_R across the film resistance $R_S = V_R / I$. Consequently, the resistance value can be determined much more accurately than with the 2-point (wire) method.

3.3 Experimental Setup

The microcantilever gas adsorption experimental setup diagram is illustrated in Figure 3.4, and it contains five basic units: gas cell, gas mix and control system, optical detection unit, 4-point resistance measurement unit and data acquisition system. Two photographs of the experimental setup on an optical table are shown in Figure 3.5(a) & (b).

3.3.1 Gas Cell

A homemade glass and plastic gas cell was used to house the microcantilever and provide a controllable environment for gas adsorption experiments. Premixed gas or vapor flowed into the gas cell from one end and a small hole was opened at the other end in order to avoid pressure build up inside the cell. The internal space was about 9 mm in diameter and 10 mm tall giving a volume of 0.64 cm^3. The small volume of the gas cell made the task of maintaining constant gas concentration much easier. With 10 ccm (cubic-centimeter-per-minute) flow, the entire volume of the gas cell could be flushed once in less than 3.8 seconds. The ceiling of the gas cell was

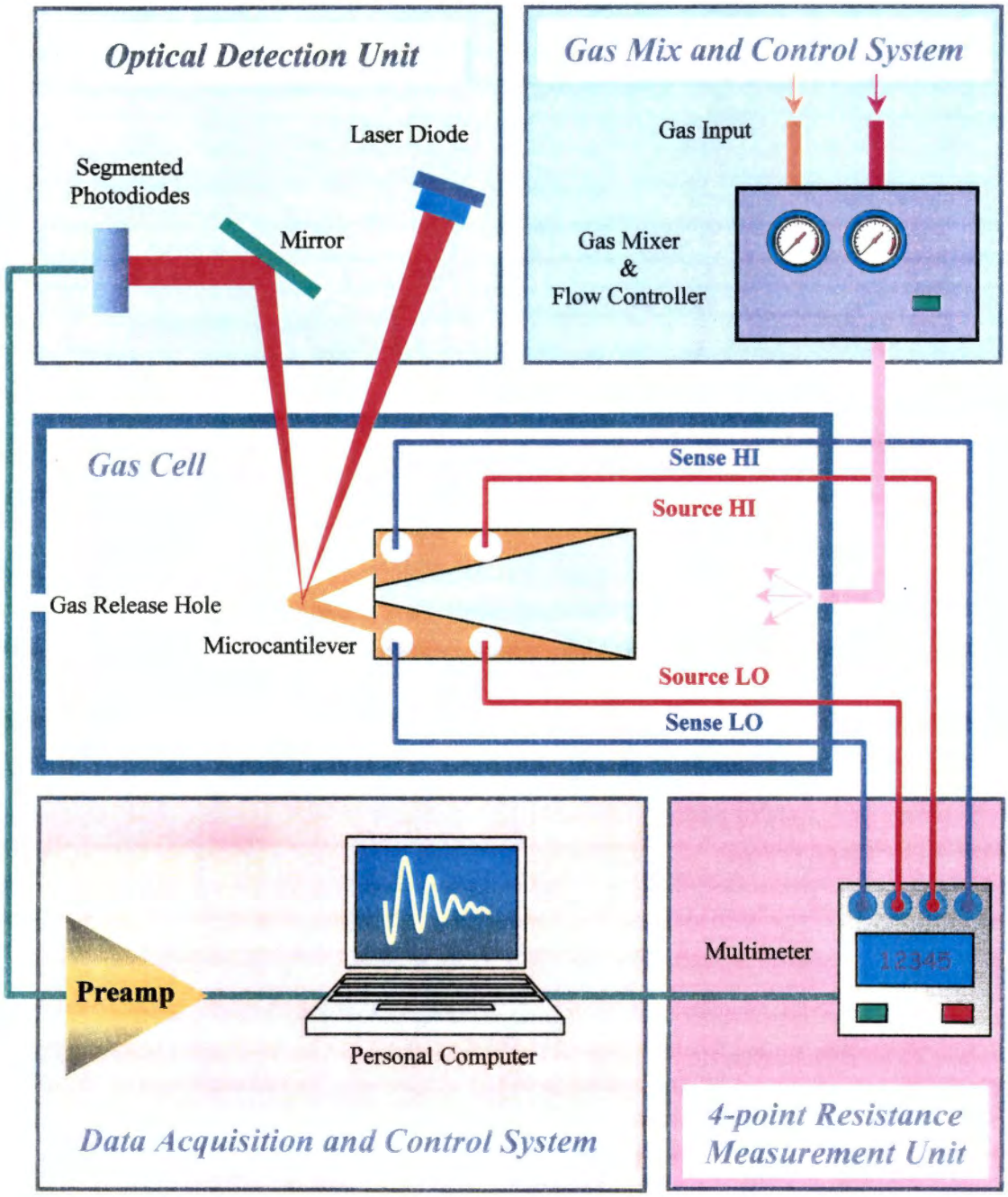


Figure 3.4: Schematic diagram of experiment setup with both cantilever deflection unit and thin film 4-point resistance measurement unit.

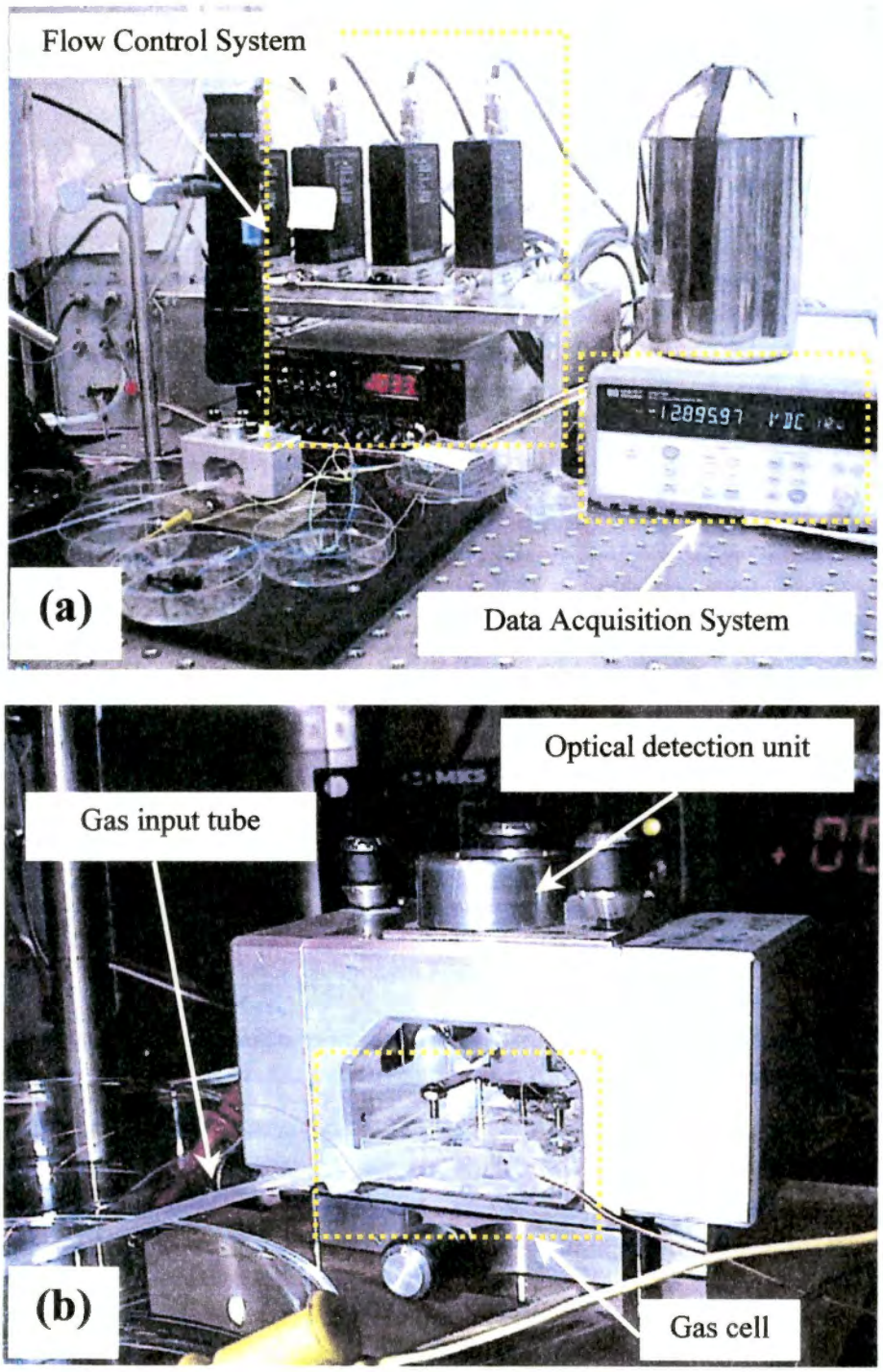


Figure 3.5: Laboratory instrument Setup. (a) Test setup with flow control, gas cell and data acquisition unit; (b) Gas cell and optical detection unit.

made of transparent glass allowing the laser beam from the optical detection unit to pass through as shown in Figure 3.5(b). A small spring secured the cantilevers onto the glass mount.

3.3.2 Optical Detection Unit

The optical detection unit was a converted NanoScope III AFM head (Digital Instrument, CA). As introduced in the detection method section, a laser beam emitted from a semiconductor laser diode was focused on the backside (opposite from tipped-side) of the microcantilever. The focused laser spot was about 20 μm in diameter. The reflected laser beam was projected onto the position sensitive detector (PSD). Any movements of the microcantilever inside the gas cell change the position of the laser spot on the PSD. The differential signals obtained from the upper and lower photo diodes of the PSD were amplified by a pre-amplifier (Preamp).

3.3.3 Four-point Resistance Measurement Unit

When the thin film resistance measurement experiments were conducted, the 4-point (wire) resistance measurement technique was used. Because the total length from one end of the V-shaped cantilever leg to the other was only about 500 μm, the resistance of the coating film on the cantilever was normally smaller than 10 Ω. Four 0.001-inch-thick copper wires were stresslessly attached to the base of microcantilever to make a four-point probe. The electrical contacts were made using silver glue. The four wires were carefully arranged to pass through a small gap between the top glass

mount and plastic sidewall without touching each other. Outside the gas cell the four wires were connected to a computer-controlled digital multimeter for measurement (details will be introduced in the data acquisition system section).

3.3.4 Gas Mix and Control Unit

The gas mix and control system included a stainless-steel tubing manifold using a MKS Flow Controller System that contained one MKS 4-Channel Readout (Type 247) unit and four MKS MASS-FLO® Controllers. Depending on the experiments, controllers with different flow rates were used. Three flow controllers were used with a maximum flow rate of 1000 ccm (Model: 1479A13CS1AM), 100 ccm (Model: 1479A12CS1AM) and 10 ccm (Model: 1479A11CS1AM). According to the manufacturer's manual, the MKS Type 1479A MASS-FLO® controllers have ± 1% full-scale accuracy (i.e. for 100 ccm unit the accuracy is about 1 ccm), less than 2 seconds settling time and control range from 2% to 100% full-scale.

A schematic diagram of flow control and gas mixture is shown in Figure 3.6. Pressurized pure nitrogen gas (99.99%), hydrogen gas (99.99%) and mercury/nitrogen mixed vapor were connected to the flow controllers Flow 4, Flow3 and Flow2 respectively. Regulated flows were mixed in a 0.25-inch-diameter stainless-steel tubing network that linked the flow controllers (The "dead" volume within the tubing network and flow controllers is about 10 cubic centimeters.). All these stainless steel tubes were connected to each other either by stainless steel couplers or T-connecters.

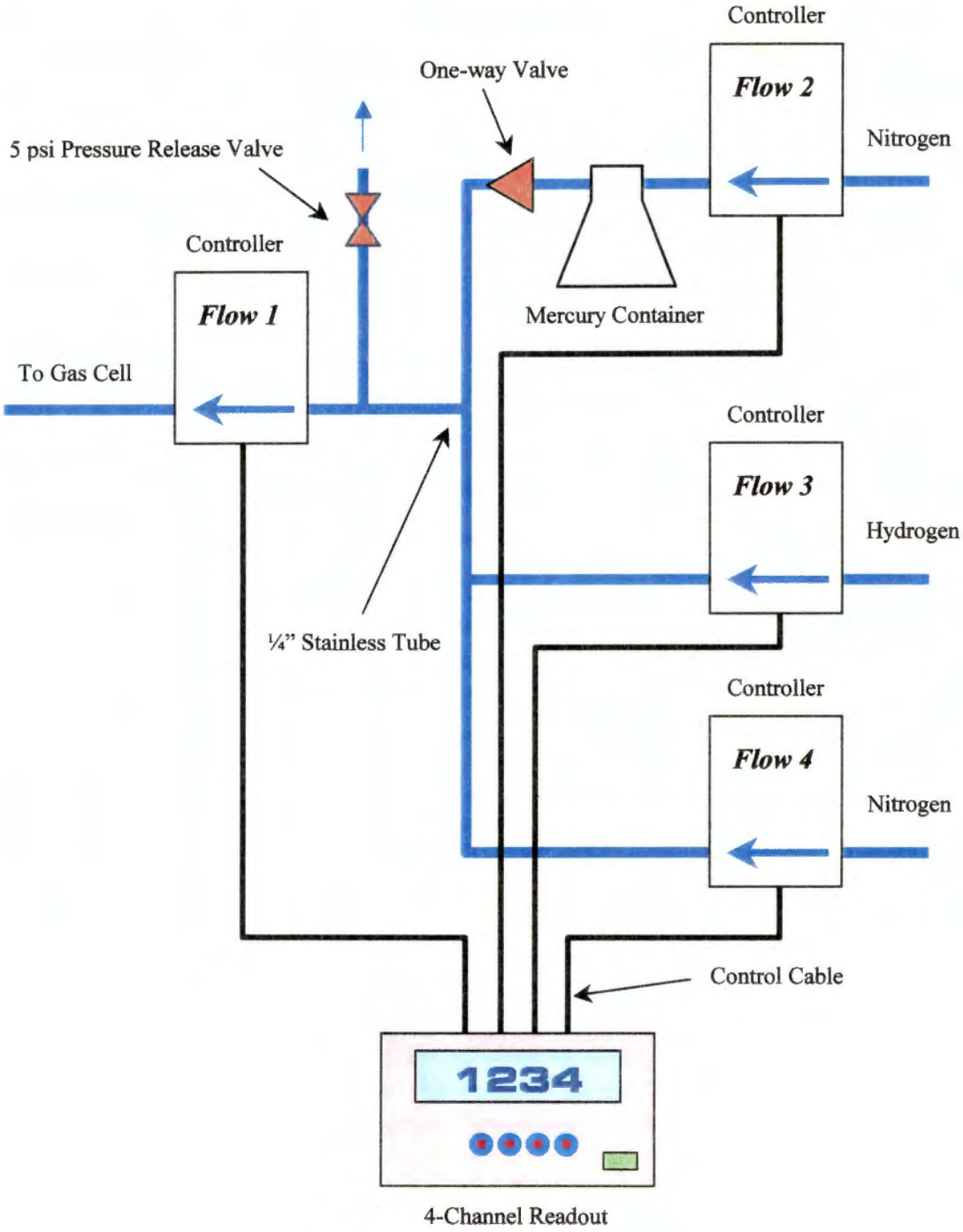


Figure 3.6: Schematic diagram of gas mix and control setup.

Before assembly, all parts were washed in warm soapy water a few times then rinsed with methanol in order to remove oil and dirt. After letting air drying all tubes and connecters were screw-tightened and no lubrication was used. A leakage check was performed. In order to have a steady flow into the gas cell and have minimum flow disturbance inside the gas cell, a 10-ccm flow controller (Flow 1) was employed and placed between the gas cell and the tubing network. Thus, the gas cell flow did not vary in spite of the flow changes of Flow 2, 3 or 4. The placement of Flow 1 not only ensured that experimental results would not be disturbed by the concentration changes, but it helped to minimize the noise induced by the flow turbulence.

Because the flow controllers a positive pressure gradient between intake and output, it is necessary to keep some pressures within the tubing network. Too much pressure can greatly reduce the efficiency of the mixing rate control or even shut down the system (when the pressure inside the tubing network is equal to the gas input end pressure). A 5-psi pressure-relief valve was use to vent flows in excess of that demanded by Flow 1. This exhaust was also used to monitor mercury concentrations by an independent instrument. (see below).

For hydrogen experiments, the hydrogen concentrations were determined by the flow ratio of Flow 3 and Flow 4. For example, 1% hydrogen concentration was obtained by setting 1-ccm hydrogen flow though Flow 3 and 100-ccm nitrogen flow though Flow 4.

For mercury experiments, the nitrogen gas through Flow 2 was sent to a container in which mercury was stored. Inside the container, mercury vapor mixed

with nitrogen gas exhausting through a one-way valve. A Jerome 431-X Mercury Vapor Analyzer (Arizona Instrument, Phoenix, AZ) was connected after the pressure release valve to determine the mercury/nitrogen vapor concentration t. The Jerome has a detection range from 0.000 to 0.999 mg/m^3 Hg with 0.001 mg/m^3 Hg resolution and 0.003 mg/m^3 Hg sensitivity. Its calibration was unknown.

3.3.5 Data Acquisition System

During the experiments, two data acquisition systems were adopted to collect experiment results. At the beginning a four-channel lock-in amplifier (Stanford Research Systems, Model SR850 DSP) was employed to record data. However, the built-in memories in this instrument limited the number of data points that could be taken and the time that experiments could run. Additionally, the lock-in amplifier only can receive ± 10 VDC voltage signals, and it cannot record or measure resistance.

Later we purchased a Hewlett Packard (HP) Data Acquisition / Switch Unit (Model: 34970A) with a 20-channel multiplexer (Model: 34901A), . This unit is controllable by a personal computer (PC, IBM compatible) and has three slots for plug-in modules for extend applications. The measurement results maybe displayed on the front panel of the data acquisition unit or be sent through a serial cable to the computer. Computer software provided with the unit turned the computer into a multi-channel data measuring, recording and analysis device. The biggest advantage of this system is that it can simultaneously measure and record results of more than one voltage or resistance signal (i.e., read signals from both optical detection unit and

resistance measurement unit.). Thus, both cantilever bending signal and film resistance changes can be observed at same time. In fact, this function allowed us to have the first side-by-side observation of thin film stress and resistance changes caused by gas adsorption.

In order to reduce the thermal effects in our experiments systems were allowed to warm up for a period of time before experiments. To minimize the temperature variations a sealed box was employed, and the room temperature was kept in a controlled manner.

3.4 Thin Film Preparation

Two metal thin films (palladium and gold) were prepared for most of the experiments carried out for this dissertation. Palladium-nickel, platinum and aluminum films were also tested in a few comparison experiments. At the beginning of the experiments an electron-beam-heated evaporator was used for film preparations. However, the evaporator required a better than 10^{-5} torr vacuum for evaporation and on averages it took up to 4 hours to pump down. Problems were encountered during the evaporation, as the electron-beam heated the samples to rather high temperature. The thermal radiation heat apparently caused unwanted stress build up in the coating layers. The cantilevers curled badly and sent the reflection beam out of the detectable range of the optical detection unit. Thus, low vacuum sputter coating systems were used to prepare the most palladium, gold, palladium-nickel alloy and platinum films on all commercially available microcantilevers and MUMPS cantilevers. The

electron-beam evaporator prepared only aluminum films on a few MUMPS cantilevers at limited occasions.

Sputter coating techniques were developed in the last century to prepare thin films on the object surfaces and various sputter deposition methods exist. [164] But no matter which method, the common goals are to generate and maintain a desired plasma and to establish a bias or electric field for the acceleration of ions from the source to the sample. During the ion bombardments, some ions lose energy and are deposited on the surface forming a film. One advantage of sputter coating is surface cleaning. Because the highly energized ions remove atoms from the sample surface, it actually cleans the sample surface before deposition. As with other thin film preparation methods, sputter coating also produces some stresses in the coating layers.[74] But as no high temperature was involved during the coating, these stresses were manageable and almost all cantilevers were useable after sputter coating.

The Hummer VI sputtering system (ANATECH Ltd, VA), which is magnetically enhanced, was employed to prepare palladium, palladium-nickel alloy and platinum films. The sputter targets were obtained from commercial sources (Pd: 99.99%; Pd/Ni: 90/10% wt.; Pt: 99.99%). Cantilevers were placed in the center of the vacuum chamber and a 3-inch x 1-inch cleaned microscope glass slide was also placed under or beside the cantilevers. The purpose of the glass slide was to check the coating thickness of the thin film afterwards by optical transmission.

Some pictures of coated cantilevers are shown in Figure 3.7. In the case of preparing films for 4-point resistance measurement, a very sharp V-shaped shadow

mask was made to place between the two legs of the microcantilever. As shown in Figure 3.7(b), the space (at the base) between the two cantilever legs was very small (less than 150 μm) and the size of the shadow mask had to be smaller than 100 μm. If the shadow mask was too small then it would not create enough shadow clearance on the cantilever base to prevent direct electrical conduction between two sides of measure points. Thus, making, placing the shadow mask and later attaching micrometer-sized wires was challenging, it was necessary to perform the entire operation under an optical microscope. A few micrometers offset could break the cantilevers or put shadow on wrong place. Learning to do this job and refining the necessary skills was time-consuming. Another shadow mask was also used for MUMPS microcantilever coating shown in Figure 3.7(c) & (d). In this case, wrongly located metal films could not only decrease measurement sensitivity but also displaced metal films could cause short circuits on the chip.

To sputter coat palladium films, the cantilevers were placed in the vacuum chamber, and the system was pumped down until a better than 40 mtorr vacuum was obtained. Then pure argon gas (99.99%) was released into the vacuum chamber at 200 mtorr to flush the chamber. After pumping down the vacuum to ~30 mtorr again, the high voltagewas turned on and argon gas leaked in. The coating current was maintained at about ~11 mA and coating time was recorded. Each time, the coating thickness was individually verified by checking the film reflection and the transmission index on the glass slide placed in the vacuum chamber besides the cantilevers. A Shimadzu UV-Visible Recording Spectrophotometer (Model: UV-250)

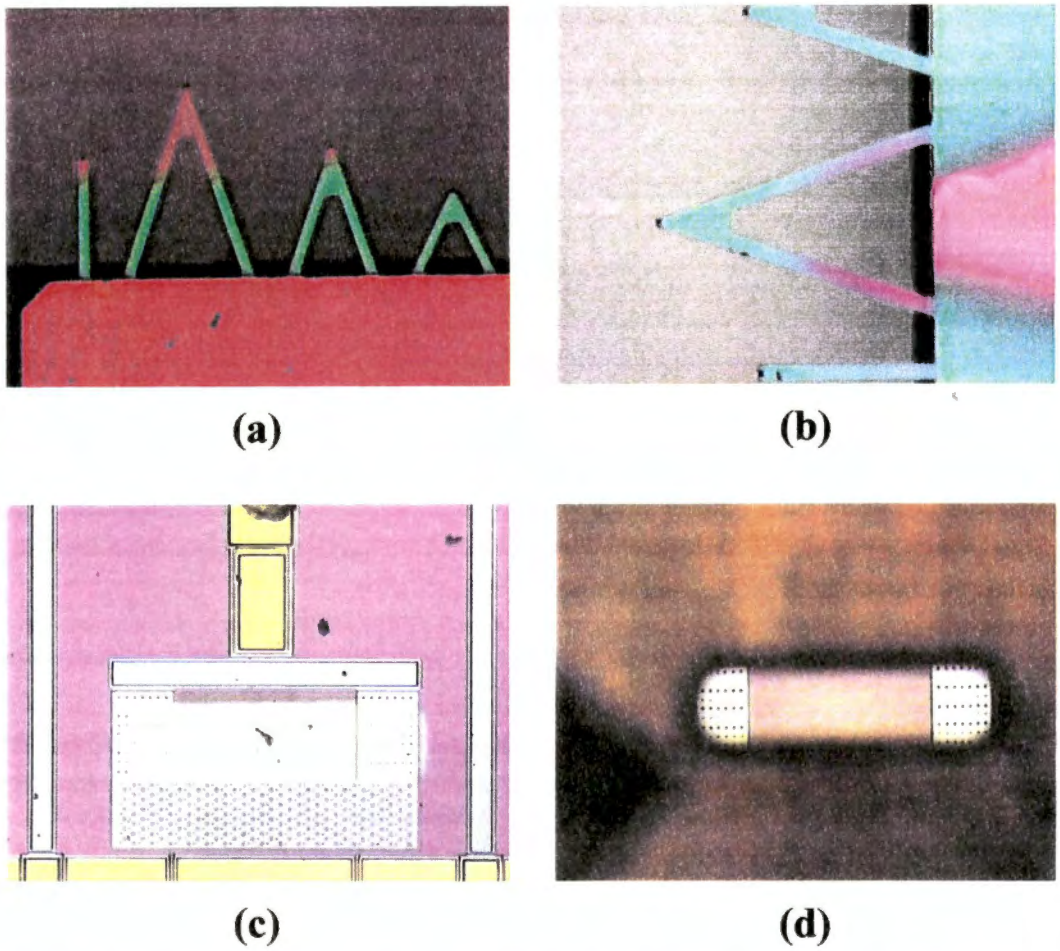


Figure 3.7: Coated microcantilevers. (a) Partially coated Microlevers; (b) Shadow masked C-type Microlever, the shadow between two legs forces electrical current passing through the cantilever arms (the uneven coatings on the legs were caused by the edge effects of the slightly offset shadow mask); (c) Gold film was shadow mask coated on MUMPS cantilever legs; (d) Shadow mask was placed on the top of a MUMPS cantilever.

was used to measure the reflection index at a wavelength of 500 nm and results were printed by Shimadzu Graphic Printer (Model: PR-1). Then film thicknesses were calculated by a computer program based on published optical indices. [165] The average palladium film thickness was founded to increase about 3 nm per minute. Similar procedures were taken to prepare palladium-nickel alloy and platinum films.

The sputter coating system used to make gold film is the Polaron SEM Coating System. Very similar steps have been taken during the coating, a quartz thickness monitor equipped with the system provided film thicknesses. The coating vacuum was set to 2 Pa and high voltage was set to2.5 KV.

3.5 MUMPS Chip Experiment

The MUMPS cantilevers and readout chips used in this project were designed by the Instrumentation and Controls (I&C) Division at Oak Ridge National Laboratory (ORNL). [43-45, 86] The fabrication of the cantilevers was done using the MUMPS (Multi-User MEMS Process) process at MCNC (now Chronos International Microsystems, Inc., Research Triangle Park, North Carolina). The MUMPS process is a three-layer polysilicon surface micromachining process. [48] More information about the MUMPS chip and its readout chip may be found in Appendix D.

There are thirty microcantilevers on each MUMPS chip, ten on each of three sides. Each cantilever is Π-shaped with two legs, 150 μm long by 100 μm wide by 2 μm thick. Two legs join a capacitive cross plate, 112 μm long by 500 μm wide and are anchored at the base of the legs 2 μm about the base plate. The chip was surface

mounted on the circuit board and connects to an eight-channel readout chip fabricated in a 1.2 μm bulk CMOS process. The typical readout noise of 1 mV corresponds to about 3 nm of cantilever deflection. Up to eight microcantilevers signals on one side of chip can be individually measured and readout. The coating on these cantilevers can be in any combination depending on the experimental requirements. For example, they can be coated by the same material but having different thicknesses or different materials with different thicknesses. A proximal shadow mask was utilized to ensure the coating area was only on the legs of the cantilevers. Before and after coating each channel was checked for shorts or opens. The entire circuit was powered by 4 AA-sized batteries and sealed in a grounded aluminum box to reduce the noise level. Mixed hydrogen or mercury-nitrogen vapor were sent in the box and results were recorded by the HP data acquisition system.

Chapter 4

ANALYSIS OF PALLADIUM-HYDROGEN SYSTEM

4.1 Introduction

In this chapter the bulk-like adsorption of gases in the thin metal films will be discussed. Because hydrogen can quickly adsorb into the bulk of palladium and much is known about this system, the palladium-coated cantilevers were selected. When palladium-coated cantilevers were exposed to hydrogen, expansion of the palladium layer caused the cantilever bending. Hydrogen adsorption-induced palladium thin film resistance changes were also observed.

At the beginning the historical background and properties of hydrogen adsorption in palladium will be introduced. Then experimental data of hydrogen adsorption-induced stress changes and thin film resistance changes will be presented with discussion and analysis. The last section of this chapter will present more detailed discussions about the observations. In an effort to understand the experimental results, a palladium surface model will be introduced followed by related considerations. Finally, the use bi-material microcantilevers as chemical and physical sensors will be discussed.

4.1.1 Palladium and Hydrogen

Palladium (symbol Pd) is a rare metal and was discovered in 1803 by Wollaston. Properties of palladium and hydrogen may be found in Appendix E. As an element it has 46 protons and is located in the group VIIIA of the periodic table. [166] In nature, most palladium is found in the ores of platinum. Although palladium has low electric conductivity (16% that of copper), it is valued for its resistance to oxidation and corrosion. [167] Palladium-rich alloys are widely use for low-voltage electric contacts, wires, instrument parts, dental plates, fountain-pen nibs and even jewelry. Palladium has the unusual property of adsorbing large volumes of hydrogen gas. Therefore it is also used to purify and to store hydrogen. [166, 168, 169]

Hydrogen is the first element in the periodic table and has very small atomic weight of 1.00797. Hydrogen was prepared many years before Cavendish recognized it as a distinct substance in 1766. Hydrogen is the most abundant of all elements in the universe, and it is thought that the heavier elements were, and still are being, built from hydrogen and helium. It has been estimated that hydrogen makes up more than 90% of all the atoms or three-quarters of the mass of the universe. The small weight of hydrogen in the gaseous state can make up very large volume and was a major fill-in material for balloons or dirigibles. But hydrogen gas is also highly flammable and becomes explosive when it is mixed in proper portion with oxygen or air. It has been used as fuel for space travel and missile propulsion for many years. Historically,

hydrogen explosions were blamed for many tragedies such as the explosion of the *Challenger* space shuttle and the *Hindenburg* disaster.

Detection of explosive levels of hydrogen gas has always been a safety concern. [170] Recent developments of hydrogen fuel cells promise a very environmentally friendly fuel source to power homes and automobiles. Therefore hydrogen will appear much closer to the general population than ever before. The need for a sensitive, small-size, low-cost, reliable hydrogen leakage detection unit is obvious.

4.1.2 Hydrogen Adsorption in Palladium

Gaseous state hydrogen has a unique ability to penetrate many solid metals directly. [122-124, 149, 151-155, 171] The absorption of molecular hydrogen by metallic palladium has been the subject of theoretical and practical interest for over a century. As hydrogen is absorbed, the metallic conductivity falls until the material becomes a semiconductor at a composition of about $PdH_{0.5}$. The adsorption of molecular hydrogen by metallic palladium has been observed and studied since 1866 when T. Graham reported that not only did palladium permit high throughput of hydrogen, but that large volumes of hydrogen (up to 935 times its own volume) were absorbed and formed "hydrogen alloys" (or "occlude" as Graham called it). Palladium is unique in that it does not lose its ductility until large amounts of H_2 have been absorbed. [172, 173]

When a metal surface is exposed to hydrogen gas, its surface adsorbs a thin layer of hydrogen molecules. An activated adsorption or chemisorption follows this surface adsorption where hydrogen molecules dissociate into atoms, then hydrogen atoms diffuse into the interior of the metal bulk and the so-called α- and β-phase hydrides are formed. [122-124, 149-155, 171, 174-176]

Palladium was the first element observed to form a metal hydride, and the palladium-hydrogen system has been heavily studied because of its suitability as hydrogen-storage system. In addition, the interaction of H with Pd surfaces has drawn much attention in connection with hydrogenation catalysis, electrolysis, and hydrogen purification. There are many reports of hydrogen adsorption in Pd and Pd alloys and their applications as chemical sensors. [45, 49, 65, 90, 94, 95, 100-102, 108, 111-113, 122, 124, 130, 134-136, 144, 146, 149, 151, 173, 174, 177-193]

Hydrogen adsorption in palladium can cause expansion up to 10% by volume. [172] Dissolving n hydrogen atoms in a metal changes the volume V of the metal by

$$\Delta V = n\Delta v \tag{4.1}$$

where Δv is the characteristic volume change per hydrogen atom and it is directly related to the mean partial molar volume $V_M = \Delta v \cdot L$ (L is Avogadro's number). [171] For a metal crystal with the volume V containing N metal atoms, the mean atomic volume of a metal atom is Φ. Thus $V = N \cdot \Phi$ and the relative volume change due to an atomic fraction $\zeta = n/N$ hydrogen atom is

$$\frac{\Delta V}{V} = \zeta \frac{\Delta v}{\Phi} \tag{4.2}$$

The length change for small volume changes (expansion coefficient) is then about one third of volume change

$$\frac{\Delta L}{L} = \frac{\zeta}{3}\frac{\Delta v}{\Phi} \qquad (4.3)$$

In general, hydrogen atoms have a high mobility within the lattice and diffuse rapidly through the metal. [122-124, 139, 150-155, 171] According to the data collected [171], at room temperature the value of $\Delta v/\Phi$ is about 0.2 in α-phase. A relative length change typically caused by a hydrogen atom concentration $C \approx 2000$ ppm (part-per-million) is about $\Delta L/L = 10^{-4}$ for a sample $Pd_{0.9}Ag_{0.1}$ where $L = 1$ cm. [171]

4.1.3 Hydrogen Diffusion in Palladium

It is believed that adsorbed hydrogen molecules (H_2) dissociate at the outer surface of palladium to form hydrogen atoms (H_{atom}). Hydrogen atoms then quickly move between palladium atoms and diffuse into the bulk. This is a reversible process and hydrogen atoms reassociate again (recombination) becoming hydrogen molecules at the surface. [94, 95, 193, 194]

$$H_2 \leftrightarrow 2H_{atom} \qquad (4.4)$$

When hydrogen atoms diffuse into thin palladium coating layer on Si or Si_3N_4 substrate, it may be considered as non-steady state one-dimensional diffusion into a medium bounded by two parallel planes. Because the interface between palladium

and silicon (or silicon nitride) is almost impenetrable for hydrogen gas, [94, 95, 193, 194] it can be treated as an impermeable boundary for hydrogen.

At room temperature (T = 25 ^{0}C), the diffusion coefficient for hydrogen diffusing into single crystal palladium is about $D = 1.6 \times 10^{-7}\ cm^2 s^{-1}$. [171, 173] In contrast to palladium, silicon and silicon nitride have orders-of-magnitude smaller diffusion coefficient and solubility. [94, 95, 131, 147, 193]

Using the above values for thin coating film Eq. (2.24) was evaluated numerically with the concentration at the gas-solid interface and diffusion coefficient as constants. The hydrogen-concentration distribution diagram within the film as a function of time t is shown in Figure 4.1. More details about this calculation may be found in Appendix A. Here it is assumed that the palladium surface is ideally "clean" even though the surface conditions in experiments were not so ideally. This will be discussed more in the later part of this chapter. It can be seen that initially hydrogen atoms are concentrated at the hydrogen/palladium interface (where x/d = 0). As diffusion proceeding, the distribution becomes more even throughout the entire volume. Theoretically, it should take an infinitely long time for the concentration at the impermeable surface to reach the same level as the concentration C_0 at the hydrogen/palladium interface.

For a particular location x the concentration depends only on the time t. When the outside hydrogen pressure changes, the concentration C_0 at the gas-solid interface changes accordingly. Shown in Figure 4.2 is that concentration distribution was plotted as a function of time at $x = d$ surface.

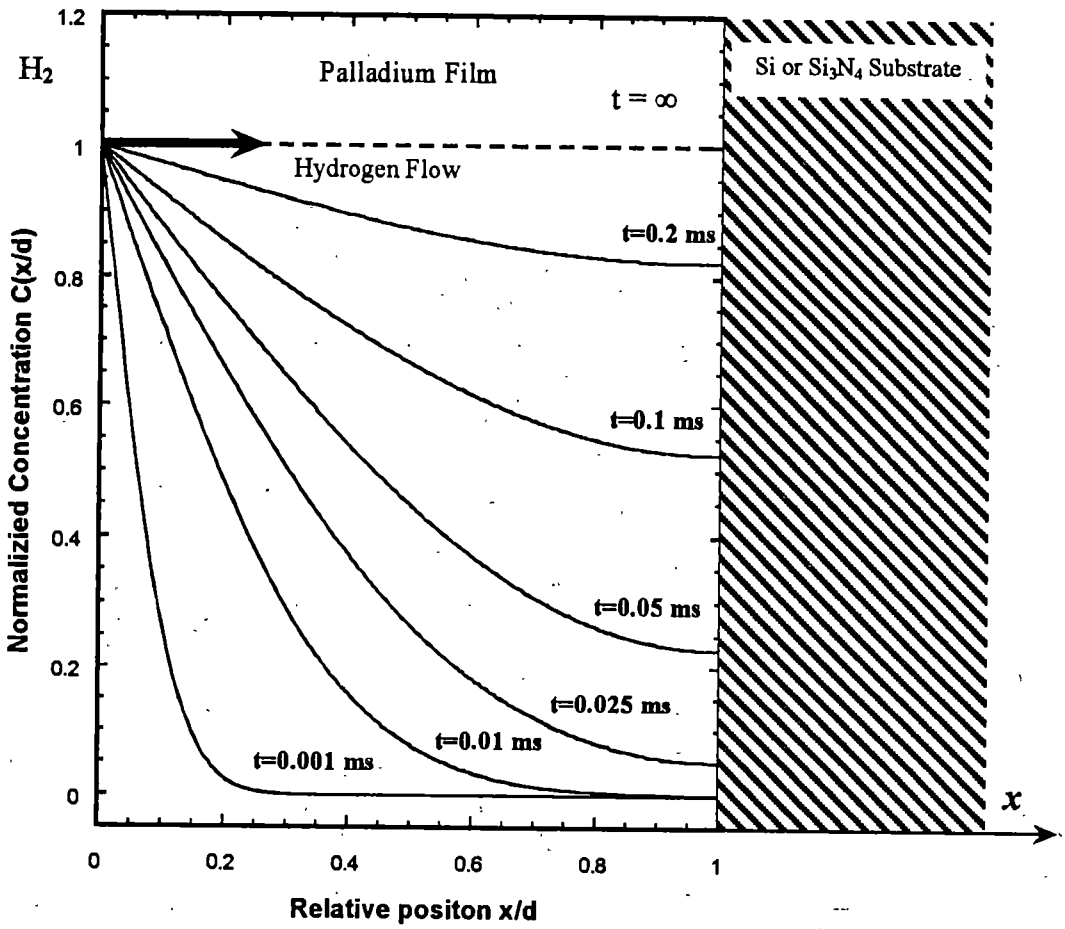


Figure 4.1: Hydrogen atom concentration distribution diagram at different time t in a plane sheet. One normalized constant surface concentration is at one surface and one impermeable layer is at another surface. Here, the diffusion coefficient for hydrogen-palladium system D is a constant and is equal to 1.6×10^{-7} $cm^2 s^{-1}$. The sheet thickness is d.

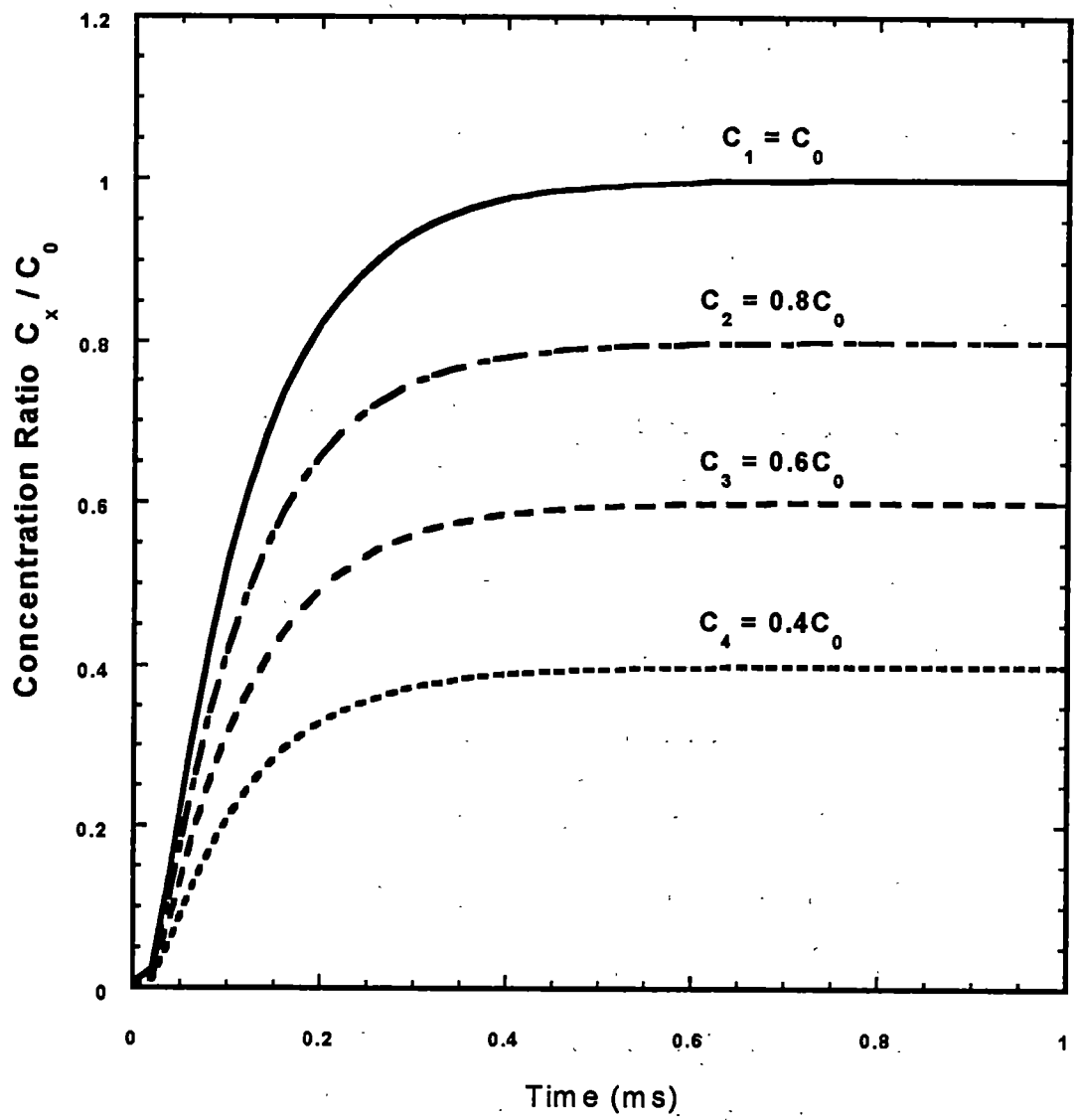


Figure 4.2: Concentration distribution as a function of time at $x = d$ surface.

We have used sputter-coated films in our experiments. Sputter coated and sputter coated thin films are polycrystalline. [195-197] Previous studies have found that hydrogen diffusion coefficient in singly crystal palladium is a constant of hydrogen pressure but it can vary in as much as two orders of magnitude for polycrystalline palladium. [143, 198] Therefore, shown in Figure 4.3, the concentration distribution curves are plotted with different diffusion coefficients (D_1, D_2, D_3 and D_4) plotted at different surface concentrations (C_1, C_2, C_3 and C_4). Obviously, the smaller the D is the longer time is needed to reach equilibrium. The reported experiments show that hydrogen adsorption the process appeared faster than its desorption process in palladium. [94, 95, 152, 193, 194] Thus, the case is illustrated where diffusion coefficients are different for hydrogen adsorption and desorption. The coefficients are labeled as D_{A0} and D_{D0} respectively. Here, the adsorption diffusion coefficient is three times faster than the desorption diffusion coefficient ($D_{A0} = 3D_{D0}$). From this plot it is clear that smaller C and D have lower maximum positions and a longer time is needed to reach the equilibrium position. The curves shown in Figure 4.3 are similar to the experimental results observed except that the time constants are much shorter. More details and discussions will be introduced later.

4.2 Hydrogen Adsorption-Induced Stress in Palladium Film

Using the properties of the palladium volume expansion on dissolving hydrogen, bi-material strips composed of palladium and another low hydrogen permeabe

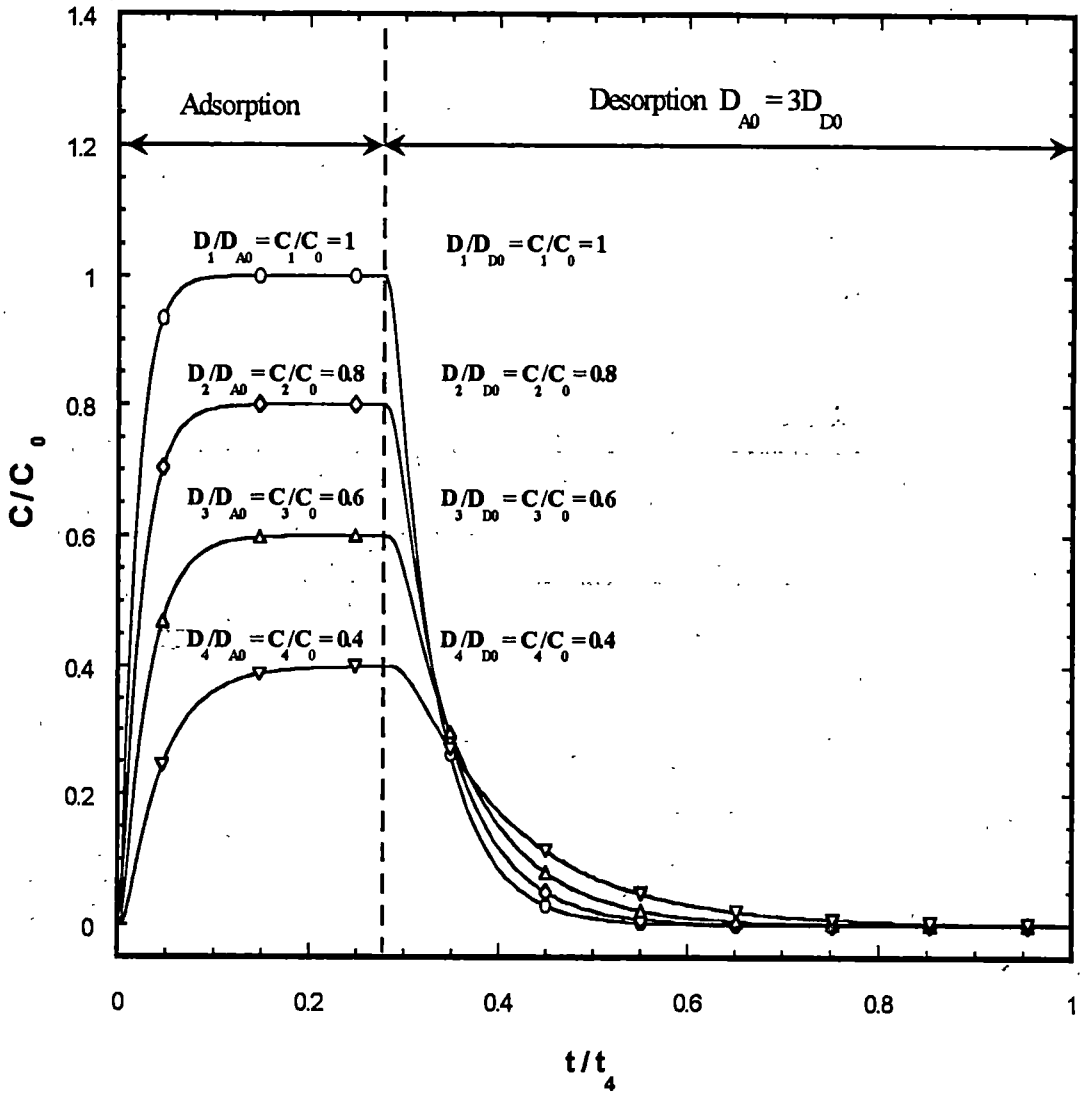


Figure 4.3: Hydrogen diffusion in and out curves with different diffusion coefficients and in-take surface concentrations. Here the diffusion coefficients for the hydrogen in-take are three times faster than the diffusion coefficients for hydrogen out-take.

material (such as Si or SiN) can be used to detect hydrogen as well as study the adsorption induced stress changes. [92] Taking advantage of the small spring constant (< 1N/m) and small size of microcantilevers, bi-material microcantilevers have ultra-high force and stress sensitivity. Since the optical detection method is capable of picking up sub-Å vertical displacements at the end of the cantilever, it is possible to study very small stress (pN level) variations on the microcantilever. For example, for a 100-μm long cantilever with 0.5 N/m spring constant, 1 Å stress-induced deflection corresponds to a force of about 50 pN (1 pN = 10^{-12} N) along the cantilever length or 0.5 pN/μm per unit length. Then the work done by the force is equal to $W(work) = F(force) \times Z(displacement) = 5 \times 10^{-21}$ J.

4.2.1 Hydrogen Adsorption Induced Cantilever Bending

As expressed in Eq.(2.9), the end displacement of a cantilever is proportional to the hydrogen atom concentration inside the palladium, which for low concentration is proportion to the external hydrogen pressure. [122, 123, 152, 171, 173] Thus, the bending of a palladium-coated cantilever should directly indicate the hydrogen atom concentration inside the palladium film and reflect the hydrogen pressure changes in ambient conditions. In Figure 4.4(a), a palladium-coated microcantilever (D-type Ultralever, 8.5 nm Pd-coated) has been exposed to about 0.98% hydrogen/nitrogen mixed gases. The bending voltage (left y-axis), which measures the cantilever bending, increases as hydrogen is introduced into the system and returns to the starting

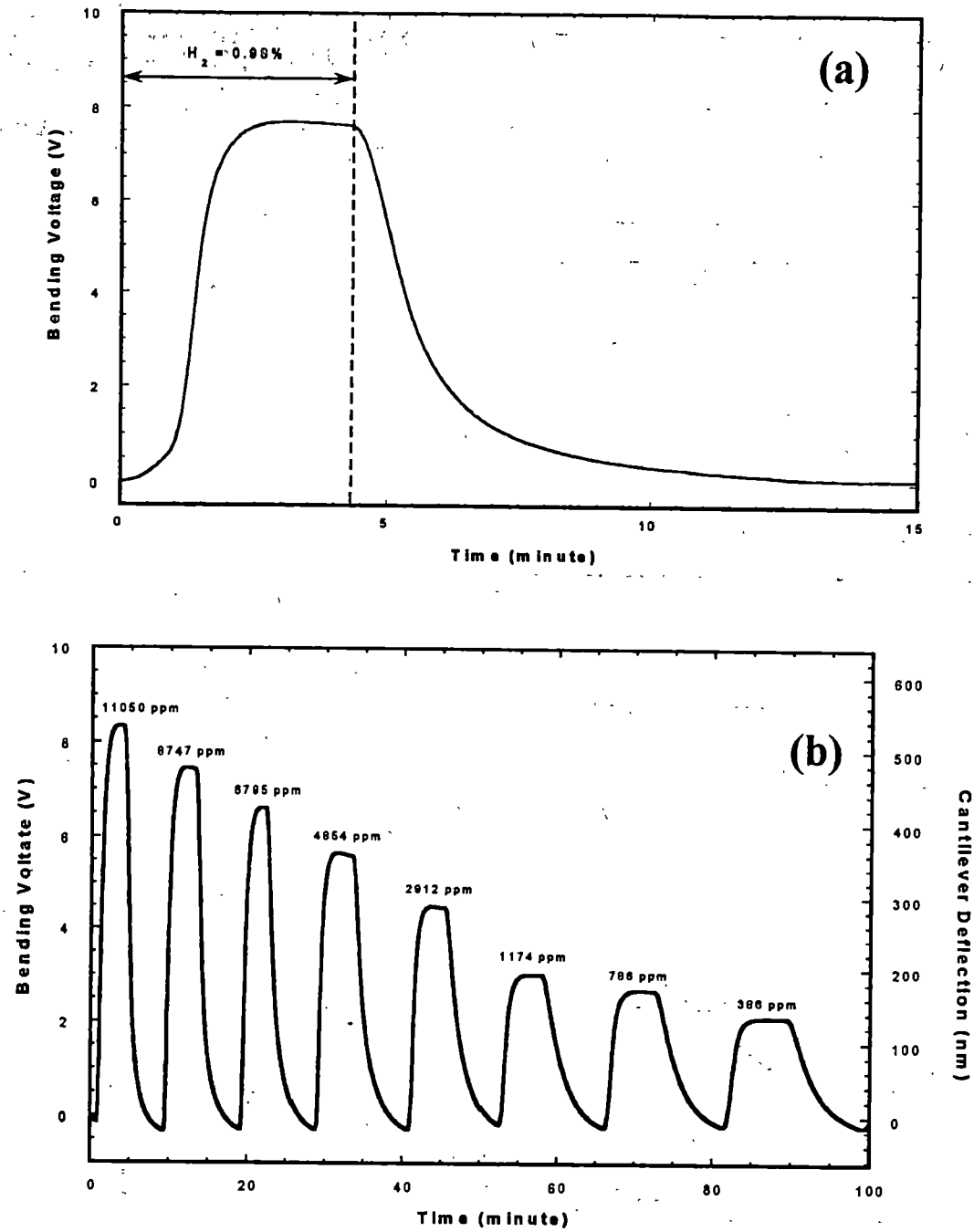


Figure 4.4: Palladium-coated microcantilever bending in hydrogen gas.

(a) Typical responses of palladium-coated cantilever in hydrogen gas.
(b) Typical responses of palladium-coated cantilever in various hydrogen concentrations. (D-type Ultralever, 8.5 nm Pd-coated)

level after removal of hydrogen. The corresponding cantilever deflection is marked on the right y-axis in nm. It is also noticed that the cantilever stops bending (flat top) after a short time even though same hydrogen concentration was maintained. The hydrogen's partial pressure in the gas cell decides the hydrogen atom concentration in palladium film. [173] Consequently, the maximum deflection of cantilever is decided too according to the bi-material cantilever theory. When the hydrogen concentration was changed as shown in Figure 4.4(b), different maximum bending positions were observed corresponding to hydrogen concentrations.

Comparing the two figures in Figure 4.4 with the theoretical calculations of hydrogen diffusion in palladium (Figure 4.3), an excellent match can be observed. Especially, in Figure 4.4(a) it took much longer time (about four times longer) for the cantilever return to its original position than bend to the maximum amplitude. From the diffusion equations this requires that the diffusion coefficients be different for in and out processes. The diffusion-out coefficient is much smaller and hydrogen atoms need much longer time to diffuse out of palladium film than to diffuse into the film.

According to the hydrogen diffusion calculation shown in Appendix A, for a micrometer-thick film the diffusion time to reach equilibrium should be within 1 ms. The similar experiments of hydrogen adsorption on clean surfaces confirmed that the adsorption and desorption processes can be very fast (milliseconds) in ultra-high vacuum (UHV) environment. [199] However, time measured from Figure 4.4 was in minutes. To explain this big difference, it is necessary to remember that the reported diffusion coefficient was obtained from clean surfaces in UHV environment. In order to simulate the field conditions for future applications, the samples had been exposed

to atmosphere before and between experiments. Layers of other materials such as water and oxides are expected to be found on the film surface. In another words, the "real" surfaces were used and they were not "clean" (in UHV standard). The existence of those layers can significantly reduce the hydrogen penetration capability and slow down the entire process. The origin of water layer could not only came from the humidity found in the atmosphere, it was known that hydrogen atoms and oxygen atoms could form water molecules too. [82] Second, it was assumed that the diffusion coefficient was not depended on the hydrogen pressure. That is clearly not the case for sputter coated polycrystalline palladium film. [143, 198] Actually, if the value of diffusion coefficient is reduced to two orders lower, using the calculation shown in Appendix A the time constant increases about two orders too. Finally, as mentioned before, there is a chemical reaction that takes place at the gas/solid interface. Hydrogen molecules first need to dissociate into elemental hydrogen atoms before diffusion into the solid can take place. This is a complex chemical process and the mechanisms involved are still under study. The time constant for this process is not quit clear yet at this point. A palladium surface model will be introduced in the discussion section of this chapter. This model will be used to explain the experimental observations.

It was found that not only the cantilever bending amplitude was a function of hydrogen concentration but its bending rate (the speed of bending) was also a function of hydrogen concentration. As shown in Figure 4.5(a), both bending amplitude and bending rate were plotted vs. the hydrogen concentration in the gas cell. From

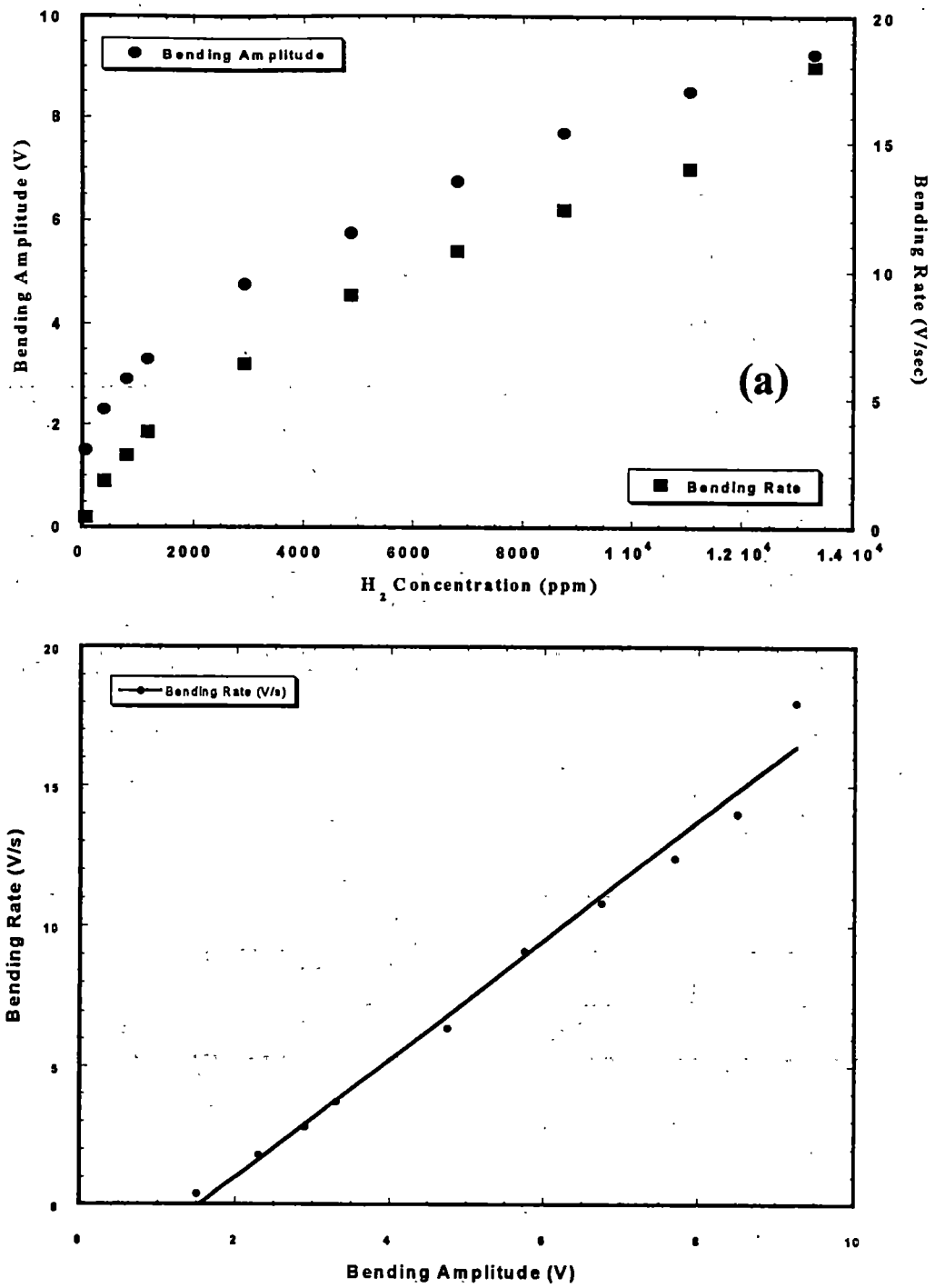


Figure 4.5: Cantilever bending amplitude and bending rate. (a) Cantilever bending amplitude and bending rate vs. hydrogen concentration in the gas cell. (b) Cantilever bending amplitude as a function of its bending rate.

Figure 4.5(a), it can be seen that excellent one-to-one correspondence exists between the cantilever bending rate and bending amplitude. This means that hydrogen concentration can be obtained either by measuring the maximum deflection signal (take longer time) of a cantilever sensor or by measuring the speed of its bending (take short time). The plot shown in Figure 4.5(b) shows this more directly; a linear function exists between the bending amplitude and bending rate over a large range. The non-linear relation at the high hydrogen concentration end (right side of the plot) is due to the slow acquisition rate that was not sufficient for the first derivative calculation. Another important observation of Figure 4.5(a) is that the points in this plot were not in a straight line. Therefore, the bending amplitude (or bending rate) was not a linear function of the detected hydrogen concentration. It appears that two basic slopes were followed. When the concentration is smaller than 2000 ppm, the slope was bigger. For higher concentration a lower slope is observed. This may be evidence of palladium α- to β-phase transaction process. If so, the hydrogen concentration at which the transaction occurred was much lower than what had been reported in literature. [149, 152, 153, 171, 173]

4.2.2 Hydrogen Charge and Discharge Time

If folding diffusion-in and diffusion-out curves together as shown in Figure 4.6(a), the difference of the cantilever bending rates for adsorption and desorption under various concentrations can be seen much easier. The hysteresis loops suggest

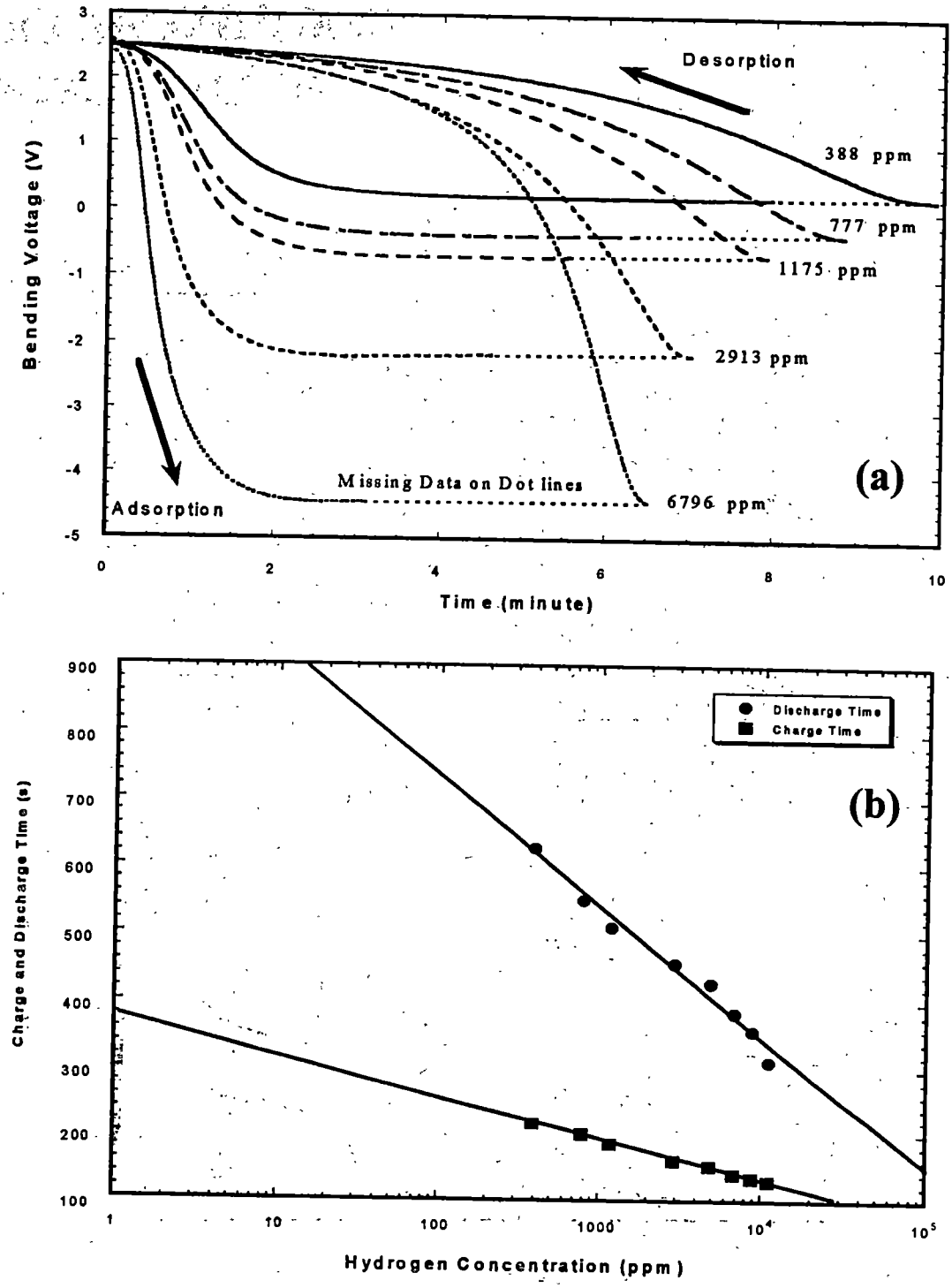


Figure 4.6: Hydrogen charge and discharge rate. (a) Hydrogen charge and discharge hysteresis loop. (b) Hydrogen charge and discharge time vs. concentration.

that the mechanisms of the palladium thin film expansion and contraction processes are different. Two conclusions may be proposed here:

(1) Hydrogen adsorption in palladium is dependent upon hydrogen concentration (partial pressure);

(2) The time needed for adsorption is not same as the time needed for desorption. According to our experimental results, the time needed for desorption process is about 2~5 longer than the time needed for adsorption process. This difference may imply the existence of different coefficients for adsorption and desorption.

To show these two points more clearly, in Figure 4.6(b), the charge time (the time for cantilever reaches the maximum bending position) and discharge time (the time for cantilever returns 90% of its start position) were plotted against the hydrogen concentration in the gas cell (note X-axis is logarithmic) using data obtained from Figure 4.4(b) After curve fitting, two experimental equations are obtained from this plot.

(1) Charge time T_{charge} expressed as a function of the concentration in the gas cell C_{GC} (ppm) is

$$T_{charge} = 370.87 - 59.914\ log\ C \quad \text{(s)}; \tag{4.6}$$

(2) Discharge time $T_{discharge}$ expressed as a function of the concentration in the gas cell C_{GC} (ppm) is

$$T_{discharge} = 1112.1 - 194.09\ log\ C \quad \text{(s)}. \tag{4.7}$$

The microcantilever used in these experiment was silicon 85 μm long Ultralever (D-typed) with 2.1 N/m spring constant and 8.5 nm palladium coating layer on one side. Above two equations show that at lower hydrogen concentration the cantilevers need longer time to reach the maximum position or restore to their start positions. Using Eq. (4.6) and (4.7) T_{charge} and $T_{discharge}$ for different C_{GC} were calculated and the results are presented in Table 4.1.

It is important to point out that T_{charge} and $T_{discharge}$ not only depend on the physical properties (i.e. spring constant and size etc.) of the cantilever but also depend on the surface conditions of the film and the thickness of the film (this point will be discussed later). The values in the table may change from one cantilever to another in a wide range and can only be used as guide line for better understanding of these phenomena. M is a parameter used to describe how long the discharge time is when it is compared to the charge time under same conditions. In general, M varies from 2 to 5 for over all experimental results obtained in this dissertation. It should be noticed that $T_{discharge}$ becomes a negative value when C = 100 %. This is understandable because Eq. (4.6) & (4.7) were obtained from the experiments conducted when C was less than 1.2 %. For higher concentration, the transition of α-phase and β-phase totally changes the expansion mechanism and can cause damage and deformations in palladium.[149, 174] Then the above equations are no longer applicable in this region.

Table 4.1: Hydrogen Charge / Discharge Time

C_{GC} (ppm)	T_{charge} (s)	$T_{discharge}$ (s)	$M = T_{discharge} / T_{charge}$
1,000,000	11.39	- 52.44	-4.60
100,000	71.30	150.65	2.11
10,000	131.21	344.74	2.63
1,000	191.13	538.83	2.82
100	251.04	732.92	2.92
10	310.96	927.01	2.98
1	370.87	1121.10	3.02
0.1	430.78	1315.19	3.05
0.01	490.70	1509.28	3.08
0.001	550.61	1703.37	3.09
0.0001	610.53	1897.46	3.11

4.2.3 Coating Film Thickness Dependence

Because of the individual differences among the commercially available cantilevers, and because experimental conditions might change from the time-to-time, it is difficult to draw any meaningful conclusion from the results of different cantilevers and experiments. The MUMPS chip offered a unique opportunity to simultaneously investigate eight identical microcantilevers on one chip. Therefore, MUMPS chip is an ideal platform for comparison experiments.

Shown in Figure 4.7(a) were the effects of coating thickness observed in MUMPS chip experiments. Three microcantilevers were sputter coated with palladium films that have thicknesses of 15 nm, 30 nm and 45 nm respectively. It is easy to see that the cantilever with thicker coating layer took longer time to reach the maximum bending position than the cantilever with thinner coating layer. The same observation may be found in discharge period. But the cantilever with the thicker coating had larger bending amplitude than the thinner ones. More evidence of the above observations may be found in Figure 4.7(b) when three cantilevers were repeatedly exposed to 1% hydrogen gas. This figure also shows that the responses of three cantilevers to the same hydrogen concentration were uniform with better than 95% repeatability.

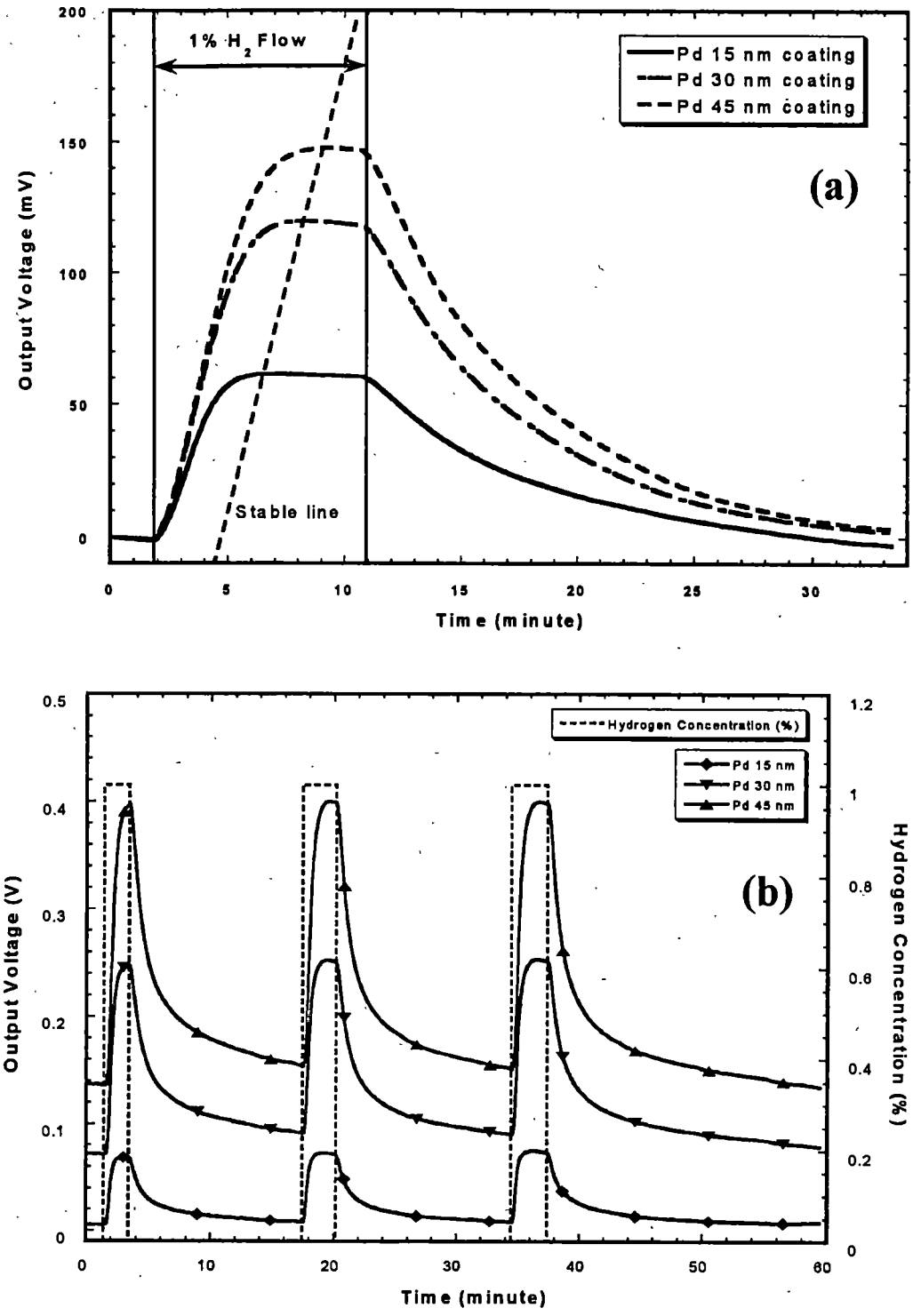


Figure 4.7: Bending respondents of cantilevers with different thicknesses of Pd films to 1% hydrogen (a) one time and (b) repeatedly.

Cantilever with thicker films bent further under same hydrogen concentration that suggests:

(1) Hydrogen adsorption inside palladium films is bulk-like adsorption. The adsorption process is dependent on the film thickness.

(2) Hydrogen atoms did not stop at the gas/solid interface. The atoms actually penetrated the entire thickness of the films.

(3) The overall adsorption and desorption time is much longer than the time suggested by the diffusion model.

(4) The sensitivity of coated cantilevers is adjustable in a certain range by controlling the coating layer thickness.

The theoretical model for the bi-material cantilever suggests the existence of an optimal coating thickness for best sensitivity. Trying to verify this point, a series of experiments were conducted to study the thickness effects. An extended range of thicknesses is shown in Fig. 4.8. The experimental data were collected from nine different cantilevers (Ultralever, D-type) with more than twenty coating thicknesses (some of them were coated more than once). Also shown is a normalized comparison with Eq.(2.9). The functional form in Eq.(2.9) is not clearly apparent and additional data with increased Pd thicknesses must be acquired to observe the expected maximum in sensitivity. However, with limited time and resources (the costs of materials, equipment and human efforts) during the experiments reported in this

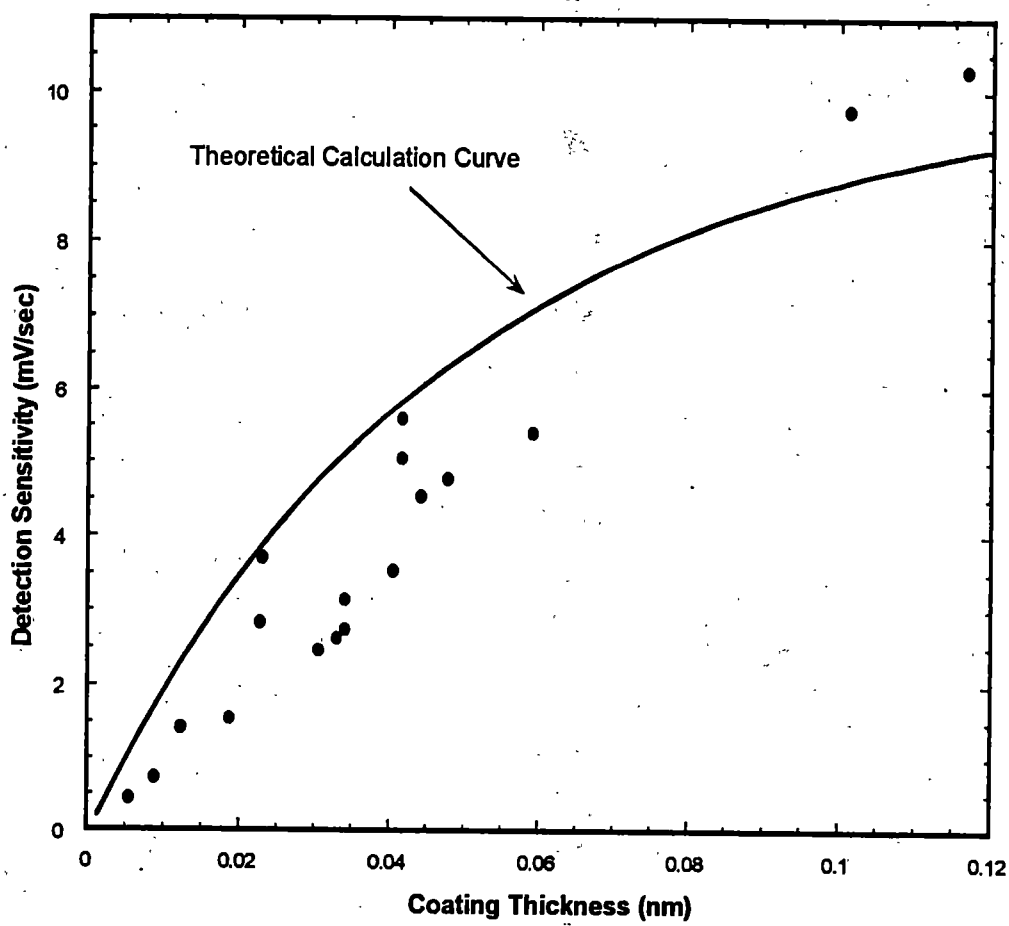


Figure 4.8: Bending rate sensitivity vs. thickness ratio.

dissertation prevented further investigation in this subject. According to literature, other groups have done similar thickness dependence experiments and their results confirmed a similar theoretical model. [50]

4.3 Hydrogen-Induced Resistance Changes in Palladium Film

It is well known that hydrogen adsorption in palladium and its alloys can cause electrical resistivity changes. In fact, several hydrogen sensors have been developed exploiting these adsorption-induced resistivity change. [99-102, 105, 106, 122-124, 130, 133, 136, 140, 151-153, 171, 173, 179, 180, 200, 201] To confirm if this is still true for the thin palladium we prepared, a strip of palladium film (15 mm long, 2 mm wide and 45 nm thick) was sputtered on a SiN substrate along with shadow-masked microcantilevers. The typical resistance (4-point method) changes are plotted in Figure 4.9 when the palladium strip was exposed to hydrogen gas. The y-axis in this plot is the percentage change of film resistance with a starting resistance of 72.1 Ω. A comparison experiment was performed to make sure that the film resistance on the coated cantilever behaves in same manner as the filmstrip. The results are shown in Figure 4.10(a) & (b). The same responses are observed in both cases except the signal obtained from the cantilever was much noisier than the one obtained from the strip. This is understandable since the resistance on the cantilever was only 5.6 Ω, and the cantilever was bending during the experiment.

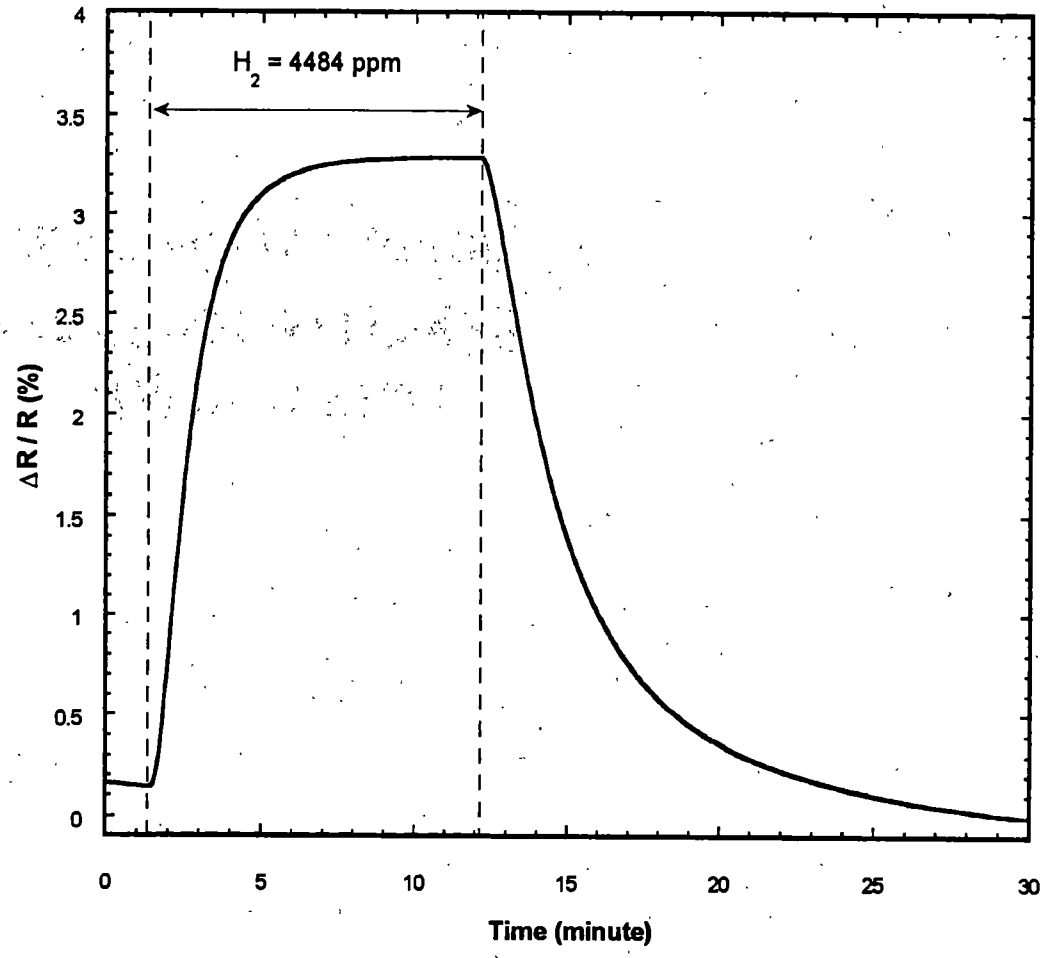


Figure 4.9: Typical palladium resistance responses to hydrogen.

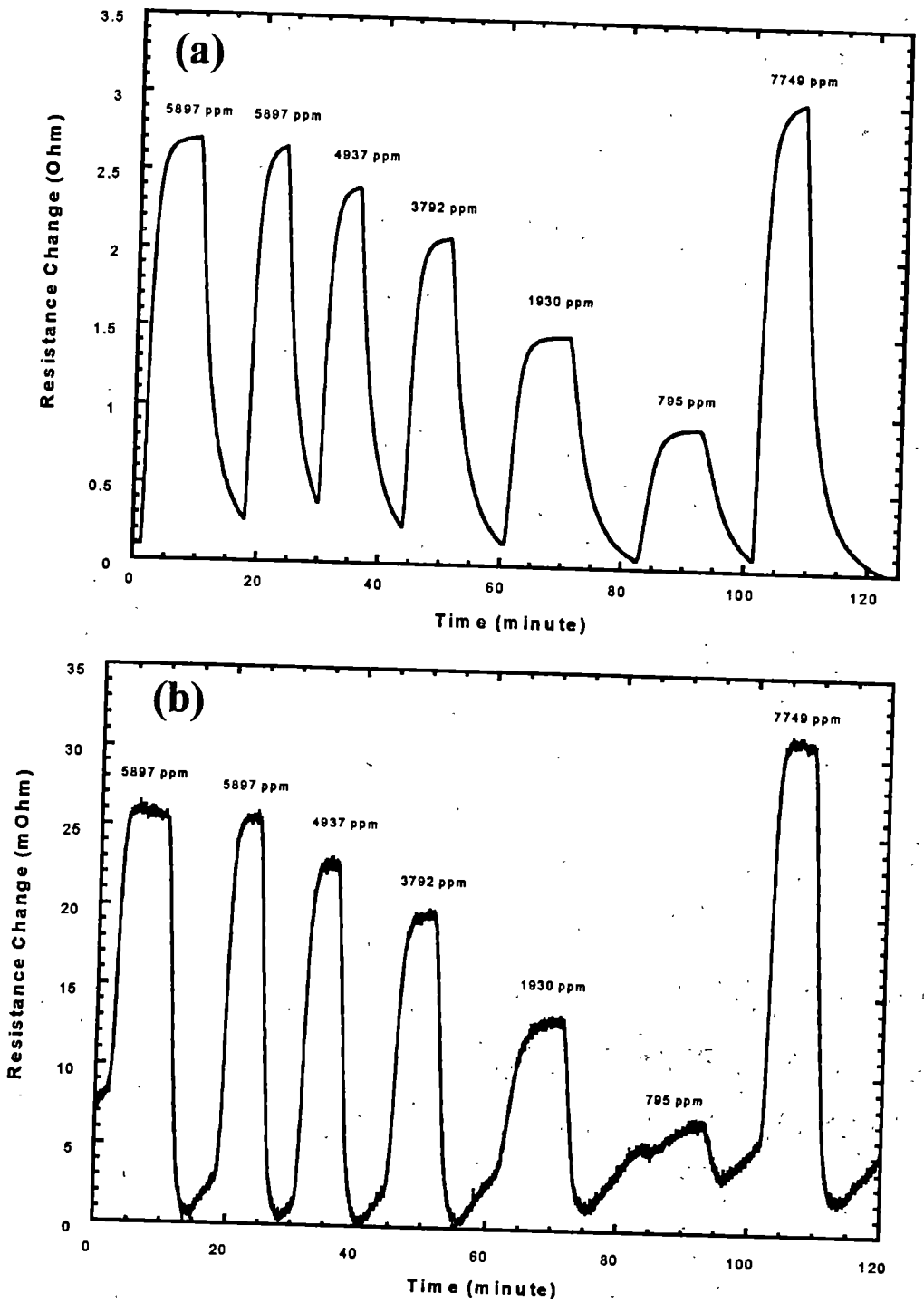


Figure 4.10: Palladium film resistance responses to hydrogen. (a) On the strip and (b) On the cantilever.

The shape of this resistance curve and the shape of the bending response of palladium-coated cantilevers appear very similar. This indicates that the hydrogen adsorption in palladium produced similar changes in both film stress and film resistance. It will be interesting to see how closely these two very different properties are related. Using both the optical detection method and the 4-point resistance method, the cantilever bending and its coating layer resistance change can be measured simultaneously.

The results of the measurements are shown in Figure 4.11. Two curves appear to have the same qualitative shape. However, the stress-induced cantilever bending (dashed line) has a different time constant from that of the film-resistance variation (solid line). This observation was not anticipated; since it is hard to image that the very same hydrogen atoms can cause two effects at different rates. Furthermore, as shown in the figure the time constants of stress and resistance variations are variable under different hydrogen concentrations. More importantly, this observation implies that the mechanical response can be faster than the electrical response under certain conditions. This conclusion is troubling because the electrical response should faster than the mechanical response. These experiments are believed to be the first observation of these phenomena. As no existing theories and models can be used for explanation, further investigation and more experimental data are needed before better and deeper understanding of this problem can be established.

Out of curiosity, another experiment was performed in a similar way and tried to see whether the same results can be obtained. This time a platinum film was

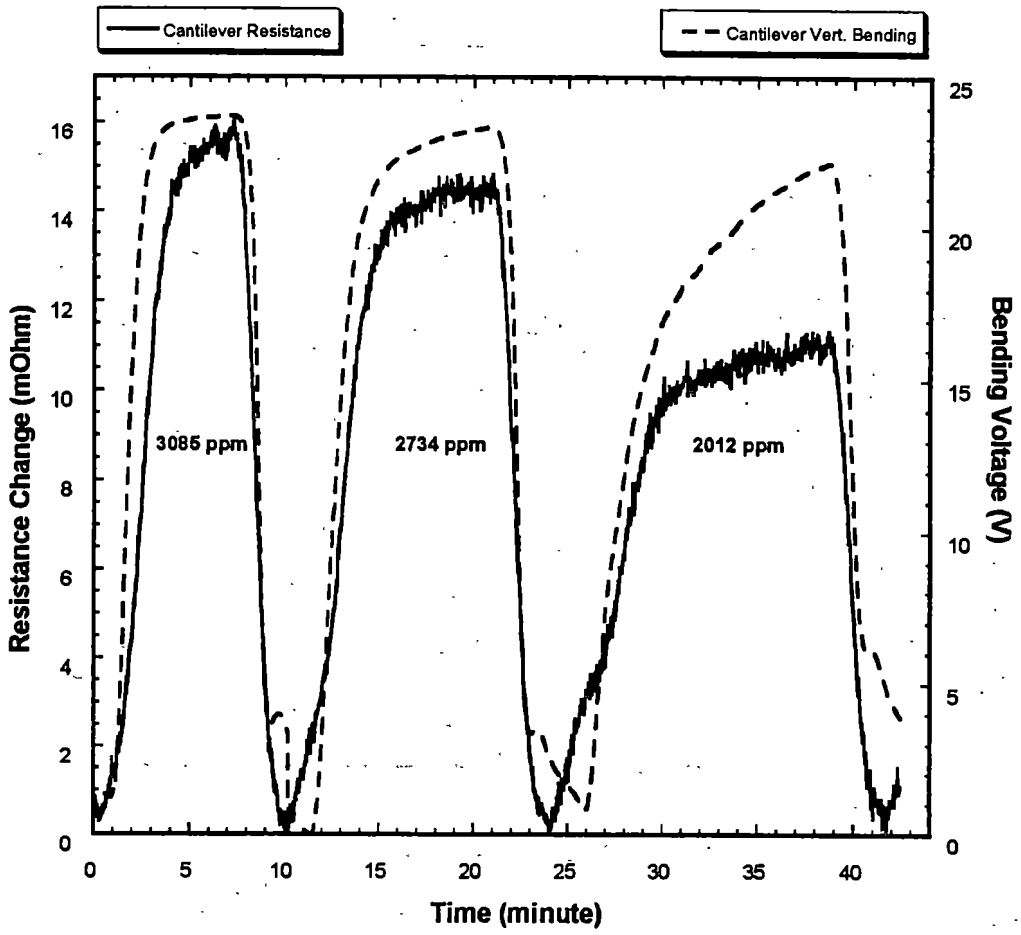


Figure 4.11: Cantilever bending and resistance response to hydrogen.

exposed to hydrogen gas instead of palladium film. A similar result for the time constant discrepancy was observed. However, the resistance of platinum film decreased when hydrogen gas was introduced into the gas cell. The variation of platinum film resistance was not only in the opposite direction as that of palladium film, but also opposite to that predicated by the theory of electron conductivity. The electron conductivity theory states that the impurities (such as hydrogen atoms) inside the metals cause more scattering of electrons and reduce the mean free path. As a result, higher resistivity should be observed. It is possible that the stress may play a role in it as the stress in thin films can also induce variation of electrical resistance. [72]

4.4 Discussions

4.4.1 Hydrogen Adsorption in Palladium

From the above experimental results and analysis, it can be seen that the adsorption of hydrogen in palladium is not a simple diffusion process. Its complex mechanisms involve changes in electrical and mechanical properties. Bi-material microcantilevers have very high stress-sensitivity. As shown in Figure 4.12 the deflection of the cantilever is very sensitive to low hydrogen concentration changes. Part-per-million (ppm) levels of hydrogen can be easily detected by a palladium-coated cantilever. In fact, there exists almost a linear response between the cantilever deflection and low hydrogen concentration (< 1000 ppm). The stress force involved in

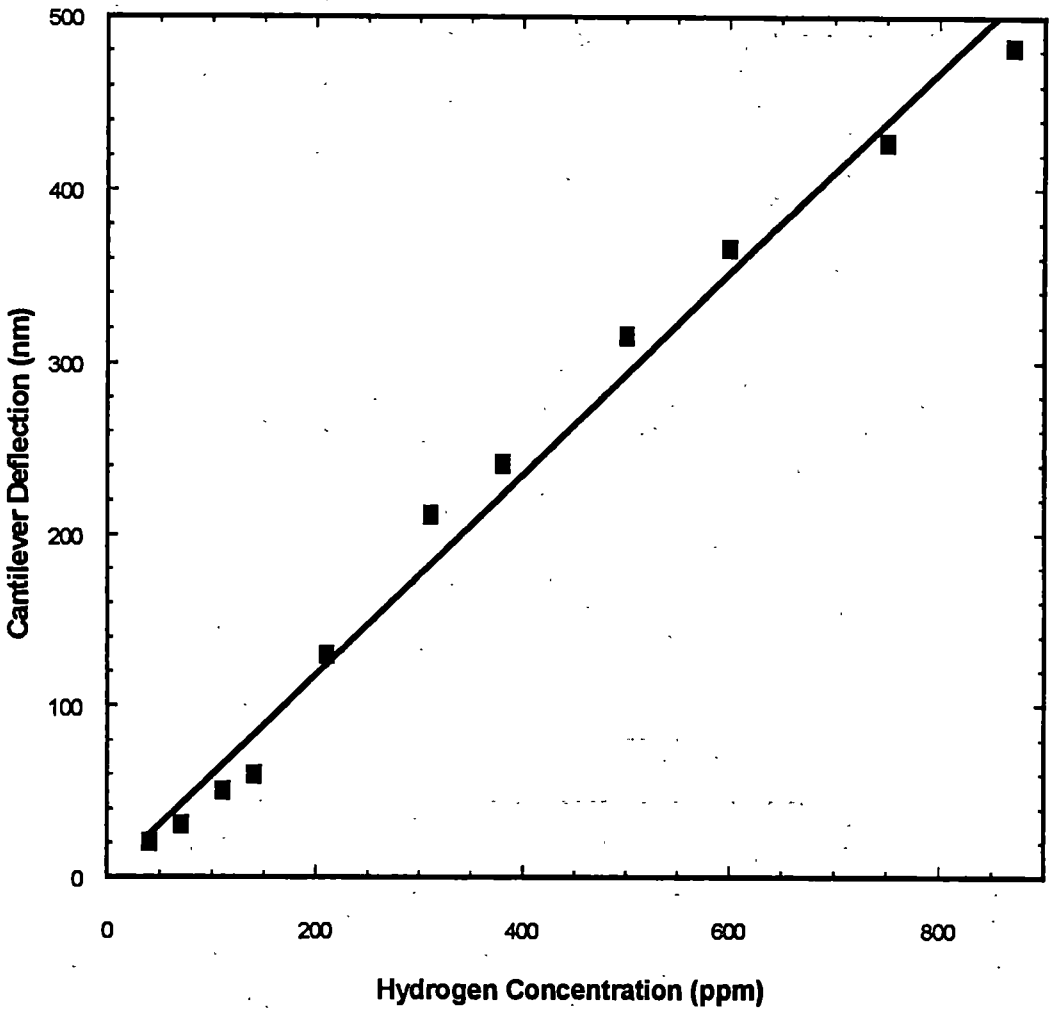


Figure 12: Cantilever deflection vs. low hydrogen concentration in the gas cell

this particular cantilever (Park Ultralever, D-type) was about 1.23 nN (= ~14.4 pN/μm length) per ppm hydrogen concentration. Therefore the microcantilever is a good testing stage for thin film stress studies.

As the hydrogen concentration increases cantilever deflection is no longer a linear function of the hydrogen concentration in the gas cell. As shown in Figure 4.13, the cantilever bending appears to be a power function of the gas cell concentration. The fitting curve in this plot follows the equation

$$V = aC_{GC}^{b}, \tag{4.8}$$

where $a \approx 7.47$ and $b \approx 0.818$. (The unit of cantilever bending voltage V is in mV and the gas cell hydrogen concentration C_{GC} is in ppm.) According to the results obtained from the literature,[173] for low concentration (<10,000 ppm or ~ 9 mmHg partial pressure) the hydrogen atom concentration within palladium is about $C = 1.17\ C_{GC}$. Substituting Eq. (4.8) in Eq. (2.10), the relative expansion coefficient for palladium becomes

$$\alpha_{Al} = \frac{\eta t_2^2 K}{3(t_1 + t_2)L^2} \frac{V}{1.17 C_{GC}} = \frac{\eta t_2^2 K}{3(t_1 + t_2)L^2} \frac{a}{1.17} C_{GC}^{b-1}. \tag{4.9}$$

For a silicon cantilever (85 μm long, 600 nm thick, 22 μm wide, and 8.5 nm Pd-coated), the relative adsorption-induced expansion coefficient α_{Al} was plotted as a function of hydrogen concentration C_{GC} in the gas cell in Figure 4.14 (note X-axis C_{GC} is logarithmic). It can be seen that due to the phase translation the expansion coefficient decreases when the hydrogen concentration increases. The expansion

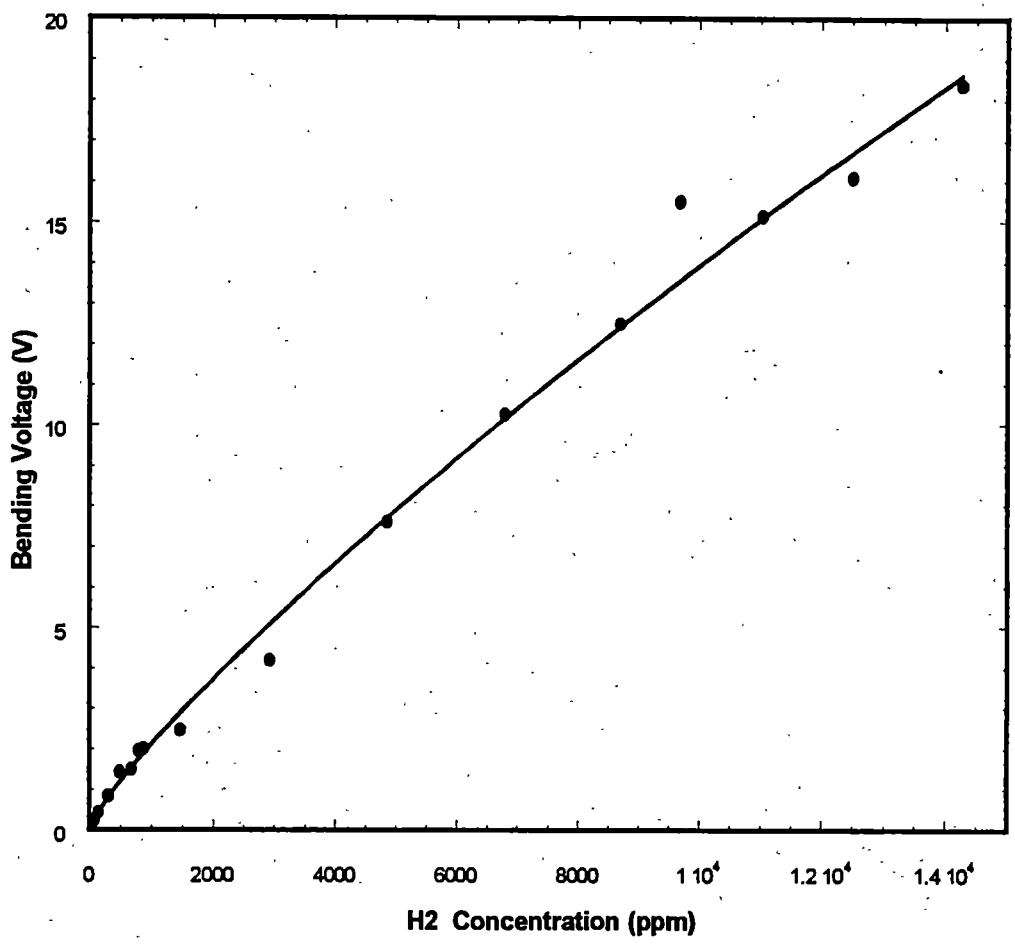


Figure 4.13: Cantilever responses to hydrogen concentration in the gas cell.

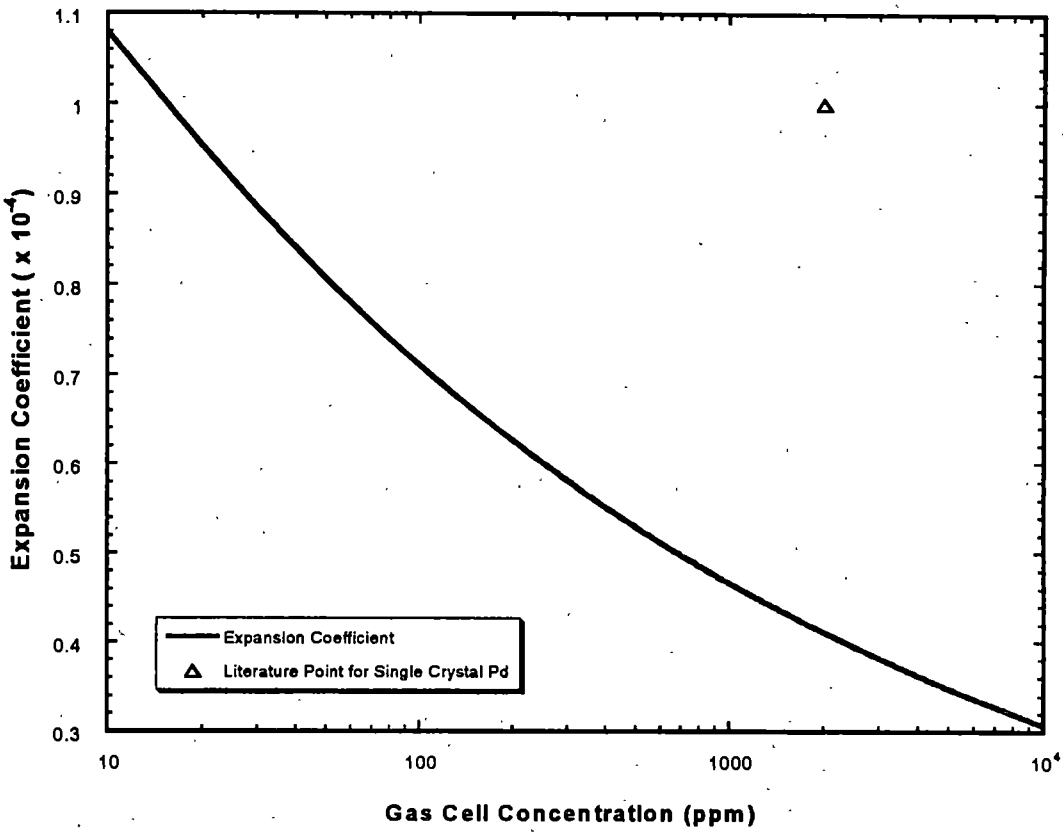


Figure 4.14: Relative adsorption-induced expansion coefficient vs. hydrogen concentration in the gas cell. For single crystal palladium, the reported linear adsorption expansion is $\Delta L/L = 1\times10^{-4}$ at a concentration of 2000 ppm.

coefficient in pure α-phase can be as much as one order higher than it is in β-phase. The published experimental results have shown similar changes. [171] But sputter coated palladium films are polycrystalline and have a sponge-like structure. [74] Up to 40% film volume was found empty (fill in with air) for the sputter-coated palladium films. The adsorption-induced expansion coefficients can be expected to vary with the film density and structure.

Adsorption-desorption processes can change the surface of the sputter-coated film until a relatively stable structure is formed (lower surface energy). In Figure 4.15, a newly sputter-coated palladium film was exposed to hydrogen for the first time. The increase of the cantilever bending implies that the film expanded when the hydrogen was introduced for the first time. The film first contracted for a short duration and then expanded. It should be noticed that the cantilever had an intrinsic bending due to coating-induced stress. This indicates that the film had a tighter or more contracted surface than before. The amount of stress change can be calculated by measure the difference of bending positions. Normally, after a several runs of high concentration hydrogen (1~2 %) the films have more uniformly and more predictable responses.

4.4.2 Hydrogen Diffusion Time Delay and Palladium Surface Model

Comparing theoretical calculations, the hydrogen adsorption (or desorption) time in our experiments is several orders-of-magnitude higher than the theoretical values. But the time in our calculation is the time for hydrogen atoms to diffuse

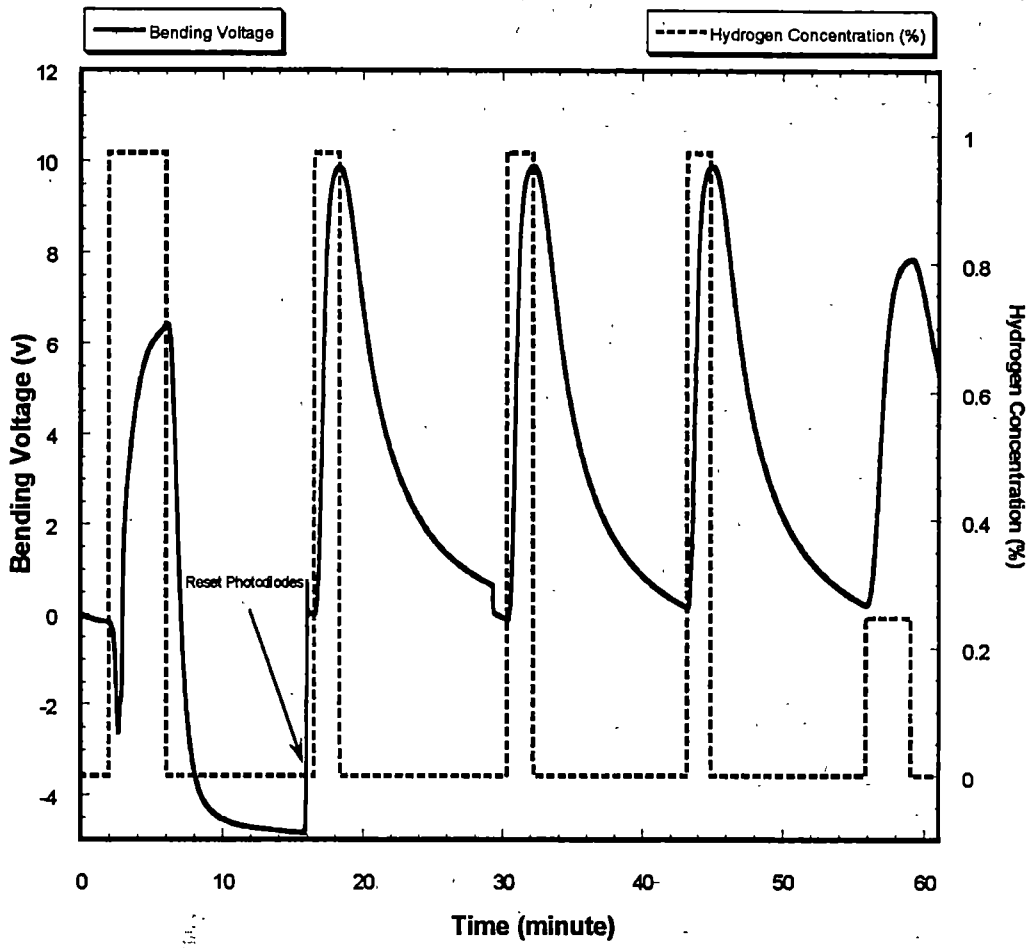


Figure 4.15: Sputter coated palladium film exposed to hydrogen at first time.

within the palladium bulk with no consideration of the surface conditions. The experimental results obtained in a UHV system confirmed that on clean metal surfaces the hydrogen adsorption (or desorption) time is in the same order of magnitude as the theoretical calculation that was presented earlier. [199] Some reported experiments, which have similar experimental conditions as ours, have shown the same adsorption time constants (in minutes). [65, 94, 95, 111-113, 185, 193, 194, 202]

Some models were used to explain the time delay of hydrogen adsorption on the "real" palladium surface.[194] The proposed models include surface contaminations, oxide layer, water layer formation, and hydrogen molecule dissociation at the palladium surface that may significantly slow down the adsorption process. Therefore, the total adsorption time t_{total} is equal to

$$t_{total} = t_{contam} + t_{water} + t_{PdO} + t_{Hatom} + t_{Pd}, \tag{4.10}$$

where t_{contam} is the time needed to pass though the surface contaminations layers, t_{waterl} is the time needed to form and pass the water layers, t_{PdOl} is the time needed to pass the oxidized palladium layer, t_{Hatoml} is the time needed to disassociate hydrogen molecules into hydrogen atoms at palladium surface, and t_{Pd} is the time needed for hydrogen atoms to diffuse through the bulk of palladium.

Then, it is necessary to single out in Eq.(4.10) which one of five terms plays the dominant role in the adsorption time delay. The last two terms ($t_{Hatom} + t_{Pd}$) in Eq. (4.10) should survive even if ideally clean surfaces are used. The adsorption and desorption time obtained from the UHV system is in the millisecond range; it should

include at least these two terms. [152, 153, 171, 199] Therefore, these two terms are not the problem at here.

Next step is to check if the surface contamination is the reason. It is true that is impossible to totally avoid the contaminations on any surface in the ambient. All possible ways have been taken to reduce the possible contaminations (including specimen handling, gas sources, and storage methods, etc.) It is not anticipated that the surface contamination is a mayor problem in the experiments. To confirm this anticipation, we compared the samples that were stored under various conditions. Some of them were kept in a covered plastic culture dish in the ambient; some of them were kept in a low vacuum chamber (vacuum was provided by the wall-mounted vacuum tubes in our laboratory); and some of them were kept in pure nitrogen that flowed at a constant rate. After being left the samples over night, no matter which of storage method was, used they all showed some aging effects when they were exposed to hydrogen gas again. No experimental results can help to identify which palladium-coated cantilever had better responses than any others based on the storage method used. As indirect evidence, one palladium-coated MUMPS chip was passed around as a demonstration unit and was exposed to various environments. After almost one year from its original prepared date, it could still respond to hydrogen. The response time is slow but it is still well within the same order-of-magnitude. Therefore, the delay caused by the contamination is not the major reason.

It has been known that at least one monolayer of water can be found on all surfaces unless it is kept in a baked ultra-high vacuum system. When hydrogen gas is mixed with oxygen gas, their atoms can form water molecules: [82, 94, 95, 193]

$$O_{2gas} + 2H_{atom} \Rightarrow 2OH_{atom}, \quad (4.12)$$

$$OH_{atom} + H_{atom} \Rightarrow H_2O_{gas}. \quad (4.13)$$

Under room pressure liquid water will become vapor when it is heated over 100 ^{0}C. Experiments have shown that the hydrogen adsorption and desorption time were improved when palladium film was heated over 150 ^{0}C or so. [65, 185, 193] But such improvement was less than one order of magnitude, the entire adsorption (or desorption) process was still in minutes. [193]

After ruling out four terms from Eq.(4.10), the only one left is the time delay caused by the palladium oxide layer on the outer surface. It is well known that almost all metals including some semiconductors (i.e. silicon) can be oxidized in the ambient. [82, 84, 155, 172, 203-207] Generally, an oxide layer has very different physical and chemical properties compared with its bulk material.

Because the oxide layer on the outer surface is very much like the sugar coatings on M&M chocolate candies. The following model is proposed for the palladium surface and it is called "sugar coating model". Plotted in Figure 16 is a cross-section of palladium surface. As shown in Figure 4.16(a), a thin layer of palladium oxide film is between palladium bulk and the ambient. Research has shown that most perfect or nearly perfect oxide surfaces are essentially inert to H_2 and hydrogen molecules cannot disassociate on the perfect oxide surfaces. [154] But hydrogen can adsorb at the defects of an oxide surface. [154] Those surface defects (or cracks) provide a entry and passageway for small-sized hydrogen molecules to reach the inner palladium bulk. Each defect or crack may be seen as a very thin pipe

or "bottleneck". These small cracks or defects limit the amount of hydrogen that can pass through and slow down the entire adsorption process. Therefore, it will takes much longer time to fill hydrogen atoms into the palladium bulk. Obviously, high hydrogen pressure can speed up the adsorption process as more hydrogen atoms pass the oxide layer.

Naturally, more such defects can speed up the total passing rate too and that is what will happen next. Once hydrogen molecules reach the actual palladium surface and disassociate into hydrogen atoms, they can quickly diffuse into the bulk of palladium film and cause the volume expansions. Uneven surface expansions between the oxide layer and palladium film will create more and bigger cracks (or defects) on the oxide surface. As a result, more hydrogen atoms will enter palladium bulk and cause more expansions until the hydrogen atom concentration inside the palladium reaches a balance with the external hydrogen pressure (Figure 4.16(b)). This process may appear as the slow start at the beginning of adsorption then reach to a steady but faster rate, which is similar to the cantilever bending or palladium film resistance change curves. It may also explain why hydrogen charging and discharging times decreased exponentially with the increasing of hydrogen concentration (pressure) shown in Figure 4.6.

Figure 4.16(c) shows that newly created defects or cracks are left on the oxide surface after hydrogen atoms desorbed from the palladium bulk. If hydrogen is reintroduced back into the system, a faster response time is expected because there are more entries on the oxide surface than before. This is exactly what was observed in

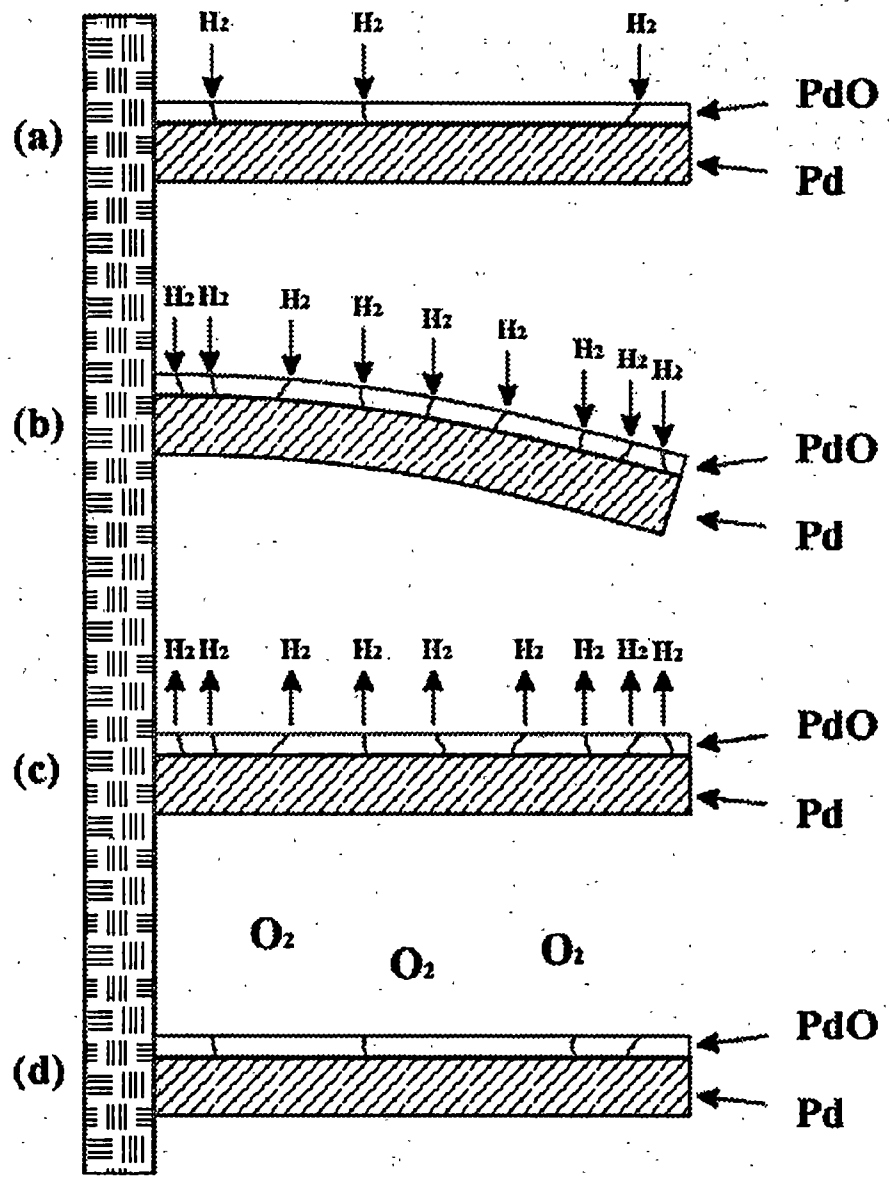


Figure 4.16: Schematic of hydrogen diffusion model on the oxidized palladium film surface. (a) Hydrogen diffuses through the oxidized palladium surface with a few cracks on it. (b) More cracks were created as a result of hydrogen adsorption-induced volume expansion. More hydrogen passed through the newly created cracks. (c) After hydrogen desorbed from the palladium, new cracks were left on the film surface. (d) Oxygen in the ambient oxidized the surface and healed some cracks.

the experiments. In order to obtain more uniform and more repeatable data, before each hydrogen experiment the palladium-coated cantilevers were first exposed to high hydrogen concentrations several times especially after they have left in the ambient for some time (more than one day). During the experiments, the cantilevers were always exposed to high concentrations than those we were going to perform on that day. For example, if we were going to measure hydrogen concentration at 1% or less for that day, 2% or higher concentrations were used at the beginning of the experiments. During each high concentration cycle (it was called "warm up period"), shown in Figure 4.17, the cantilever bending amplitude got bigger and bending became faster until they reached to a stable level. When palladium-coated cantilevers were left in the ambient for a period of time (say several days), the oxidization process oxided the newly exposed palladium surface resulting in fewer cracks left on the palladium surface. The cracking damage, which has created during the hydrogen adsorption-induced expansions, "heals" over time (Figure 4.16(d)). If expose to hydrogen again, the palladium-coated cantilevers will behave as what is seen in Figure 4.17. Comparing Figure 4.15 with Figure 4.17, they appear similar. But if take a closer look, it can be seen that the freshly prepared surface in Figure 4.15 does not have the gradually increasing of bending amplitude periods (cycle 2 to 4). It may imply that the freshly prepared surface had a thinner oxide layer than the aged surface. The period of the gradually increasing cantilever bending amplitudes is the period of the crack formation on the oxide surface in this model.

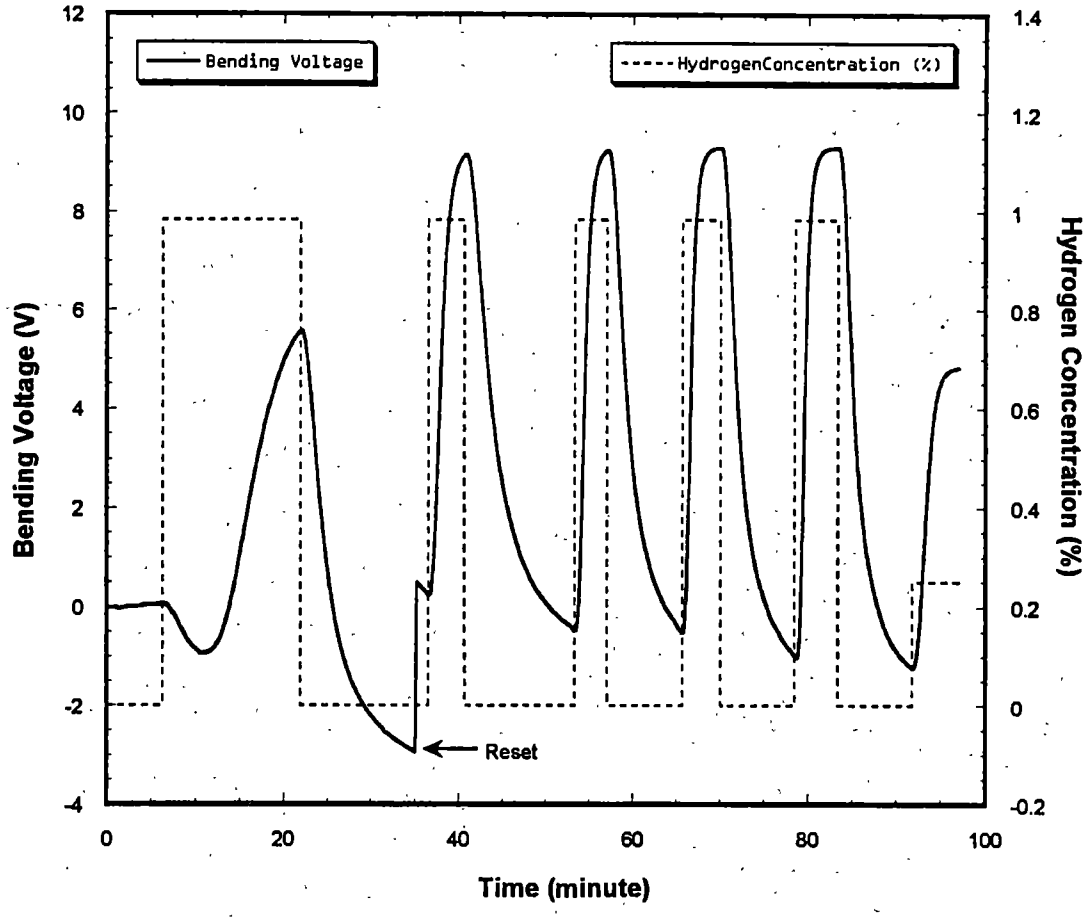


Figure 4.17: Palladium surface reactivation.

Cracked surface model may be also used to explain why the desorption rate is slower than the adsorption rate. During the adsorption hydrogen molecules can be found anywhere outside the oxide, therefore hydrogen molecules can not only directly adsorb on the defects, but also more and bigger entries appear during the adsorption. But during the desorption process, things work in the opposite ways. Not only all hydrogen atoms have a direct exit out from the palladium bulk, and those exits (defects) are getting smaller during the desorption process. Longer time for desorption is expected.

Limited by the current equipment and technical skills, the small cracks on the palladium coating surface on the cantilevers cannot be directly observed. Those cracks have to be very small (<< 1 μm) because they cannot be seen under a light microscope (~ 500 X) system. Though the model can well explain almost all observations and problems in this dissertation, there is no direct evidence to prove it. In the literature a perfect oxide layer was report inert to hydrogen and hydrogen could only adsorb at the defects on the oxide surface. [154] But it has been known that hydrogen can crack or blister the palladium thin film and occasionally peel off the substrate. [115, 124, 149, 150, 154, 155, 174] Micrometer-sized blisters and cracks were observed when palladium thin film was exposed to 10% hydrogen/nitrogen mixtures. [100] It is not very hard to image that the low concentration hydrogen can do similar damage in a much smaller scale. Some literature has reported problems like surface aging effects, but few of them have made detailed discussions and most of them just considered this problem caused by surface contaminations. [92, 94, 95, 100-102, 108, 111-113, 115, 149, 181, 193, 208-211] Sizes of the cracks are expected to

be in the range of from one nanometer to a few tens of nanometers depending on hydrogen concentration. How to catch those cracks in action is still a technical challenge, and it was beyond the efforts that the author can afford during the writing of this thesis.

4.4.3 Hydrogen Detection and Microcantilever Sensors

Hydrogen gas is well known as a dangerous explosive gas when it mixes with certain concentrations of oxygen. It can also cause structural damage in many materials including metals and semiconductors. [115, 122-124, 149-151, 154, 155, 173, 174, 191, 212] There are a large number of commercial instruments that have been developed for measuring hydrogen concentrations including electrochemical cells, thermal conductivity sensors, gas chromatographs, mass spectrometers, combustible gas sensors, fiber optical sensors, and metal-oxide semiconductor resistance sensors. [90-95, 98-102, 105, 106, 111-113, 194, 202, 213-217] In spite of the commercial instruments available as indicated above, the measurement of H_2 continues to be a challenging technological problem. Small, lightweight, low-power, low-cost, fast-response, remotely fieldable devices are still in great demand. Applications would range from point detection of leaks in liquid-H_2-fueled rocket motors, semiconductor-fabrication clean rooms to future hydrogen (or battery) powered automobiles.

Stress-sensitive palladium (or its alloys) may be used as a sensor platform. For a 30-nm Pd coating on a 0.7-μm silicon base Ultralever (D-type), the sensitivity was

determined to be 9.13 mV/ppm or ~0.9 nm/ppm. The noise level for current configuration is about 1 mV, which corresponds to a detection limit of about 100 parts-per-billion (ppb). Current optical detection methods have very high sensitive (<0.01 nm equivalent to 1 ppb detection), but the complex optical and electrical systems make it not a promising candidate. Modified MUMPS microcantilever arrays seem more realistic. However, many technical difficulties have to be solved before a real device can be made. Those problems include keeping film surface clean, preventing aging effects, packaging, sampling and data readout etc. But the high sensitivity, miniaturization, low power, and ability of manufacture in high volume give technology a bright future.

Chapter 5

ANALYSIS OF GOLD-MERCURY SYSTEM

5.1 Introduction

The investigation of hydrogen adsorption in palladium films provided a good understanding of bulk-like adsorption system. In this chapter another adsorption mechanism – surface-like adsorption will be discussed. With the goal of investigating surface adsorption, mercury on gold as a model was selected for the investigations. Experimental results of the surface adsorption-induced stress change and the thin film resistance variation will be presented. First, some background information about gold and mercury will be introduced. Then, surface stress variation causes the microcantilever bending will be discussed. Based on our experimental results a surface adsorption model will be proposed. The last part of this chapter contains a short discussion of surface energy and surface stress and how the microcantilever can be used as a sensor platform by exploiting the adsorption-induced variation of surface energy and stress.

5.1.1 Gold and Mercury

Both gold (At. No. 79) and mercury (At. No. 80) are heavy metals. Their atomic radii and atomic weights are very close (Their properties are detailed in

Appendix E). The discovery and usage of gold can be traced back to the very early stages of human civilization. Gold is found in nature as a free metal and in tellurides. It is very widely distributed and is almost always associated with quartz or pyrite. [169, 218] In addition to its usage for jewelry and coins, gold is a good conductor of heat and electricity, and it is unaffected by air and most reagents. Thin-film gold is a very good reflector of infrared and visible light and is widely applied in optical systems and satellites.

Mercury is the only metal that is liquid at ordinary temperatures as it has a melting temperature of $-38.87\ ^{0}C$. In Chinese, mercury is called "liquid-like silver" or "water silver" and has been known to ancient Chinese and Hindus for thousands of years. It occurs free in nature, but the chief source is cinnabar (HgS) that was widely used in the ancient world as a pigment (vermilion). [169, 218]

Compared with other metals, mercury has rather poor heat conductivity and fair electrical conductivity. It is widely used in thermometers, barometers, diffusion pumps, mercury-vapor lamp, switches, and many other instruments. Because of its high volatility, mercury and its compounds enter the atmosphere through emission in the form of vapors and particulates from industries (such as coal-fired power plants, laboratories and hospitals) and also by evaporation from soil and water. Once in the atmosphere, mercury atoms can easily move with the winds and reenter the ground and water sources. Evaporation from ground and water can eventually reintroduce mercury atoms back into the atmosphere and complete the cycle. [219]

Even though mercury exists naturally in our environment excessive amounts of mercury concentration in air and water can be toxic. [219, 220] At high concentration mercury and its compounds are very harmful to humans and animals and can cause various illnesses even death. [170, 219] Thus, today as society becomes more and more industrialized, concerns of environmental protection have drawn more attention than ever from government, industry and the general public. There exists a widespread need for highly sensitive contamination detection methods and systems that includes the detection of mercury vapor. However, at present not only are the prices for existing mercury vapor sensors expensive, but these systems also suffer from the poor sensitivity and response time. Therefore, new methods of sensing are needed for the development of inexpensive and extremely sensitive mercury sensors.

5.1.2 Mercury Adsorption on Gold Surface

It has been known for a long time that metal surfaces such as gold and silver have a strong adsorption affinity for mercury. [70, 97, 103, 110, 221] As compared to the palladium-hydrogen system, more limited research has been done for mercury-vapor adsorption on gold surface. Moreover the mechanism of mercury on gold is not thoroughly studied. [69, 96, 104, 222-227] It is known that mercury atoms adsorb on gold surfaces when gold substrates are exposed to gaseous mercury. [38, 49, 78, 96, 97, 103, 104, 110, 222, 225, 228-232]

Close surface observations performed by AFM and STM found that some island-like structures are formed on gold surfaces subsequent to mercury exposure.

[104, 222-225, 233, 234] Depth profile analyses showed that most mercury atoms are adsorbed on the surface and that mercury atoms can only diffuse into the gold substrate for a few nanometers at room temperature. [222] Other techniques have been employed to analyze the property variations of thin gold films as a result of mercury adsorption. The reported property changes include reflectivity, resistivity and frequency shift of piezoelectric resonators. [78, 104, 110, 226, 229, 230, 235] However, no research attempts have been reported about the mercury adsorption-induced stress changes on the gold surface. The only related article that the author could locate was the early work done in our group. [38] Therefore there exist many unanswered questions about mercury adsorption on gold surfaces because of lack of research in this area. To address this problem, the ultra-high stress sensitivity of microcantilevers have been utilized to investigate the stress changes induced by mercury adsorption on thin gold film.

5.2 Surface Stress and Cantilever Deflection

Before presenting any experimental results, it is necessary to present the relationship between surface stress and cantilever deflection. Cantilever deflection caused by surface stress differences between the two surfaces of a cantilever will be discussed.

The adsorption-induced stress on two identical surfaces are expected to be equal. For example, if we have a cantilever that is made of gold, it should not bend, since mercury adsorption-induced stresses are equal on both surfaces. In the actual

experiments, it is possible to observe a small bending caused by the small asymmetric nature of two surfaces and tiny variations of material properties on both surfaces. The easiest way to enlarge the stress differences of two surfaces is by making one surface different from the other surface.

Research using dissimilar surfaces of cantilever structures to study stress have been reported from the early 1900s through recent works. [27, 29-41, 49, 55, 92, 120, 236-238] If the surface tension of one side decreases, then the cantilever bends away from that side with bending radius R as shown in Figure 5.1. For a cantilever with a thin film coating ($t_2 >> t_1$), the radius of curvature, R, is given by [26, 236]

$$\frac{1}{R} = 6\frac{(1-\nu)}{Et_2^2}(\Delta\sigma_1 - \Delta\sigma_2), \tag{5.1}$$

where E is the Young's modulus of the substrate, ν is the Poisson ratio, and t_2 is the thickness of the cantilever. $\Delta\sigma_1$ and $\Delta\sigma_2$ are the surface stress changes on the surface of coating film and substrate surface, respectively.

To simplify our problem, the bending of a cantilever can be treated as a simple one-dimensional spring. The well-known Hooke's law expresses the relationship of a simple spring as the following: the restoring force F of the spring caused by the elastic deformation Z of the spring is

$$F = kZ, \tag{5.2}$$

where k is called spring constant and is a parameter is determined by the physical property of the spring such as material, size and formation, etc.

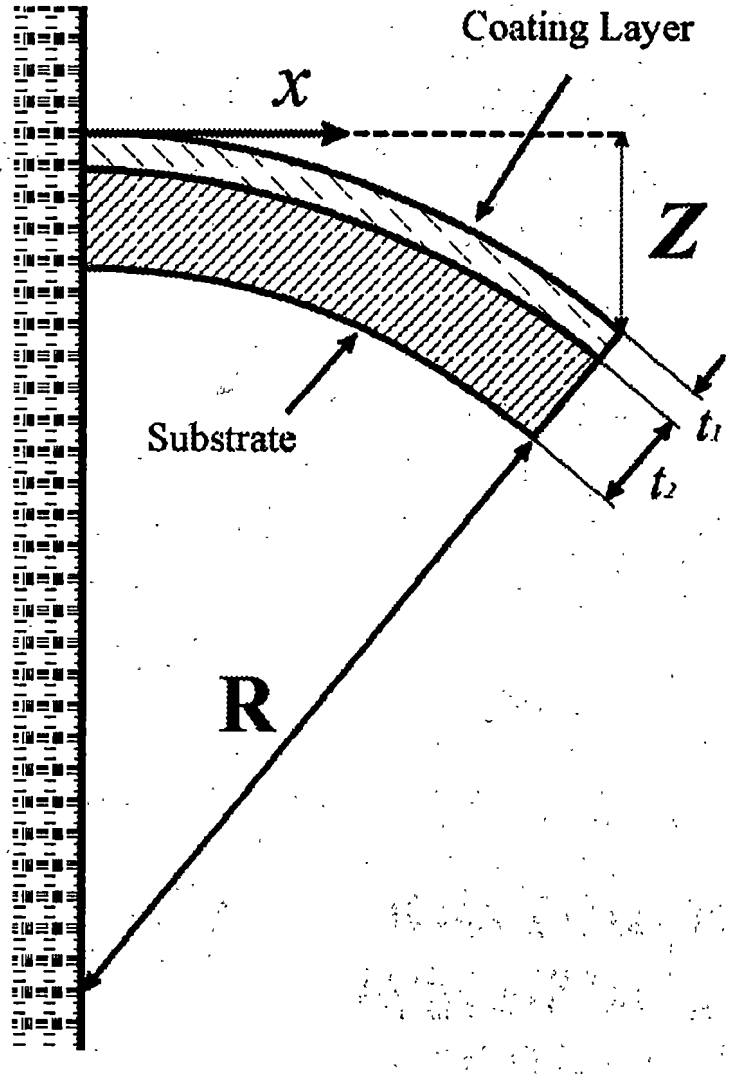


Figure 5.1: A schematic of bending cantilever with the radius of curvature *R*.

In the case of the surface adsorption-induced cantilever bending, if the free-end deflection Z of the cantilever can be measured, then the accumulated stress force F along the cantilever can be determined. When the optical detection method is used, substituting Eq.(3.1) into Eq.(5.2) the restoring force F_r induced by the cantilever deflection $Z = \delta$ is

$$F_r = k\delta = k\eta\Delta V, \tag{5.3}$$

where η is the deflection sensitivity and ΔV is the readout voltage from output device. If we use $F_{atom}^{(n)}$ to represent the surface stress force (surface tension) induced by each atomic adsorption, then the restoring force F_r of the bent cantilever is equal to the accumulation of the surface stress force F_s induced by each atomic adsorption and it is given as

$$F_r = F_s = \sum_{n=1}^{N_{adsorbed}} F_{atom}^{(n)} = N_{adsrobed} F_{atom}^{(n)}, \tag{5.4}$$

where $N_{adsorbed}$ is the total number of adsorbed adsorbate atom. Therefore, if we know the total number of the atoms adsorbed that are on the cantilever surface, the surface stress force (surface tension) induces by each atomic adsorption is

$$F_{atom}^{(n)} = \frac{F_r}{N_{adsorbed}} = \frac{k\eta}{N_{adsorbed}}\Delta V. \tag{5.5}$$

In Eq.(5.5), the spring constant k, deflection sensitivity η and the output voltage ΔV can be measured. Then the only undetermined parameter is the total adsorbed atom number $N_{adsorbed}$ of adsorbate.

It is impossible to count directly and accurately how many (adsorbate) atoms adsorb on the surface of adsorbent. However, the number of adsorbate atoms arriving the surface in a unit time should proportional to the vapor partial pressure (concentration). Therefore, the total number of the adsorbate atoms N_{arrive} that arrive the adsorbent surface in time Δt can be calculated as

$$N_{arrive} = BC_A \Delta t, \tag{5.6}$$

where C_A is the volume concentration of mercury vapor, B is an experimental configuration parameter. N_{arrive} obtained from Eq.(5.6) is not the total adsorbed atom number N adsorbed at the adsorbent surface yet. To find out how many atoms can adsorb at the adsorbent surface, we need to establish a model for the surface adsorption mechanism this will be describe in the following section.

5.3 Surface Adsorption Model

As mentioned in the earlier part of this chapter, it has been reported in the literature that mercury atoms stay only on the top layer or near the surface of the gold film surface at room temperature. [96, 222, 225, 230]. At higher temperature, adsorbed mercury atoms can diffuse into the deeper layers of gold film up to several nanometers from the surface. [222] Various experimental methods including ours have confirmed that the adsorption of mercury atoms at the gold surface is a continuous process until one monolayer of coverage is reached. Also the adsorption rate decreases along with the increase of monolayer coverage. [38, 49, 104, 110, 222, 226, 230, 231, 235]

Langmuir [239-243] proposed a model for the gas adsorption process in the 1910s. His idea was that when an incoming atom (or molecule) collided with a surface it could be "trapped" in a weakly bound state. The atom (or molecule) would then have to find a bare site before it could "stick"; if not, the molecule would desorb. Langmuir modeled his adsorption data by assuming that trapping probabilities were unity. Considering the particular mercury/gold system is used here, the Langmuir's model has been modified by adding the following two main assumptions (more details about these assumptions may be found in Appendix F). The illustration of this model is shown in Figure 5.2 in which mercury is the adsorbate (in vapor) and gold is the adsorbent (substrate).

1. If there is an acceptable site available on the adsorbent surface, an incoming adsorbate atom will adsorb on that site with no further movement and interaction between the adsorbed atom and the adsorbent surface.
2. An adsorbed atom will not desorb from the surface unless the adsorption conditions changed.

Conventionally, a sticking coefficient $S(\theta)$ is used to describe the probability of an incident molecule (or atom) adsorbing on the surface. The sticking coefficient is defined as [82, 244]

$$S(\theta) = \frac{N_{stick}}{N_{arrive}}, \tag{5.7}$$

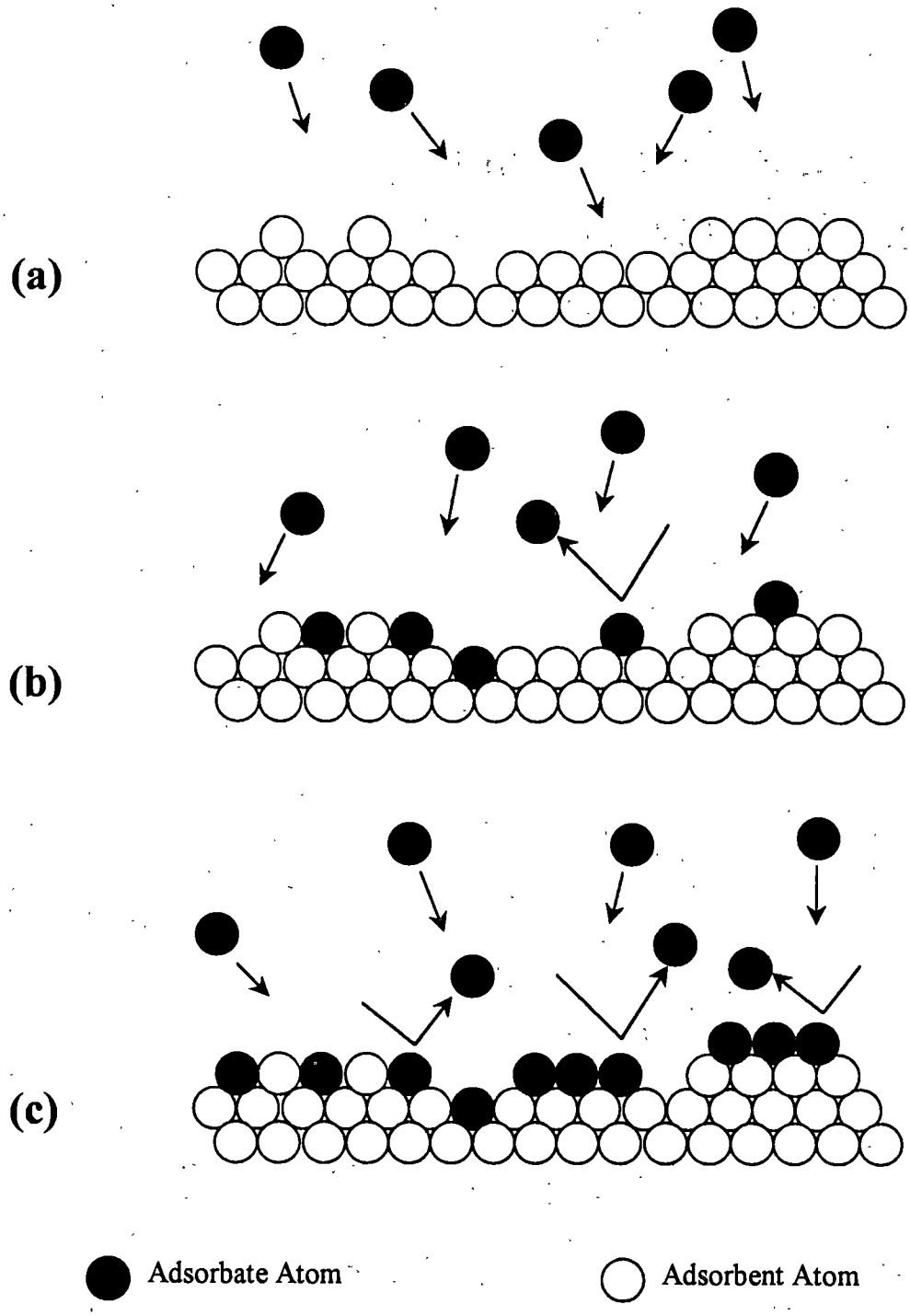


Figure 5.2: A model of the surface adsorption process. (a) Fresh adsorbent surface, all adsorbate atoms are accepted by the surface; (b) Adsorbent surface partially covered by the adsorbate atoms, some arriving adsorbate atoms are rejected; (c) When all most all the adsorbent surface coved by the adsorbate atoms, no more adsorbate atoms are accepted.

where N_{stick} is the number of molecules (atoms) that stick on the adsorbent surface, and N_{arrive} is the number of molecules (atoms) that impinge on the adsorbent surface. However, the values of both N_{stick} and N_{arrive} cannot be measured in the experiments, and they also depend upon the mercury vapor concentrations, flow rate and other conditions. Therefore, it is very difficult to even estimate a reasonable value for $S(\theta)$ based upon these uncertainties.

The adsorbent surface area generally can be measured rather precisely. A reasonable estimate of the total adsorption sites on the adsorbent surface can be made based upon the adsorbent atom size and atom arrangement on the surface. Here, a new parameter J is introduced as the adsorbent surface rejection factor (formal definition of J will be introduced later) that describes a ratio by which the adsorbate atoms are prevented from adsorbing on the surface. Therefore, unlike sticking coefficient $S(\theta)$ the rejection factor J is a function of surface coverage. For example, if $J = 0.1$ it means that 10% adsorbate atoms will be rejected from the adsorbent surface while 90% of the adsorbate atoms successfully adsorb on the adsorbent surface. For freshly prepared adsorbent surface, J has its minimum value of zero (100% adsorption). If one monolayer has already formed then J has a value of one (100% rejection). Therefore, equation for $N_{adsorbed}$ and N_{arrive} is given as

$$N_{adsorbed} = (1-J)N_{arrive}. \tag{5.8}$$

Substituting Eq.(5.6) & (5.8) into Eq.(5.5), we have

$$F_{atom}^{(n)} = \frac{k\eta}{(1-J)N_{arrive}}\Delta V = \frac{k\eta}{(1-J)B}\frac{\Delta V}{C_A \Delta t} \tag{5.9}$$

If the adsorbent surface is exposed briefly to the vapor, for a very low surface coverage we can consider the value of $J \sim 0$ for a period of time. Then Eq.(5.9) may be rewritten as

$$F_{atom}^{(n)} = Q\frac{\Delta V}{C_A \Delta t}, \qquad \text{where } Q = \frac{k\eta}{B}. \tag{5.10}$$

Since Q is an experimental parameter and all terms in Q should not change during the experiment, then Q can be treated as a constant. Based on the assumption $F_{Atom}^{(n)}$ should be a constant. The value of $F_{Atom}^{(n)}$ should not depend upon the adsorption rate, adsorbate (vapor) concentration and the adsorbent surface coverage. Therefore, two adsorbate (vapor) concentrations C_{A1} and C_{A2} should have a relation as

$$\frac{\psi_1}{C_{A1}} = \frac{\psi_2}{C_{A2}}, \tag{5.11}$$

where $\psi = \frac{\Delta V}{\Delta t}$ is the rate of cantilever bending which can be measured from the experiments for each concentration. If experimental results can confirm that Eq.(5.11) is valid, then the proposed surface adsorption model is a suitable one. More discussion of our model will be introduced experimental section that follows.

The next step is to determine the value of J when the adsorbate concentration is considerably higher and a larger portion of the adsorbable sites is already occupied. As more and more adsorbate atoms are rejected by the adsorbent surface, the effects caused by J are no longer negligible.

Recall the two assumptions of our surface adsorption model: (a) only one gold atom can associate with one mercury atom; and (b) one (adsorbent) position (site) can only be occupied by one adsorbate atom. First we need to find out the total number of acceptable (available) sites on the adsorbent surface. Assume the cantilever is L long and W wide and surface area of gold-coated cantilever is equal to LW. The atomic radii of the adsorbent (i.e. gold) atom and the adsorbate (i.e. mercury) atom are labeled as r_g and r_m respectively. For a square, uniform array, the total acceptable (available) positions on the adsorbent surface is equal to

$$N_{total} = \frac{LW}{(2r_g)^2} = \frac{LW}{4r_g^2}. \tag{5.12}$$

According to the assumptions, the adsorbent surface rejection factor $J(t)$ actually is the possibility that an adsorbate atom arrives at a preoccupied acceptable position. $J(t)$ is equal to the ratio of the occupied sites $N_{occupied}$ at that time divided by the total acceptable positions N_{Stotal} on the adsorbent surface as

$$J(t) = \frac{N_{occupied}}{N_{Stotal}}. \tag{5.13}$$

Initially, N_{Stotal} is much larger than N_{arrive}. Therefore, statistically $J(t)$ can more reliable reflect the actual adsorption process than the sticking coefficient $S(\theta)$. The occupied positions $N_{occupied}$ is equal to the sum of adsorbed atoms $N_{occupied}^{(i)}$ ($i = 1$, 2...m) and is expressed as

$$N_{occupied} = \sum_{i=1}^{m} N_{occupied}^{(i)}. \tag{5.14}$$

Considering the history of the adsorption on the adsorbent surface, Eq.(5.13) and Eq.(5.8) may be rewritten as

$$J(t)^{(m)} = \frac{1}{N_{Stotal}} \sum_{i=1}^{m} N_{occupied}^{(i)}, \tag{5.15}$$

$$N_{adsorbed}^{(m)} = [1 - J(t)^{(m-1)}] N_{arrive}^{(m)} = [1 - \frac{1}{N_{Stotal}} \sum_{i=1}^{m-1} N^{(i)}] N_{arrive}^{(m)}, \tag{5.16}$$

where m in the superscripts denotes the number of atom adsorbed per unit time. $N_{arrive}^{(m)}$ is the number of the adsorbate atoms that arrive at the adsorbent surface during the mth unit time. Obviously for a fresh surface (first time adsorption), when $m = 1$ then $J(t)^{(0)} = 0$ and $N^{(1)} = N_{arrive}^{(1)}$.

If there is a non-steady flow with variable (vapor) concentrations, the number of the arriving adsorbate atoms $N_{arrive}^{(m)}$ is different and its value depends on the flow rate and (vapor) concentration. If there is a steady flow and constant (vapor) concentration, the number of the arriving adsorbate atom $N_{arrive}^{(m)}$ is a constant, $N_{arrive}^{(m)} = N_0$, during each unit time t_0. Then Eq.(5.13) can be evaluated further as (the detailed evaluation may be found in the Appendix F)

$$J(t)^{(m)} = [m - \frac{\sum_{i=1}^{m-1} (m-i) N_{occupied}^{(i)}}{N_{Stotal}}] \frac{N_0}{N_{Stotal}}. \tag{5.17}$$

Using an integration to replace the sum in Eq.(5.17) for unit time $t_0 = 1$ the surface rejection coefficient over the total exposure time T_{total} is equal to

$$J(T_{total}) = \left[\int_0^{T_{total}} dt - \frac{1}{N_{Stotal}} \int_0^{T_{total}} N_{occupied} dt \right] \frac{N_0}{N_{Stotal}} = \left[1 - \frac{N_{occupied}}{N_{Stotal}} \right] \frac{N_0}{N_{Stotal}} T_{total} . \quad (5.18)$$

Substituting Eq.(5.13) into Eq.(5.17), and rearranging the equation as

$$J(T_{total}) = \frac{AT_{total}}{1 + AT_{total}}, \qquad \text{where } A = \frac{N_0}{N_{Stotal}} . \quad (5.19)$$

Since A is a constant for a given concentration and flow rate, at the beginning $T_{total} = 0$ then $J(T_{total}) = 0$. After a gold surface is exposed to mercury vapor for a long time ($AT_{total} >> 1$), then $J(T_{total}) \approx 1$.

Figure 5.3 shows how adsorbate atoms accumulate on the adsorbent surface under a constant flow rate and vapor concentration. There are two curves in Figure 5.3: the single accumulation during each unit time t_0 (dashed-line) and total accumulation (solid line). It can be seen that as the accumulation time proceeds, more and more adsorbent surface is covered by the adsorbate atoms. In the meantime, because fewer and fewer acceptable surface sites are available, less and less adsorbate atoms adsorb on the adsorbent surface within each unit of time t_0 even though the adsorbate atoms arrive the surface at a constant rate. For Figure 5.3, $A = 0.1$ per unit time t_0 is assumed. The smaller value of A means that the fewer adsorbate atoms arrive per unit time, the longer the time is needed to form one monolayer. Notice that when the monolayer coverage is less than about one-third to entire surface area, the accumulation is close to linear. In the next section we will see if this surface adsorption model fits the experimental results.

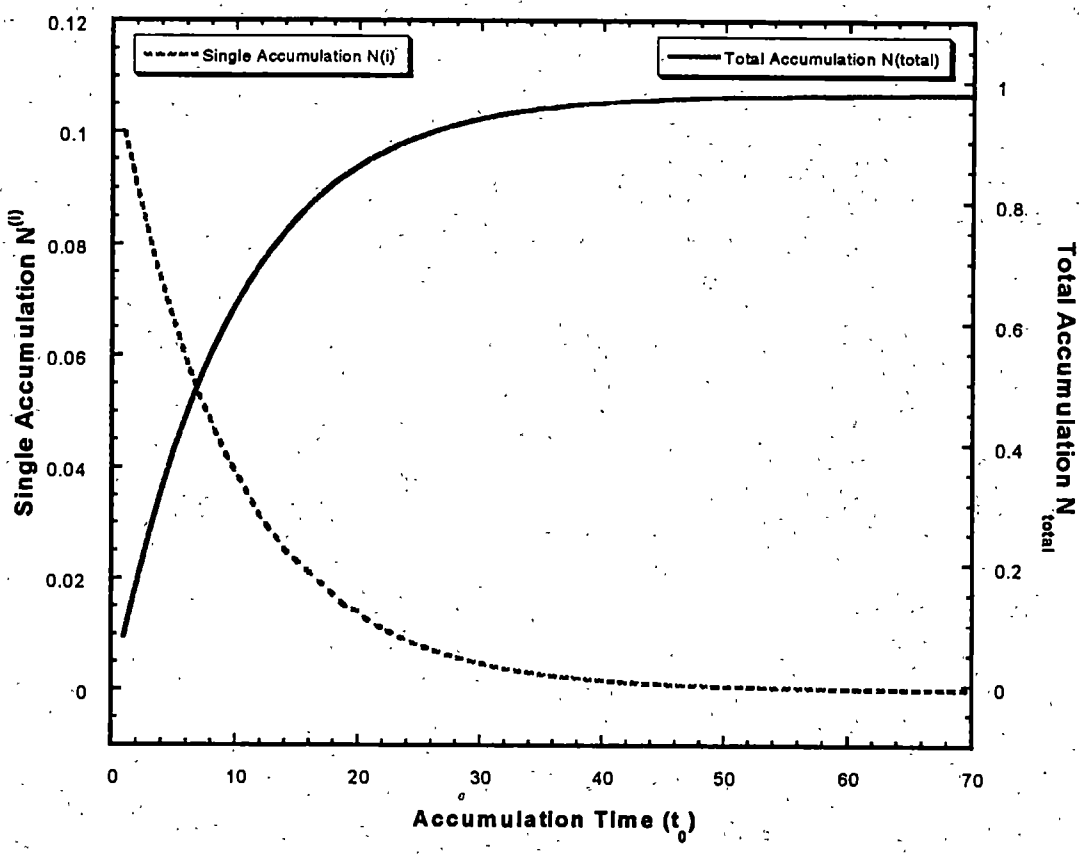


Figure 5.3: Theoretical model of the adsorbate atoms accumulate on the adsorbent surface under a constant flow rate ($A = 0.1$ per unit time t_0).

5.4 Mercury Adsorption-Induced Stress in Gold Film

5.4.1 Mercury Adsorption Induced Cantilever Bending

As in the case of the palladium/hydrogen system, similar bending and coating film resistance changes were observed on the gold-coated microcantilevers with mercury vapor adsorption. Figure 5.4 is a typical cantilever bending response to various mercury vapor concentrations. The data show that the curvature is away from the gold surface. The higher the concentration is, the faster the cantilever bends. Unlike hydrogen adsorption, there is no maximum bending position for given mercury vapor concentration unless the entire gold surface is covered by mercury atoms. Once the flow of mercury vapor is stopped (nitrogen gas flows continuously at same flow rate), the cantilever bending is stopped too.

5.4.2 Cantilever Bending Rate and Adsorption-Induced Stress

According to our surface adsorption model, the adsorption-induced stress change per adsorbed mercury atom is a constant and it is independent of mercury vapor concentration. Shown in Figure 5.5 is the result from an experiment where a freshly gold-coated cantilever was exposed to low levels of mercury concentrations (in ppt level). The first observation is that the higher the same vapor concentration, the faster the cantilever bent. The second observation is that for same vapor concentration the cantilever bending rate (or slope) is constant. In this experiment, two 610 ppt level mercury vapor concentrations were introduced into the gas cell separated by a few minutes of pure nitrogen. It still can be seen that the cantilever bent at the same

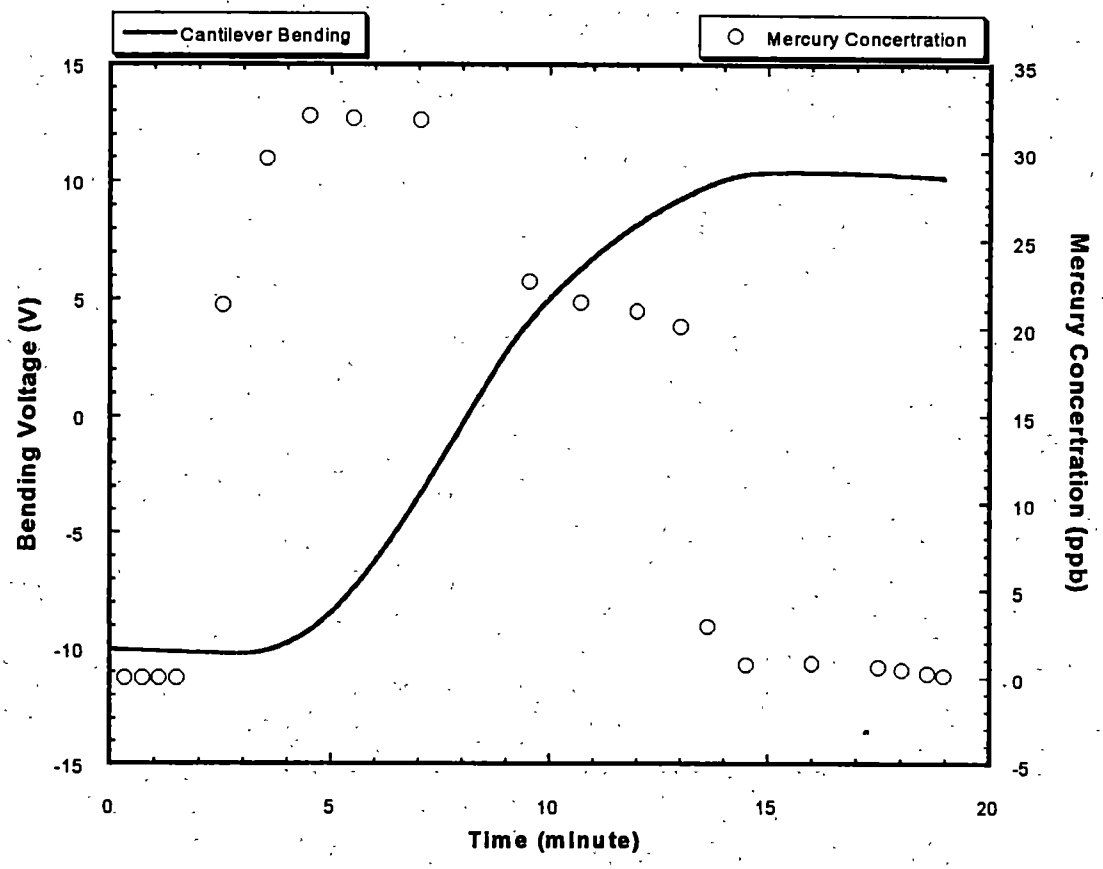


Figure 5.4: Typical gold-coated cantilever bending responses to mercury vapor. Mercury concentration was monitored by a commercial mercury detector at the points indicated.

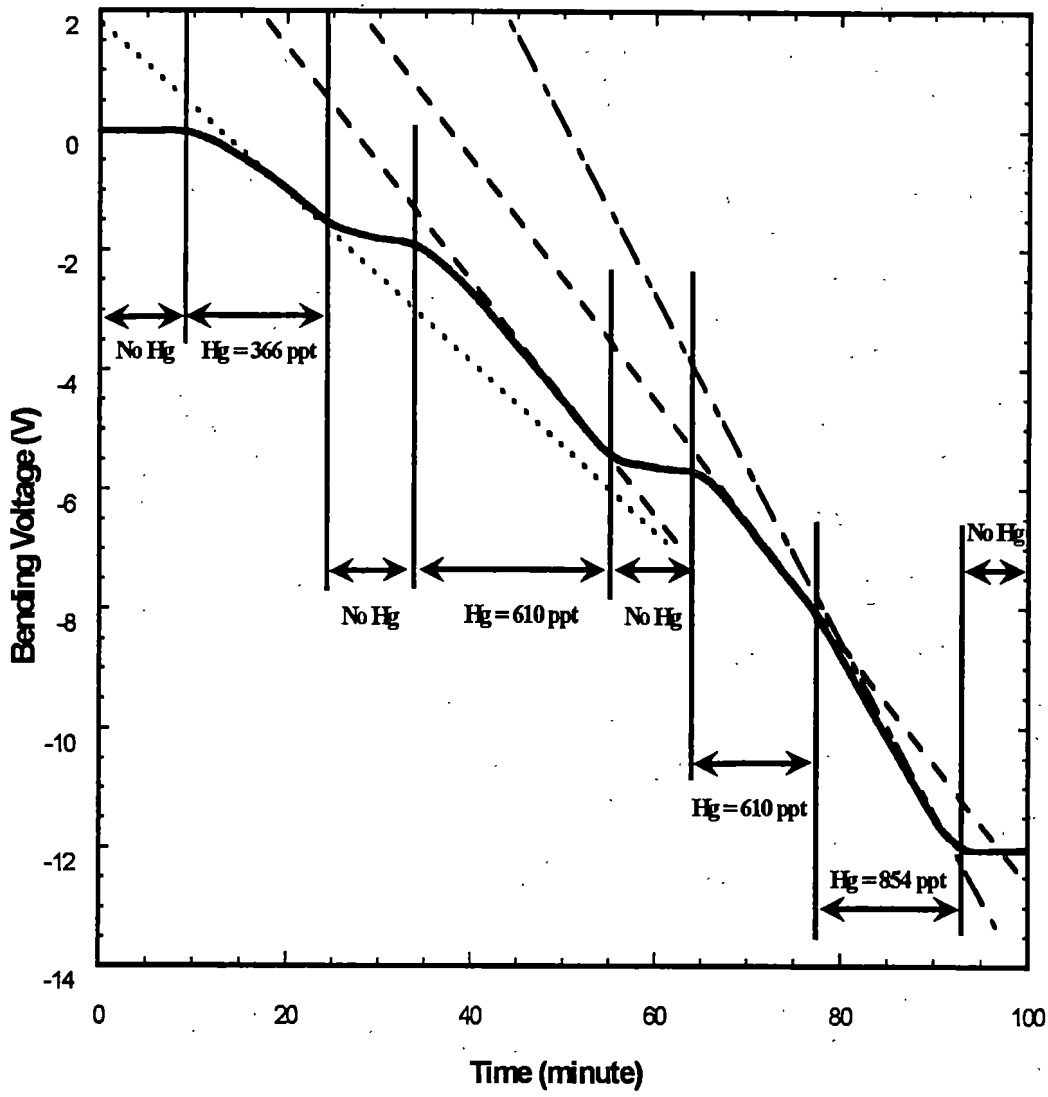


Figure 5.5: Gold-coated microcantilever is exposed to various mercury vapors.

rate during these two periods at where mercury vapors were introduced. To see these more clearly, two dashed lines are extended from these two periods of mercury vapor concentrations. The two extended lines parallel to each other. The third observation is that the gold-coated cantilever stays at same position when no mercury vapor presented.

One of the goals in this thesis was to verify if Eq.(5.11) is obeyed in our experiments. To do so, in Figure 5.5 the cantilever bending rates $\psi_1 = 0.1195$ V/minute; $\psi_2 = 0.1810$ V/minute; $\psi_3 = 0.1964$ V/minute and $\psi_4 = 0.2724$ V/minute are measured and calculated for four mercury concentration regions of 366 ppt, 610 ppt, 610 ppt and 854 ppt, respectively. Then we divided the bending rates by their corresponding mercury vapor concentrations as follows:

When Hg = 366 ppt; $$\frac{\psi_1}{C_{A1}} = \frac{0.1195}{366} \approx 3.27 \times 10^{-4}; \quad \text{(V/minute/ppt)} \quad (5.20)$$

When Hg = 610 ppt; $$\frac{\psi_2}{C_{A2}} = \frac{0.1910}{610} \approx 3.13 \times 10^{-4}. \quad \text{(V/minute/ppt)} \quad (5.21)$$

When Hg = 610 ppt; $$\frac{\psi_3}{C_{A3}} = \frac{0.1964}{610} \approx 3.22 \times 10^{-4}; \quad \text{(V/minute/ppt)} \quad (5.22)$$

When Hg = 854 ppt; $$\frac{\psi_4}{C_{A4}} = \frac{0.2724}{854} \approx 3.19 \times 10^{-4}. \quad \text{(V/minute/ppt)} \quad (5.23)$$

Comparing the results of Eq.(5.20) to (5.23), all four calculations are in excellent agreement. The mean value of above four results is $\psi / C_A \approx 3.203 \times 10^{-4}$ V/minute/ppt with a standard deviation of $SD \approx 0.058 \times 10^{-4}$ V/minute/ppt.

Considering the experimental errors and other factors (such as flow fluctuations over time, etc.), the four values are close enough for us to believe the validity of (at least it consistent to) our surface adsorption model. This model is not only good for mercury/gold system, but also for other surface adsorption systems where all assumptions of this model may apply.

The correspondence between the cantilever-bending rate and mercury vapor concentration is further shown in Figure 5.6. It can be seen that the cantilever-bending rate is a linear function of mercury vapor concentration for these low exposures, and is also consistent with the surface adsorption model. Even the absolute values of the cantilever-bending rate are dependent upon the adsorbent surface coverage or the adsorbent surface rejection factor $J(t)$. However, their relative values are not affected by the surface coverage.

5.4.3 Monolayer Coverage and Long Time Exposure

In our theoretical calculation, we showed that when the adsorbate atoms arrive at the surface at a constant rate the atom accumulation rate decreases as the adsorbent surface coverage increases. Figure 5.7 shows a gold-coated cantilever bending for long exposures to a constant of mercury vapor concentrations. Comparing with the theoretical monolayer coverage (dashed line; using $N_0 / N_{Stotal} = 0.01$ as a fitting parameter), the experimental data fits the theoretical curve very well until about 60% surface coverage. The decrease of the cantilever bending rate over time indicates

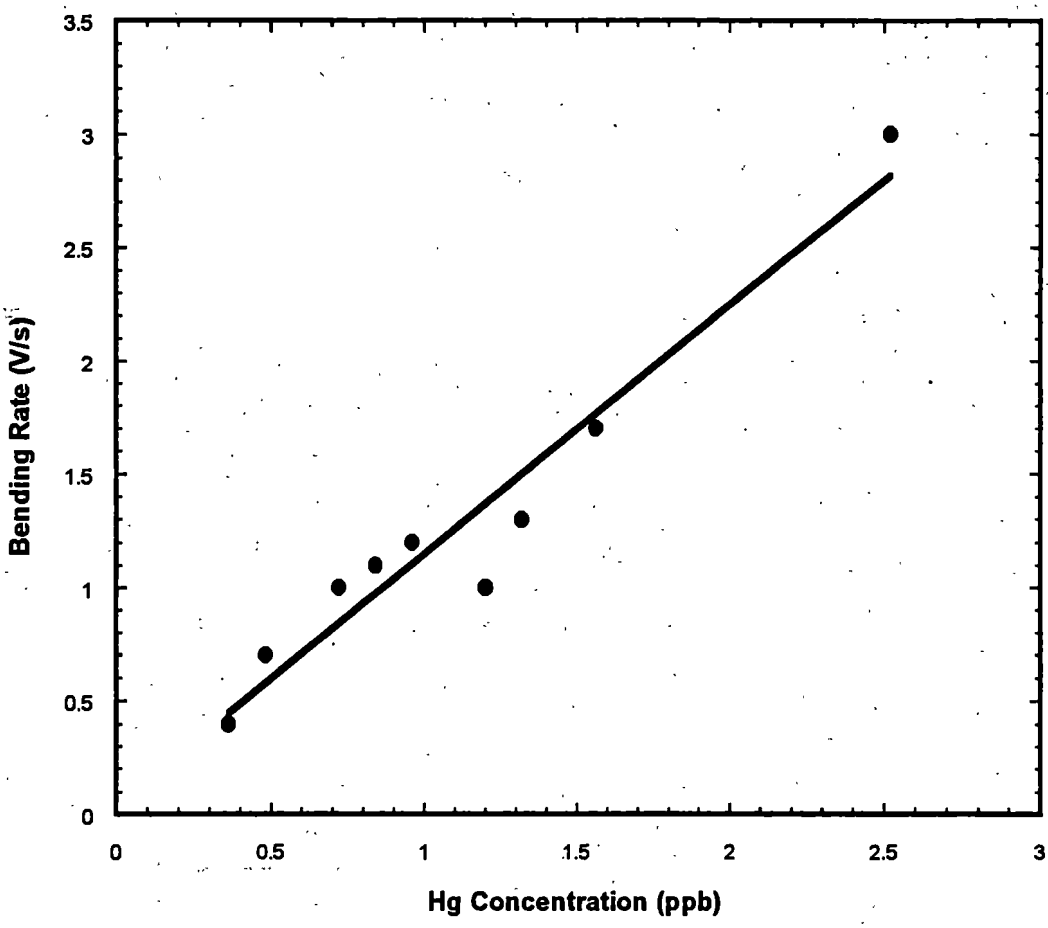


Figure 5.6: Gold-coated cantilever bending rate vs. mercury concentration.

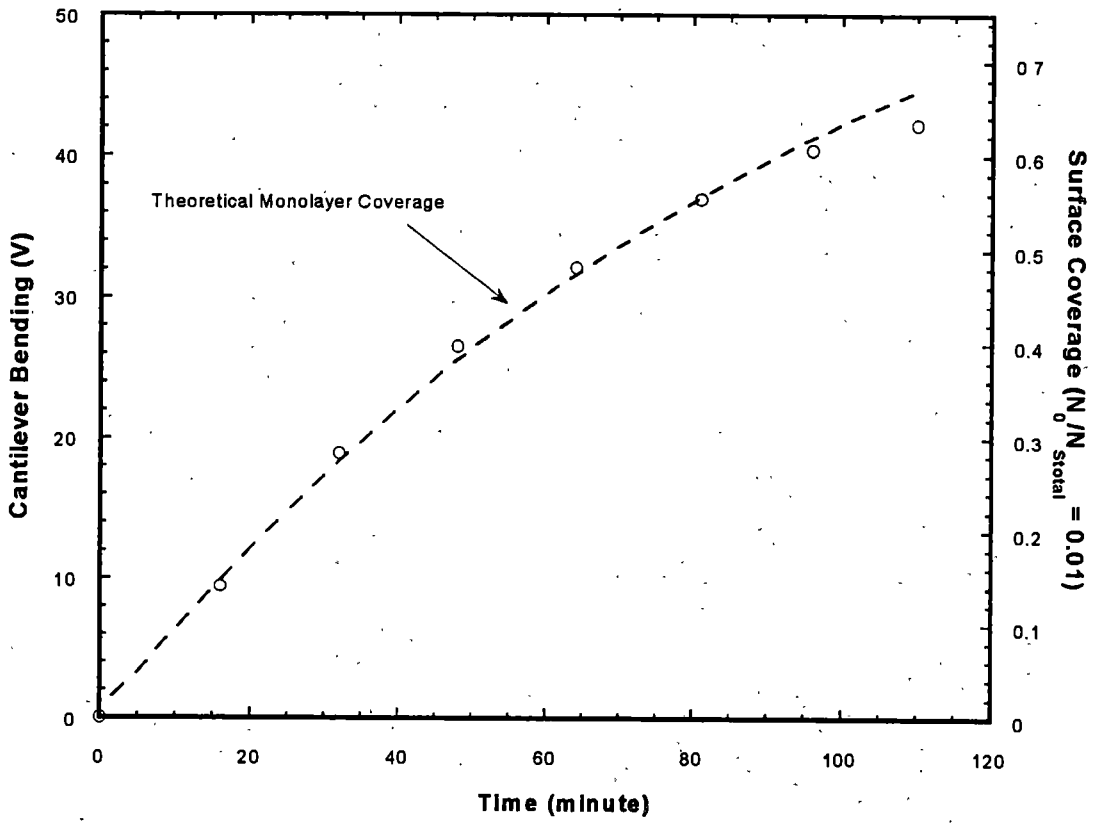


Figure 5.7: Long time mercury exposure of gold-coated cantilever .

more arriving mercury atoms being rejected by the gold surface. A linear part is at the beginning of this curve (first ~ 40 minutes). This linear part corresponds to the first one-third of surface monolayer coverage in our calculation. Other experiments, such as resistance change, mass loading induced frequency shift in quartz crystal microbalance (QCM), also show this behavior. [226, 230] Actually, most of the mercury vapor detection instruments work only in this linear range.

The cantilever bending rate ψ was defined as the rate of stress-induced cantilever bending. However, a broader definition is needed for detailed analysis. Furthermore, in addition to the stress changes due to the adsorption of mercury atom on the gold surface, gold film resistance variation and mass loading also take place. [78, 104, 226, 229, 230, 235]. Therefore, ψ can be redefined as a generalized rate parameter that can be either stress changing rate or resistance changing rate or mass deposition (frequency shifting) rate. But no matter which character ψ represents, for low vapor concentration and low surface coverage Eq.(5.11) is still valid. For high vapor concentration and high surface coverage, the adsorbent surface rejection factor J has to be taken as a correction factor. Eq.(5.11) can be rewritten as

$$\frac{\psi_1}{(1-J_1)v_{A1}C_{A1}} = \frac{\psi_2}{(1-J_2)v_{A2}C_{A2}}, \tag{5.24}$$

where J_1 and J_2 are the adsorbent surface rejection factors during periods 1 and 2, respectively, and v_{A1} and v_{A2} are the adsorbate atom arrival rates for each period. Theoretically, after including the adsorbent surface rejection factors J_1 and J_2, Eq.(5.24) should hold over the whole range of surface coverage and vapor

concentrations. However, in practice it is very difficult to precisely determine the value of J and to know every detail of the adsorption history of the adsorbent surface. Therefore, it is much easier to use a fresh or regenerated surface to conduct experiments at low vapor concentrations.

5.4.4 Gold Film Thickness Dependence

Preparing gold films in different thicknesses and exposing them to the same mercury concentration is the best way to verify if mercury adsorption at gold surface is the pure surface-adsorption mechanism assumed in our model. Taking the advantage of multi-channel signal output capability of the MUMPS chip, we prepared gold films (10.2 nm and 20 nm thick, respectively) on two microcantilevers on the same chip. Shown in Figure 5.8 is the comparison between the responses of the two cantilevers. Even when the gold film thickness on one cantilever is almost doubled, there is very little difference. In order to have a clean plot, two cantilever bending lines in this figure are given as the mean values of the actual data. This is consistent with the mercury being on the top surface of gold film just like our surface adsorption model.

5.5 Mercury Adsorption-Induced Resistance Changes in Gold Film

Similar to thr palladium/hydrogen system, the gold film resistance changes on the cantilever were also measured when it was exposed to mercury vapor. In Figure 5.9 the cantilever bending signals (for the same cantilever) were also recorded

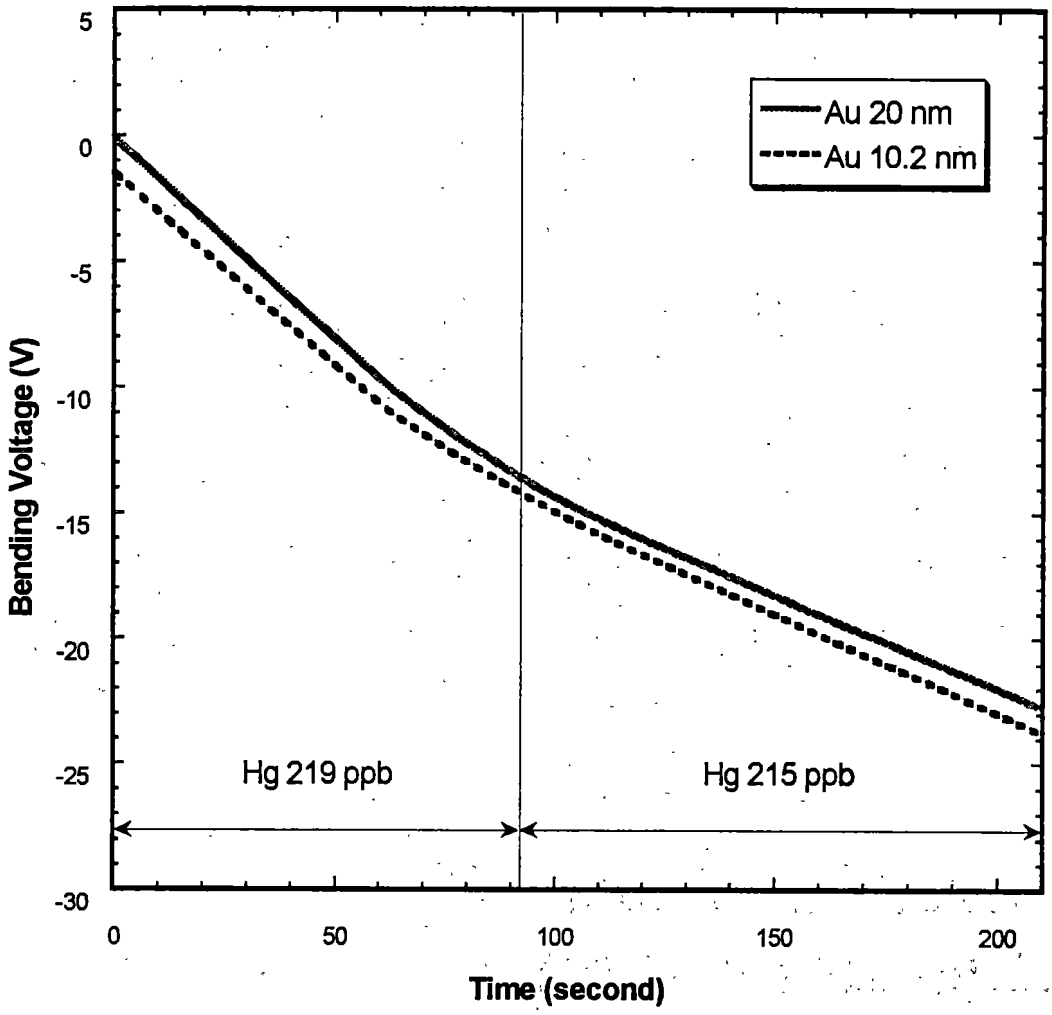


Figure 5.8: Gold thin film thickness dependences of mercury vapor.

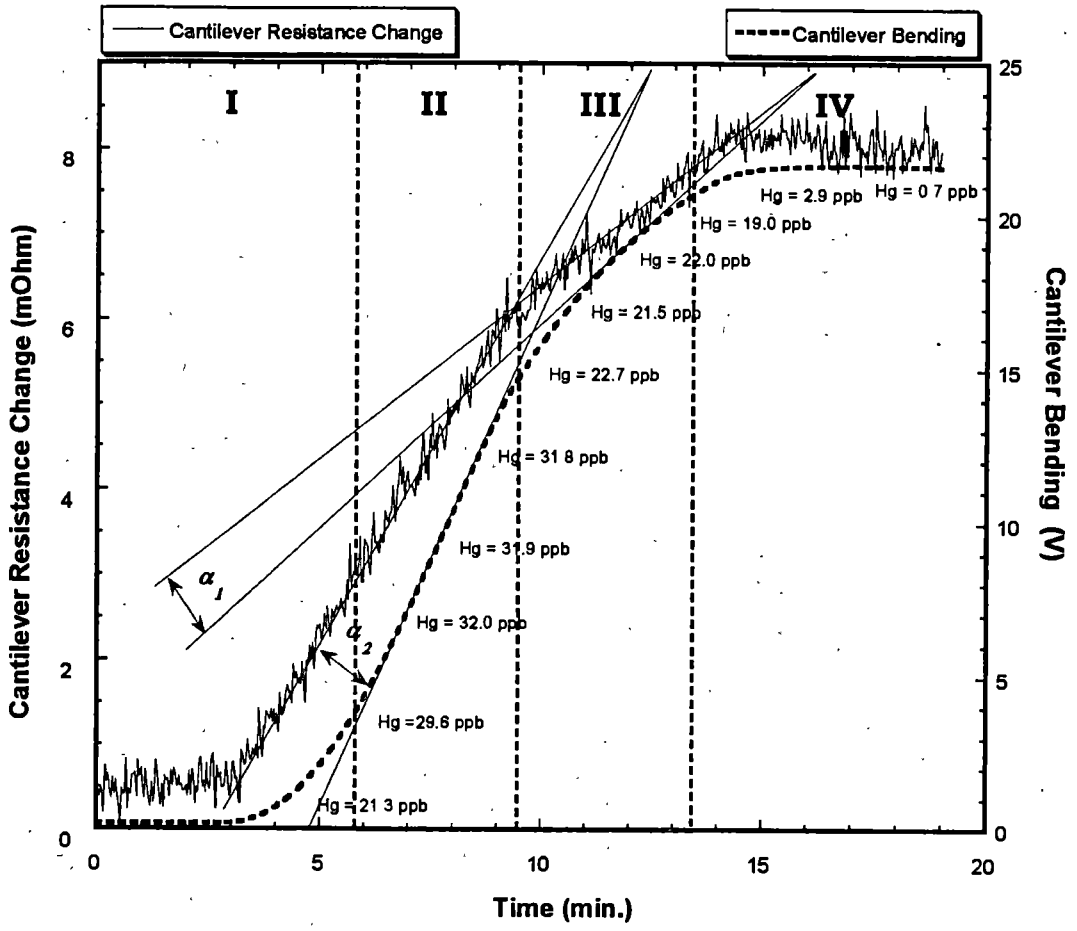


Figure 5.9: Gold-coated cantilever bending and resistance changes in mercury vapor.

simultaneously. To make it easier for discussion, this plot has been separated into four regions (I, II, II and IV). Mercury vapor were introduced in the region I and allowed it to stabilize at about 32 ppb in the region II. Then the vapor concentration was reduced to about 22 ppb in range III and cut off the mercury vapor flow in region IV. Both cantilever bending rate and gold film resistance changing rate were reduced when the mercury vapor concentration decreased from about 32 ppb to 22 ppb. Furthermore, the changing rates of both cantilever bending and gold film resistance are proportional as can be seen in the two angles α_1 and α_2. Similar to the hydrogen experiments, the signal obtained from the gold film resistance is noisier than the cantilever-bending signal.

More interesting observations can be made if the same data (used in Figure 5.9) are plotted in different way. Shown in Figure 5.10, the cantilever bending was presented as a function of the gold film resistance on the same cantilever. Previous deflected lines between the region II and III in Figure 5.9 become a straight line despite the fact that the mercury vapor concentration was changed. This provides further evidence for the generalized rate parameter ψ that was defined earlier. All characteristics (stress, resistance or mass) depend only upon the number of mercury atoms adsorbed on the gold surface.

It is also noticed that the response time between the cantilever bending and gold film resistance change is different. In Figure 5.11 the gold film resistance change acted in a much faster pace than the stress-induced cantilever bending. Unlike the palladium/hydrogen, this time constant seems not to change (at least in the

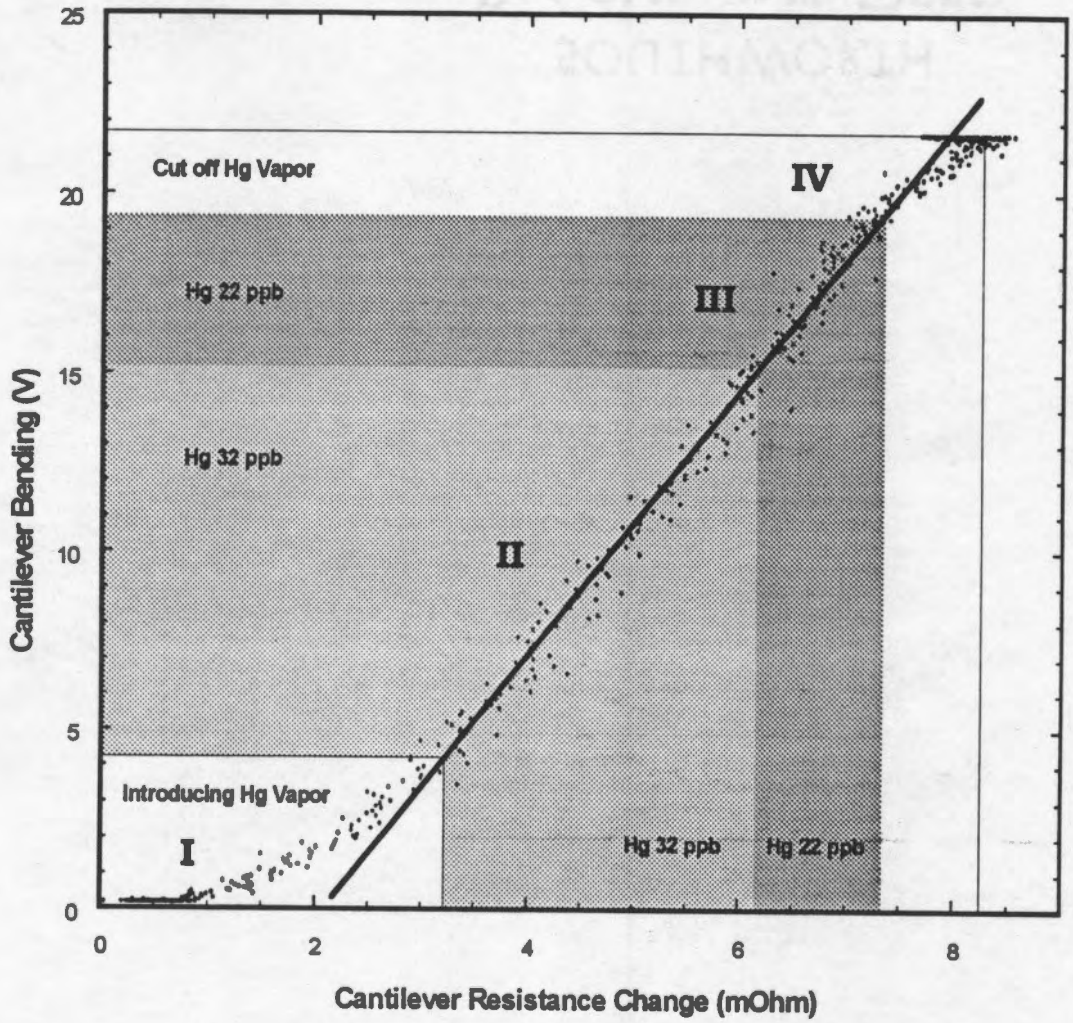


Figure 5.10: Gold-coated cantilever bending vs. gold film resistance change in mercury vapor.

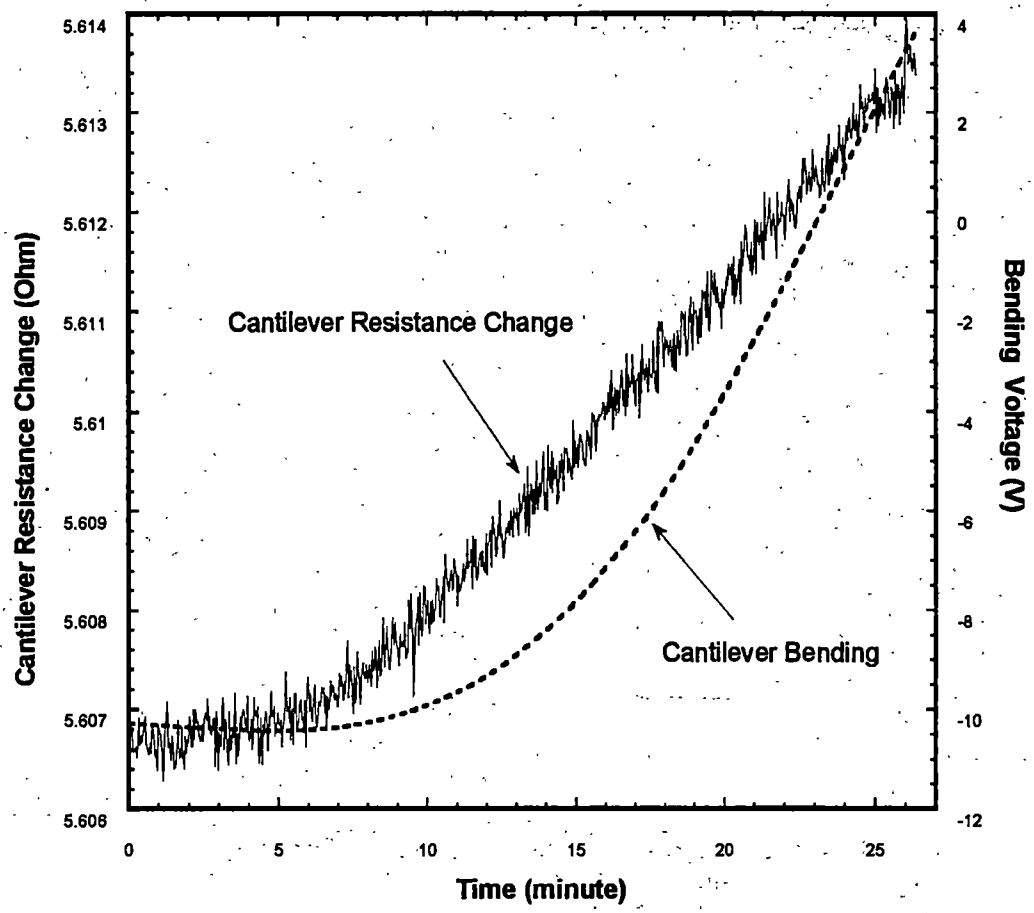


Figure 5.11: The response time differences between cantilever bending and gold film resistance change.

experiments that were performed in this thesis.) with mercury vapor concentration. The reason for this phenomenon is not clear, and further investigation is required to answer this question.

5.6 Discussions

5.6.1 Mercury Adsorption on Gold Surface

Experimental data imply that mercury adsorption on gold surface indeed is a surface-like adsorption that is very similar to what has been described in the proposed model. Therefore, both gold and mercury atoms coexist on the surface without much interaction, since further changes of both cantilever bending and gold film resistance were not observed after stopping the mercury flow. The average surface energy is the weighted average of the clean gold surface and the mercury covered surface energy. Tromp proposed that the dependence between the surface energy and monolayer coverage is a simple linear line. [245, 246]

In our experiments, it has been found that gold-coated cantilever always bent toward the uncoated side, indicating the mercury adsorption-induced surface relaxation (expansion) on gold-coated surface. Adsorption-induced surface relaxation implies the increasing of negative stress with the coverage of the monolayer. [247] In Eq.(2.40), surface stress is expressed as the sum of surface free energy and surface free energy per elastic strain. Therefore, observed mercury adsorption-induced gold surface relaxation may reflect the decreasing of the surface free energy on the gold surface.

It has been reported that after heating the exposed gold substrate to temperatures above 150 ^{0}C, the gold surface can be regenerated. [225, 230] One possible reason for this surface regeneration is that at high temperature some top-surface-adsorbed mercury atoms migrate into the bulk of gold substrate, while some of them leave the surface into vapor phase. Some positions occupied before become available for further adsorption. However, surface regeneration is not unlimited. Since mercury atoms cannot diffuse very far from the gold surface, mercury atoms will eventually take over all available spaces and positions on and near the gold surface. At this point, this gold film cannot adsorb any more mercury atoms on its surface. That is also why when the gold film thickness is more than a few nanometers, [222] increasing of the gold film thickness would have no benefit either for improving adsorption process nor for prolonging the film lifetime.

5.6.2 Microcantilever Stress Sensor

As one can see from the experimental results, microcantilevers are very sensitive to surface stress changes. Bi-material microcantilevers can be used as detectors for extremely small variation of surface stress or as a sensor for chemical detection. If one chemical (compound) can adsorb on a surface, and such adsorption processes involve surface stress changes on surfaces, microcantilevers can be used to measure such stress changes and obtain information about what kind of chemical (or compound) is involved. The gold/mercury system is just an example of one of these reaction couples.

In our experiments, gold-coated cantilevers appear to be able to sense part-per-trillion (ppt) levels of mercury vapor in nitrogen. Cantilever bending was observed in more diluted concentration, but the precise vapor concentration could not be determined because the lack of reliable reference sources. The MUMPS cantilevers were also coated with gold and palladium with different thicknesses on each of them. Then the MUMPS chip was exposed to hydrogen and mercury vapor mixture gases. The experimental results are shown in Figure 5.12. One can see that each cantilever demonstrated very distinguishable responses to the mixed gases that proved the concept of microcantilever array sensors. Carefully arranged and prepared cantilever arrays are capable of sensing multiple targets at one time.

The most common and the biggest threat to any sensor performance is contamination from the ambient. Humidity or water vapor is one of these contamination sources. The biggest trouble with humidity is that it can be found almost anywhere on the earth. To study the effects of relative humidity to the cantilever arrays, one MUMPS chip was coated with palladium (two thicknesses, 15 nm & 30 nm), gold (three thickness, 10 nm, 16 nm & 20 nm) and aluminum (17.4 nm) and left one cantilever uncoated for the reference. Then the MUMPS chip was placed in a humidity chamber. The humidity sensitivities (maximum bending / RH%) of each cantilever are shown in Figure 5.13. Thickness changes in the palladium coatings did not affect humidity sensitivities very much. In contrast, the gold-coated cantilevers showed strong thickness dependence to relative humidity changes. In other words, for water adsorption, palladium surfaces acted surface-like in adsorption, while gold surfaces acted bulk-like (sponge-like) in adsorption. The aluminum surface did not

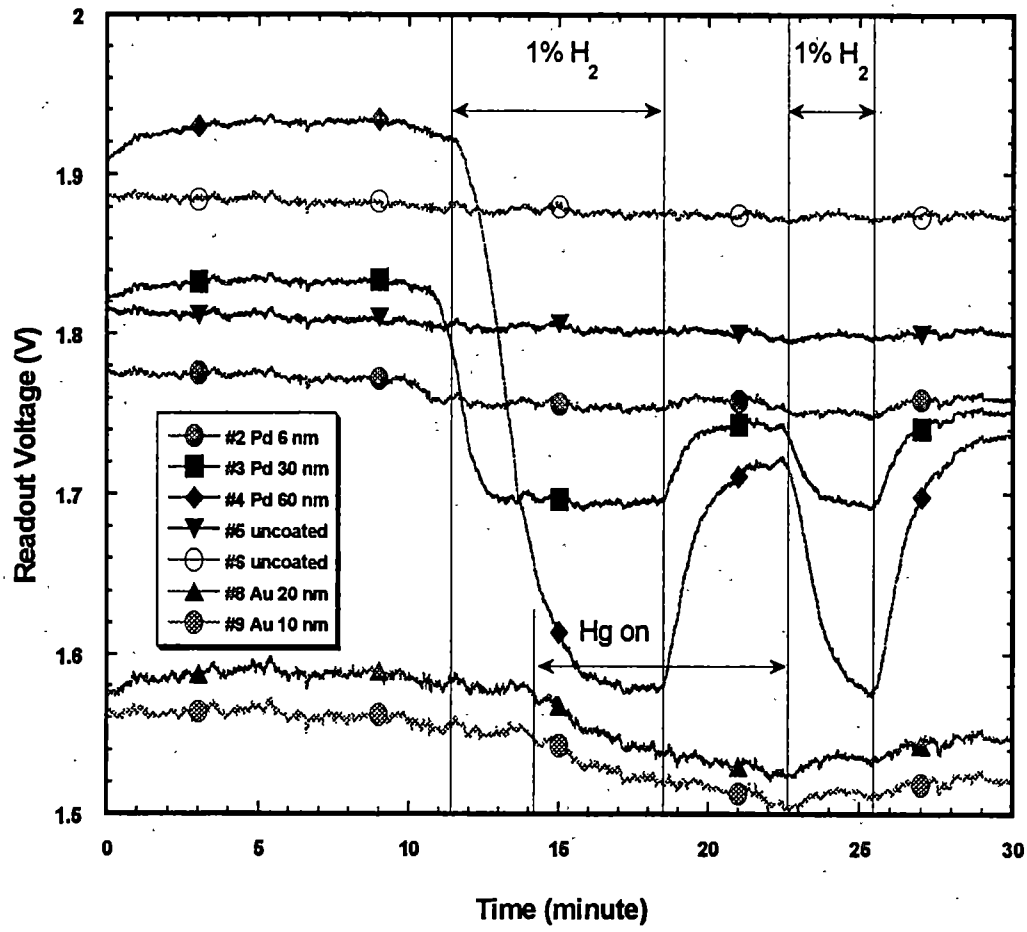


Figure 5.12: Comprehensive MUMPS chip test for both hydrogen and mercury exposures.

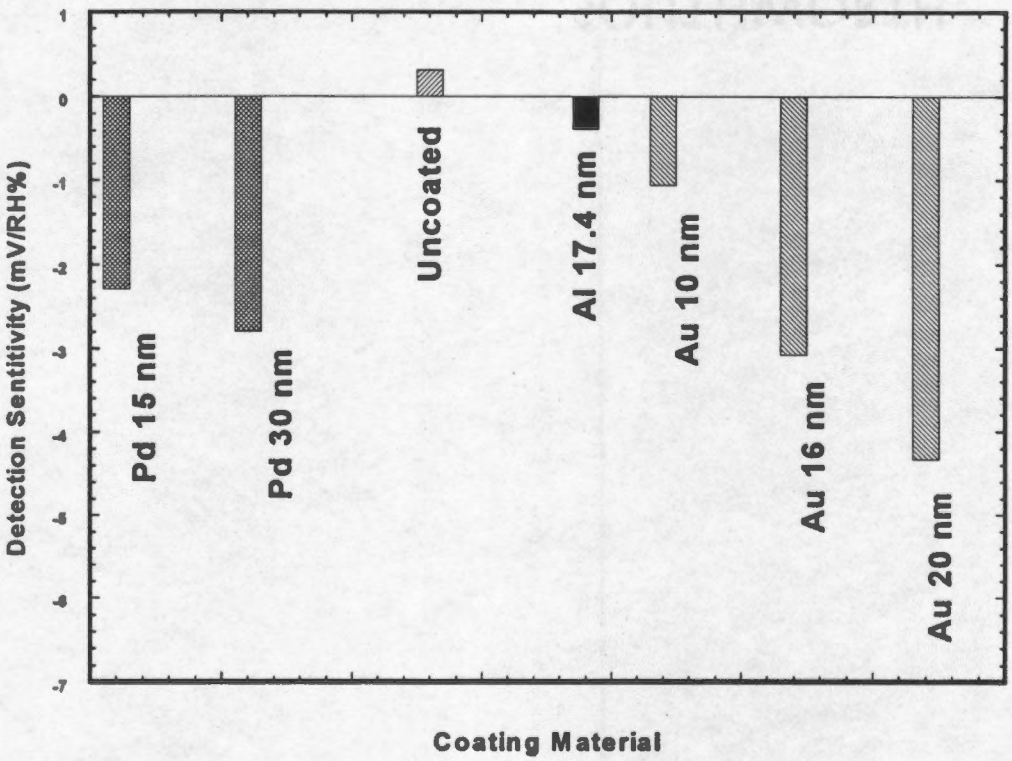


Figure 5.13: MUMPS microcantilevers coated with various thicknesses of palladium, gold and aluminum response to relative humidity.

respond to water vapor very much and the uncoated polysilicon cantilever moved toward the opposite direction, indicating a slight asymmetry.

There are ways to relieve this problem. One solution is to let the cantilever sensors work at an elevated temperature (i.e., at 100 ^{0}C). At this temperature (100 ^{0}C), little water will be adsorbed on the sensor surface. In fact, an elevated working temperature can also help reduce other contaminations (such as oil, etc.), improve the sensor response time (i.e. hydrogen atoms move much faster in and out palladium at higher temperature) and diminish the effects caused by the temperature change in the surrounding environment. However, like everything in this world no solution can solve all problems. Experiments have found that the cantilever bending sensitivity was reduced at the elevated temperatures for the palladium-coated cantilevers. More systematic tests are needed for the real sensor device development. Another way to help relieve water combination is by placing a filter or membrane to adsorb water from the sampled air on its way to the sensor chamber. The filter seems a good solution because the filter cannot only take care the water problem but it can also reduce and other contaminations. However, the lifetime of the filter and its replacement can be new problem too.

In spite of many possible problems that can affect the microcantilever sensor's performance, the many advantages of microcantilever are just too big to be ignored. This author believes that with a properly packaged design, the most problems can be reduced to the minimum. It will not take too long before many microcantilever based devices are utilized in our daily life at much lower costs.

Chapter 6

SUMMARY

The investigations in this thesis show that gas or vapor adsorptions in thin metal films can induce film stress changes. Depending on the system studied, there exist two types of gas-solid interaction: bulk-like absorption and surface-like adsorption. Either case can result in differential stresses when the metal film is attached to a thin microcantilever beam. The consequent effect is bending of the cantilever that can be related to exposure of the interacting vapor species.

In bulk-like absorption, the gas species penetrates the whole film as in the case of hydrogen in palladium that expands the lattice. The uptake of hydrogen in palladium appears to be rate-limited by a surface barrier that can be activated by initial exposure to hydrogen. An increase of film thickness increases both the sensitivity and response time of coated cantilevers and can be used to optimize the system.

For surface-like adsorption, the number of adsorbed adsorbate atoms determines film characteristics such as stress and resistance. Adjustments of film thickness have very little effect on the sensitivity and response time of coated cantilevers. Mercury adsorption onto the gold surface decreases the surface stress as evidenced by the cantilever bending away from the gold-coated side. For the first time mercury adsorption-induced stress on thin gold films is uncovered completely.

Experimental results were in good agreement with a proposed surface adsorption model, which may be very useful for future work.

Gas (vapor) adsorption on the solid surfaces may be reversible or irreversible at room temperature. For hydrogen in palladium, equilibrium is established that limits the stress and resistance at a particular external hydrogen pressure. Thus, a coated cantilever deflects to a specific position until the external pressure of hydrogen changes. In contrast, mercury adsorption onto gold is not reversible and acts as dose-integrating surface that continues to change its stress and resistance as long as there are open places for mercury to adsorb.

A novel simultaneous stress- and resistance-measurement method developed during this study revealed that more complex mechanisms are involved than a simple relationship. This innovative experimental method may offer a new approach for material property studies.

Bi-material microcantilevers have shown ultra-high stress sensitivity, which may be utilized to study thin film stress or employed as a sensor platform. Investigations of two adsorption mechanisms provided a much better understanding of gas (or vapor) adsorption onto solid surfaces as well as adsorption-induced stress. Both theoretical models and experimental results could be used to design and improve the performance of microcantilever-based sensors.

The research involved in this dissertation has been described, in part, in more than thirty publications, conference presentations and patents. The author has written or co-authored seven journal papers and has personally presented talks at international

conferences in Los Angeles, Atlanta and Hawaii. The concept of microfabricated sensor arrays has also attracted federal and private investment to develop and commercialize chemical, physical, and biological sensors. The experimental results presented here have shown that current laboratory systems can detect ppb (part-per-billion) or ppt (part-per-trillion) levels of hydrogen or mercury, respectively. Additional coatings may be chosen for detection of other vapor species. It is foreseeable that in the near-term and long-range future microcantilever-based sensors may play active, important roles in our daily lives.

BIBLIOGRAPHY

1. Binnig, G., C.F. Quate, and C. Gerber, *Atomic Force Microscope,* Phys. Rev. Lett., 1986. **56**(9): p. 930-933.
2. Binnig, G.K., *Atomic-force microscopy,* Physica Scripta (Sweden), 1987. **T19A**: p. 53-4.
3. Binnig, G., *et al.*, *Atomic Resolution with Atomic Force Microscope,* Surface Science, 1987. **189-190**: p. 1-6.
4. Marti, O. and M. Amrein, eds. *STM and SFM in Biology.* . 1993, Academic Press, Inc.: San Diego.
5. Wiesendanger, R. and H.-J. Güntherodt , eds. *Scanning Tunneling Microscopy III : Theory of STM and related scanning probe methods.* Springer series in surface sciences, ed. 29. 1993, Springer-Verlag: Berlin.
6. Wiesendanger, R., ed. *Scanning Probe Microscopy : Analytical Methods.* Nanoscience and Technology. 1998: Berlin.
7. Wiesendanger, R., *Scanning Probe Microscopy and Spectroscopy: Methods and Applications.* 1994, New York: Cambridge University Press.
8. Wiesendanger, R. and H.-J. Güntherodt , eds. *Scanning Tunneling Microscopy II : Further applications and related scanning techniques.* Springer series in surface sciences. 28. 1992, Springer-Verlag,: New York,.
9. Woodruff, D.P. and T.A. Delchar, *Modern Techniques of Surface Science.* 2nd ed. Cambridge Solid State Science Series, ed. E.A. Davis, I.M.F. Ward, and D.R. Clarke. 1994, Bambridge: Cambridge University Press.
10. Sarid, D., *Scanning Force Microscopy; with Applications to Electric, Magnetic and Atomic Forces.* Rev. ed. 1994, New York: Oxford University Press.
11. Thundat, T., *et al.*, *Atomic Force Microscope Investigation of C_{60} Adsorbed on Silicon and Mica,* Appl. Phys. Lett., 1993. **63**(7): p. 891-3.
12. Thundat, T., *et al.*, *Atomic Layer-By-Layer Surface Removal by Force Microscopy,* Surf. Sci. Lett., 1993. **293**(1-2): p. L863-9.
13. Thundat, T., *et al.*, *Atomic Force Microscopy of Single-Stranded and Double-Stranded DNA Adsorbed on Chemically Treated Mica,* Bull. Am. Phys. Soc., 1993. **38**(1): p. 118.
14. Thundat, T., *et al.*, *Role of Relative Humidity in Atomic Force Microscopy Imaging,* Surf. Sci. Lett., 1993. **294**: p. L939-43.
15. Allison, D.P., *et al.*, *Mapping Individual Cosmid DNAs by Direct AFM Imaging,* Genomics, 1997. **41**(3): p. 379-384.
16. Allison, D.P., T. Thundat, and R.J. Warmack, *Scanning Probe Microscopy in Genomic Research,* in *Automated Technologies for Genome Characterization,* T.J. Beugelsdijk, Editor. 1997, Wiley. p. 167-188.
17. Allison, D.P., *et al.*, *The Analysis of Genomes by Atomic Force Microscopy,* Scanning, 1997. **19**(3): p. 136-137.
18. Brugger, J., *et al.*, *Microfabricated Ultrasensitve Piezoresistive Cantilevers for Torque Magnetometry,* Sensors and Actuators, 1999. **73**: p. 235-242.
19. Lee, C., *et al. Smart Piezoelectric PZT Microcantilevers with Inherent Sensing and Actuating Abilities for AFM and LFM.* in *Materials Research Society 1996 Fall Meeting.* 1996.
20. Pechmann, R., *et al.*, *The Novolever: A New Cantilever for Scanning Force Microscopy Microfabricated From Polymeric Matericals,* Rev. Sci. Instrum., 1994. **65**(12): p. 3702-3706.
21. Piner, R.D., *et al.*, *"Din-Pen" Nanolithography,* Science, 1999. **283**: p. 661-663.
22. Walters, D.A., *et al.*, *Short Cantilevers for Atomic Force Microscopy,* Rev. Sci. Instrum., 1996. **67**(10): p. 3583-3590.
23. Minne, S.C., *Bringing Scanning Probe Microscopy Up to Speed.* Microsystems (series). Vol. 3. 1999, Boston.
24. Harris, J.G.E., *et al.*, *Fabrication and Characterization of 100-nm-thick GaAs Cantilevers,* Rev. Sci. Instrum., 1996. **67**(10): p. 3591-3593.
25. Meyer, G. and N.M. Amer, *Novel Optical Approach to Atomic Force Microscopy,* Appl. Phys. Lett., 1988. **53**(12): p. 1045-7.

26. Butt, H.-J., *A Sensitive Method to Measure Changes in the Surface Stress of Solids,* J. Colloid and Interface Science, 1996. **180**: p. 251-260.
27. Chen, G.Y., *et al., Adsorption-induced Surface Stress and Its Effects on Resonance Frequency of Microcantilevers,* Journal of Applied Physics, 1995. 77(8): p. 3618-3622.
28. Raiteri, R. and H.-J. Butt, *Measuring Electrochemically Induced Surface Stress with an Atomic Force Microscope,* J. Phys. Chem., 1995.
29. Thundat, T. and L. Maya, *Monitoring Chemical and Physical Changes on Sub-Nanogram Quantities of Platinum Dioxide,* Surface Science Letters, 1999. **430**: p. L546-L552.
30. Thundat, T., *et al. Highly Selective Microcantilever Sensor for Cesium Ion Detection.* in *1999 International Electrochemical Society Annual Meeting.* 1999. Honolulu, Hawaii: The Electrochemical Society, Inc.
31. Thundat, T., *et al., Microcantilever Immunosensors,* in *Immunoassays: Methods and Protocols.* 1999, Humana Press: New York.
32. Thundat, T., *et al. Microcantilever Chemical Sensors.* in *The Second Micro Nano Technology Conference.* 1999. Pasadena, CA.
33. Thundat, T.G. and E.A. Wachter, *Microcantilever Sensor,* 1998, Lockeed Martin Energy Systems, Inc. Oak Ridge, Tenn.: USA.
34. Thundat, T., P.I. Oden, and R.J. Warmack, *Chemical, Physical, and Biological Detection Using Microcantilevers,* in *Microstructures and Microfabricated Systems III,* P.J. Hesketh, G. Barna, and H.G. Hughes, Editors. 1997, The Electrochemical Society: Pennington, NJ. p. 179-187.
35. Thundat, T., P.I. Oden, and R.J. Warmack, *Microcantilever Sensors,* Microscale Thermophysical Engineering, 1997. **1**: p. 185-199.
36. Thundat, T., *et al., Micromechanical Radiation Dosimeter,* Appl. Phys. Lett., 1995. **66**: p. 1563-5.
37. Thundat, T., *et al., Vapor Detection Using Resonating Microcantilevers,* Anal. Chem., 1995. **67**(3): p. 519-521.
38. Thundat, T., *et al., Detection of Mercury Vapor Using Resonating Microcantilevers,* Appl. Phys. Lett., 1995. **66**(13): p. 1695-1697.
39. Wachter, E.A. and T. Thundat, *Micromechanical Sensors for Chemical and Physical Measurements,* Rev. Sci. Instrum., 1995. **66**(6): p. 3992-3667.
40. Wachter, E.A. and T.G. Thundat, *Microbar Sensor,* 1995, Lockheed Martin Energy Systems, Inc. Oak Ridge, Tenn.: USA.
41. Wachter, E.A., *et al., Remote Optical Detection Using Microcantilevers,* Rev. Sci. Instrum., 1996. **67**(10): p. 3434-3439.
42. Berger, R., *et al., Micromechanics: A Toolbox for Femtoscale Science: "Towards a Laboratory on a Tip",* Microelectronic Engineering, 1997. **35**: p. 373-379.
43. Britton, C.L., *et al. MEMS Sensors and Wireless Telemetry for Distributed Systems.* in *5th International Symposium on Smart Materials and Structures.* 1998. San Diego, CA: Proceedings of the International Society for Optical Engineers - SPIE.
44. Britton, C.L., *et al. Multiple-Input Microcantilever Sensor with Capacitive Readout.* in *Government Microcircuits Applications (GOMAC).* 1999. Monterey, CA.
45. Britton, C.L., Jr., *et al., Multiple-Input Microcantilever Sensors,* Ultramicroscopy, 2000. **82**: p. 17-21.
46. Chen, G., *Theory and Applications of Atomic Force Microscopy Microcantilevers,* in *Dept. of Phys. and Astro.* 1995, Univ. of Tenn.: Knoxville.
47. Datskos, P.G., *et al., Remote Infrared Radiation Detection Using Piezoresistive Microcantilevers,* Appl. Phys. Lett., 1996. **69**(20): p. 2986-2988.
48. Jones, R.L., *MEMS Cantilever Sensor System With CMOS Readout Circuit,* in *Dept. of Elec. Eng.* 1998, Univ. of Tenn.: Knoxville.
49. Hu, Z., T. Thundat, and R.J. Warmack. *Metal Coated Microcantilever Hydrogen and Mercury Sensors.* in *1999 International Electrochemical Society Annual Meeting.* 1999. Honolulu, Hawaii: The Electrochemical Society, Inc.
50. Lai, J., *et al., Optimization and Performance of High-Resolution Micro-Optomechanical Thermal Sensors,* Sensors and Actuators, 1997. **A 58**: p. 113-119.

51. Lang, H.P., *et al., A Chemical Sensor Based on a Micromechanical Cantilever Array for the Identification of Gases and Vapors,* Appl. Phys. A, 1998. **66**: p. S61-S64.
52. Maute, M., *et al., Fabrication and Application of Polymer Coated Cantilevers as Gas Sensors,* Microelec. Eng., 1999. **46**: p. 439-442.
53. Oden, P.I., *et al. Infrared Imaging Using Microcantilevers.* in *The American Society of Mechanical Engineers Symposium on Microscale Thermal Phenomena in Electronic Systems (MEMS).* 1996. Atlanta, Georgia: American Society of Mechanical Engineers.
54. Oden, P.I., *et al., Uncooled Thermal Imaging Using a Piezoresistive Microcantilever,* Appl. Phys. Lett., 1996. **69**(21): p. 3277-79.
55. Warmack, R.J., *et al. Multiple-Input Microcantilever Sensor with Capacitive Readout.* in *Hilton Head Sensors and Actuators Conference.* 1998. Hiltion Head, SC.
56. Young, D.M. and A.D. Crowell, *Physical Adsorption of Gases.* 1962, Washington, D. C.: Butterworths & Co.
57. Metals, A.S.f. *Thin Films: papers presented at a seminar of the American Society for Metals, October 19 and 20, 1963.* 1963. Metals Park, Ohio: American Society for Metals.
58. Thun, R.E., *Structure of Thin Films,* in *Physics of Thin Films: Advances in Research and Development,* G. Hass, Editor. 1963, Academic Press: New York and London. p. 187-232.
59. Chopra, K.L., *Thin Film Phenomena.* 1969, New York: McGraw-Hill Book Co.
60. Blech, I.A. and E.S. Meieran, *Enhanced X-ray Diffraction from Substrate Crystals Containing Discontinuous Surface Filems,* J. Appl. Phys., 1967. **38**(7): p. 2913-2919.
61. Blech, I. and U. Cohen, *Effects of Humidity on Stress in Thin Silicon Dioxide Films,* J. Appl. Phys., 1982. **53**(6): p. 4202-4207.
62. Braunstein, A.I., *Calculation of Electric Field and Absorption Distributions in Thin Film Structures,* Thin Solid Films, 1976. **37**: p. 181-184.
63. Brundle, C.R., C.A.J. Evans, and S. Wilson, *Encyclopedia of Materials Characterization: Surfaces, Interfaces , Thin Films.* Materials Characterization Series, ed. C.R. Brundle and C.A.J. Evans. 1992, Boston, London: Butterworth-Heinemann.
64. Hoffman, R.W., *Mechanical Properties of Thin Films,* in *Thin Films.* p. 99-134.
65. Fogelberg, J., *et al., Kinetic Modeling of Hydrogen Adsorption/Absorption in Thin Films on Hydrogen-Sensitive Field-Effect Devices: Observation of Large Hydrogen-Induced Dipoles at the Pd-SiO_2 Interface,* J. Appl. Phys., 1995. **78**(2): p. 988-996.
66. Jesson, D.E., *et al., Crack-Like Sources of Dislocation Nucleation and Multiplication in Thin Films,* Science, 1995. **268**: p. 1161-1163.
67. Kalli, K., A. Othonos, and C. Christofides, *Temperature-Induced Reflectivity Changes and Activation of Hydrogen Sensitive Optically Thin Palladium Films on Silicon Oxide,* Rev. Scientific Instrum., 1998. **69**(9): p. 3331-3338.
68. Maissel, L., I. and R. Glang, eds. *Handbook of Thin Film Technology.* . 1970, McGraw_Hill Book Co.: New York.
69. McGinnis, W.C. and P.M. Chaikin, *Electron Localization and Interaction Effects in Palladium and Palladium-Gold Films,* Phys. Rev. B, 1985. **32**(10): p. 6319-6330.
70. Yoshida, Z., *Preparation of An Ideal Thin Mercury Film Electrode and Its Electrochemical Property,* Bull. Chem. Soc. Jpn., 1981. **54**: p. 562-567.
71. Priest, J., H.L. Caswell, and Y. Budo, *Mechanical Stresses in Silicon Oxide Films,* Vacuum, 1962. **12**: p. 301-306.
72. Parker, R.L. and A. Krinsky, *Electrical Resistance-Strain Characteristics of Thin Evaporated Metal Films,* J. Appl. Phys., 1963. **34**(9): p. 2700-2708.
73. Munitz, A. and Y. Komem, *Structural and Resistivity Changes in Heat-Treated Chromium-Gold Films,* Thin Solid Films, 1976. **37**: p. 171-179.
74. Windischmann, H., *Intrinsic Stress in Sputter-Deposited Thin Films,* CRC Critical Reviews in Solid State and Materials Sciences, 1992. **17**(6): p. 547-596.
75. Zhu, W., *et al., Synthesis, Microstructure and Electrical Properties of Hydrothermally Prepared Ferroelectric $BaTiO_3$ Thin Films,* J. Electroceramics, 1998. **2**(1): p. 21-31.
76. Story, H.S. and R.W. Woffman, *Stress Annealing in Vacuum Deposited Copper Films,* Proc. Phys. Soc. London, 1957. **B70**: p. 950-960.

77. Hutchison, T.S. and D.C. Baird, *The Physics of Engineering Solids*. 2nd ed. 1967, New York: John Wiley and Sons, Inc.
78. McNerney, J.J. and P.R. Buseck, *Mercury Detection by Means of Thin Gold Films*, Science, 1972. **178**(10 November): p. 611-612.
79. Coutts, T.J., *Electrical Conduction in Thin Metal Films*. 1974, New York: Elsevier Scientific Publishing Co.
80. Pollock, D.D., *Electrical Conduction in Solids: An Introduction*. 1985, Metals Park, Ohio: American Society for Metals.
81. Fuchs, K., *The Conductivity of Thin Metallic Films According to The Electron Theory of Metals*, Proc. Cambridge Phil. Soc., 1938. **34**: p. 100-108.
82. Masel, R.I., *Pinciples of Adsorption and Reaction on Solid Surfaces*. Wiley Series in Chemical Engineering. 1996, New York: John Wiley & Sons, Inc.
83. Ross, S. and J.P. Olivier, *On Physical Adsorption*. 1964, New York; London; Sydney: Interscience Publishers (a Division of John Wiley & Sons, Inc.).
84. Tompkins, F.C., *Chemisorption of Gases on Metals*. 1978, New York: Academic Press.
85. Ricco, A.J.G.C., ed. *Solid-State Sensor and Actuator Workshop*. . 1998, Transducers Research Foundation, Inc.: Hilton head Island, SC.
86. Britton, C.L., *et al. Battery-Powered, Wireless MEMS Sensors for High-Sensitivity Chemical and Biological Sensing*. in *Advanced Research in VLSI*. 1999. Atlanta, GA.
87. Hu, C., *Silicon Nanolelectronics for the 21st Century*, Nanotech., 1999. **10**: p. 113-116.
88. Barnes, J.R., *et al., A Femtojoule Calorimeter using Micromechanical Sensors*, Rev. Sci. Instrum., 1994. **65**(12): p. 3793-3798.
89. Ferreira, L.O.S. and S. Moehlecke, *A Silicon Micromechanical Galvanometric Scanner*, Sensors and Actuators, 1999. **73**: p. 252-260.
90. Thomas, R.C. and R.C. Hughes, *Sensors for Detecting Molecular Hydrogen Based on Pd Metal Alloys*, J. Electrochem. Soc., 1997. **144**(9): p. 3245-3249.
91. Tabib-Azar, M., *et al., Highly Sensitive Hydrogen Sensors using Palladium Coated Fiber Optics with Exposed Cores and Evanescent Field Interactions*, Sensors and Acuators, 1999. **B**(56): p. 158-163.
92. Shaver, P.J., *Bimetal Strip Hydrogen Gas Detectors*, The Review of Scientific Instruments, 1969. **40**(7): p. 901-904.
93. Maffei, N. and A.K. Kuriakose, *A Hydrogen Sensor Based on a Hydrogen Ion Conducting Solid Electrolyte*, Sensors and Actuators, 1999. **B**(56): p. 243-246.
94. Lundstrom, I. and D. Soderberg, *Hydrogen Sensitive MOS-Structures Part1: Principles and Applications*, Sensors and Actuators, 1981. **1**: p. 403-426.
95. Lundstrom, I. and D. Soderberg, *Hydrogen Sensitive MOS-Structures Part2: Characterization*, Sensors and Actuators, 1981/82. **2**: p. 105-138.
96. Levlin, M., *et al., Mercury Adsorption on Gold Surfaces Employed in the Sampling and Determination of Vaporous Mercury: A Scanning Tunneling Microscopy Study*, J. Anal. Chem., 1996. **355**: p. 2-9.
97. Korolczuk, M., *Sensitive and Selective Determination of Mercury by Differential Pulse Stripping Voltammetry after Accumulation of Mercury Vapor on a Gold Plated Graphite Electrode*, J. Anal. Chem., 1997. **357**: p. 389-391.
98. Johansson, M., I. Lundstrom, and L.-G. Ekedahl, *Bridging the Pressure Gap for Palladium Metal-Insulator-Semiconductor Hydrogen Sensors in Oxygen Containing Environments*, J. Appl. Phys., 1998. **84**(1): p. 44-51.
99. Janega, P. and L. Young, *Palladium-Silver Alloy Gates in Metal-Oxide-Semiconductor Structures for Use as Hydrogen Sensors*, J. Electrochemical Society, 1987. **134**(Jan.): p. 252-253.
100. Hughes, R.C., *et al., Thin-Film Palladium and Silver Alloys and Layers for Metal-Insulator-Semiconductor Sensors*, J. Appl. Phys., 1987. **62**(3): p. 1074-1083.
101. Hughes, R.C., W.K. Schubert, and R.J. Buss, *Solid-State Hydrogen Sensors Using Palladium-Nickel Alloys: Effect of Alloy Composition on Sensor Response*, J. Electrochem. soc., 1995. **142**(1): p. 249-254.

102. Hughes, R.C. and W.K. Schubert, *Thin Films of Pd/Ni Alloys for Detection of High Hydrogen Concentrations,* J. Appl. Phys., 1992. **71**(1): p. 542-544.
103. Himmelhaus, M., M. Buck, and M. Grunze, *Mercury Induced Reorientation of Alkanethiolates Adorbed on Gold,* Appl. Phys. B, 1999. **68**(3): p. 595-598.
104. George, M.A., *et al.*, *Investigation of Mercury Adsorption on Gold Films by STM,* J. Microscopy, 1988. **152**(3): p. 703-713.
105. Eriksson, M. and L.-G. Ekedahl, *Hydrogen Adsorption States at the Pd/SiO_2 Interface and Simulation of the Response of A Pd Metal-Oxide-Semiconductor Hydrogen Sensor,* J. Appl. Phys., 1998. **83**(8): p. 3947-3951.
106. Ekedahl, L.-G., M. Eriksson, and I. Lundstrom, *Hydrogen Sensing Mechanisms of Metal-Insulator Interfaces,* Accounts of Chemical Research, 1998. **31**(5): p. 249-256.
107. Dobos, K., *et al.*, *The Influence of Different Insulators on Palladium-Gate Metal_Insulator-Semiconductor Hydrogen Sensors,* IEEE Trans. Electron Devices, 1984. **ED-31**(4): p. 508-510.
108. D'Amico, A., A. Palma, and E. Verona, *Surface Acoustic Wave Hydrogen Sensor,* Sensors and Actuators, 1982/83. **3**: p. 31-39.
109. Chaudhary, V.A., I.S. Mulla, and K. Vijayamohanan, *Selective Hydrogen Sensing Porperties of Surface Functionalized Tin Oxide,* Sensors and Actuators, 1999. **B**(55): p. 154-160.
110. Butler, M.A., A.J. Ricco, and R.J. Baughman, *Hg Adsorption of Optically Thin Au Films,* J. Appl. Phys., 1990. **67**(9): p. 4320-4326.
111. Butler, M.A. and D.S. Ginley, *Hydrogen Sensing with Palladium-coated Optical Fibers,* J. Appl. Phys., 1988. **64**(7): p. 3706-3712.
112. Butler, M.A., *Micromirror Optical-Fiber Hydrogen Sensor,* Sensors and Actuators, 1994. **B**(22): p. 155-163.
113. Butler, M.A., *Fiber Optic Sensor for Hydrogen Concentrations near the Explosive Limit,* J. Electrochem. Soc., 1991. **138**(9): p. L46-L47.
114. Beinrohr, E., *et al.*, *Calibrationless Determination of Mercury by Flow-through Stripping Coulometry,* J. Anal. Chem., 1996. **356**: p. 253-258.
115. Armgarth, M. and C. Nylander, *Blister Formation in Pd Gate MIS Hydrogen Sensors,* IEEE Electron Device Letters, 1982. **EDL-3**(12): p. 384-386.
116. Rossow, E.C., *Analysis and Behavior of Structures.* 1996, Upper Saddle River, New Jersey: Prentice Hall.
117. Jenkins, W.M., *Chapter 6: The Analysis of Beams,* in *Structural Analysis Using Computers,* W.M. Jenkins, Editor. 1990, Longman Scientific & Technical: New York. p. 92-143.
118. Paz, M., *Structural Dynamics: Theory and Computation.* 4th ed. 1997, New York: Chapman & Hall; International Thomson Publishing.
119. Bhushan, B., *Handbook of Micro/Nano Tribology.* 2nd ed. The mechanics and materials science series. 1999.
120. Tabib-Azar, M., *Microactuators: Electrical, Magnetic, Thermal, Optical, Mechanical, Chemical & Smart Structures.* The Kluwer International Series In: Electronic Materials: Science and Technology, ed. H.L. Tuller. 1998, Boston; London: Kluwer Academic Publishers.
121. Young, W.C., *Roark's Formulas for Stress and Strain.* 6th ed. 1989, New York: McGraw-Hill Book Company.
122. Fukai, Y. and H. Sugimoto, *Diffusion of Hydrogen in Metals,* Adv. in Phys., 1985. **34**(2): p. 263-326.
123. Smith, D., *Hydrogen in Metals.* 1948, Chicago, Illinois: University of Chicago Press.
124. Fullenwinder, M., *Hydrogen Entry and Action in Metals.* 1983, New York, Oxford: Pergamon Press.
125. Hodgman, C., D., *et al.*, eds. *Handbook of Chemistry and Physics.* . 1962, The Chemical Rubber Publishing Co.: Cleveland, Ohio.
126. Barrer, R.M., *Diffusion In and Through Solids.* 1951, Cambridge: Cambridge University Press.
127. Jost, W., *Diffusion in Solids, Liquids, Gases.* Physical Chemistry-A Series of Nonographs, ed. E. Hutchinson. 1952, New York: Academic Press Inc., Publishers.
128. Stark, J.P., *Solid State Diffusion.* 1983, Malabar, Florida: Robert E. Krieger Publishing Co.

129. Aaronson, H.I., ed. *Diffusion: Papers presented at a seminar of the American Society for Metals, October 14 and 15, 1972.* . 1973, American Society for Metals: Metals Park, Ohio.
130. Ash, R. and R.M. Barrer, *Diffusion with a Concentration Discontinuity: The Hydrogen-Palladium System,* J. Phys. Chem. Solids, 1960. **16**: p. 246-252.
131. Dayananda, M.A. and G.E. Murch, eds. *Diffusion in Solids: Recent Developments.* . 1985, The Metallurgical Society: Warrendale, Pennsylvania.
132. Feibelman, P.J. and R. Stumpf, *Adsorption-Induced Lattice Relaxation and Diffusion by Concerted Substitution,* Phys. Rev. B, 1999. 59(8): p. 5892-5897.
133. Devanathan, M.A.V. and Z. Stachurski, *The Adsorption and Diffusion of Electrolytic Hydrogen in Palladium,* Proc. of a Royal Society of London, 1962. **A270**: p. 90-102.
134. Frank, R.C. and J.E.J. Thomas, *The Diffusion of Hydrogen in Single-Crystal Germanium,* J. Phys. Chem. Solids, 1960. **16**: p. 144-151.
135. Holleck, G.L., *Diffusion and Solubility of Hydrogen in Palladium and Palladium-Silver Alloys,* J. Phys. Chem., 1970. 74(3): p. 503-511.
136. Jewett, D.N. and A.C. Makrides, *Diffusion of Hydrogen Through Palladium and Palladium-Silver Alloys,* Trans. Faraday Soc., 1965. **61**: p. 932-939.
137. Nowick, A.S. and J.J. Burton, eds. *Diffusion in Solids: Recent Developments.* Materials Science and Technology, ed. A.M. Alper, J.L. Margrave, and A.S. Nowick. 1975, Academic Press: New York.
138. Sakamoto, Y., *et al., "Uphill" Hydrogen Diffusion Effects of Hydrogen Interstitial Strain Gradients in Palladium and Palladium Alloys,* 1996.
139. Schmiz, G., *et al., Diffusion of Hydrogen Through Metallic Multilayers,* Phys, Rev. B, 1998. **58**(11): p. 7333-7339.
140. Silberg, P.A. and C.H. Bachman, *Diffusion of Hydrogen in Palladium,* J. Chem. Phys., 1958. **29**(4): p. 777-781.
141. Simons, J.W. and T.B. Flanagan, *Diffusion of Hydrogen in the α-phase of the Palladium-Hydrogen System,* J. Phys. Chem., 1965. **69**(10): p. 3581-3587.
142. Tong, X.Q., *et al.; "Uphill" Hydrogen Diffusion Effects and Hydrogen Diffusion Coefficients in Palladium,* Int. J. Hydrogen Energy, 1997. **22**(2/3): p. 141-144.
143. Mutschele, T. and R. Kirchheim, *Segregation and Diffusion of Hydrogen in Grain Boundaries of Palladium,* Scripta Metallurgica, 1987. **21**: p. 135-140.
144. Li, Y. and G. Wahnstrom, *Molecular-Dynamics Simulation of Hydrogen Diffusion in Palladium,* Phys. Rev. B, 1992. 46(22): p. 14528-14542.
145. Levine, H.S. and C.J. MacCallum, *Grain Boundary and Lattice Diffusion in Polycrystalline Bodies,* J. Appl. Phys., 1960. **31**(3): p. 595-590.
146. Knapton, A.G., *Palladium Alloys for Hydrogen Diffusion Membranes,* Platinum Met. Rev., 1977. **21**: p. 44-50.
147. Kirkaldy, J.S. and D.J. Young, *Diffusion in the Condensed State.* 1987, London: The Institute of Metals.
148. Kaur, I., w. gust, and L. Kozma, *Handbook of Grain and Interphase Boundary Diffusion Data.* Vol. 2. 1989, Stuttgart: Ziegler Press.
149. Beachem, C.D., *Hydrogen Damage.* 1977, Metals Park, Ohio: American Society for Metals.
150. Moody, N.R. and A.W. Thompson, eds. *Hydrogen Effects on Material Behavior.* . 1989, TMS Minerals, Metals and Materials: Warrendale, Pennsylvania.
151. Ash, R. and R.M. Barrer, *Permeation of Hydrogen through Metals,* Phil. Mag., 1959. **4**: p. 1197-1206.
152. Alefeld, G. and J. Volkl, *Hydrogen in Metals II: Application-Oriented Properties.* Topics in Applied Physics, ed. H.K.V. Lotsch. Vol. 29. 1978, New York: Springer-Verlag.
153. Wipf, H., ed. *Hydrogen in Metals III: Properties and Applications.* Topics in Applied Physics, ed. H.K.V. Lotsch. Vol. 73. 1997, Springer-Verlag: New York.
154. Schlapbach, L., ed. *Hydrogen in Intermetallic Compounds II.* Topics in Applied Physics, ed. H.K.V. Lotsch. Vol. 67. 1992, Springer-Verlag: Topics in Applied Physics.
155. Schlapbach, L., ed. *Hydrogen in Intermetallic Compounds I.* Topics in Applied Physics, ed. H.K.V. Lotsch. Vol. 63. 1988, Springer-Verlag: New York.
156. Crank, J., *The Mathematics of Diffusion.* 2nd ed. 1975, Oxford: Clarendon Press.

157. Crank, J., *Free and Moving Boundary Problems*. 1984, Oxford: Clarendon Press.
158. Carslaw, H.S. and J.C. Jaeger, *Conduction of Heat in Solids*. 2nd ed. 1969, Oxford: The Clarendon Press.
159. Howe, J.M., *Interfaces in Materials: Atomic Structure, Thermodynamics and Kinetics of Solid-Vapor, Solid-Liquid and Solid-Solid Interfaces*. 1997, New York: John Wiley & Sons, Inc.
160. Feibelman, P.J., *First-Principles Calculations of Stress Induced by Gas Adsorption on Pt(111)*, Phys. Rev. B, 1997. **56**(4): p. 2175-2182.
161. Puers, R. and D. Lapadatu, *Electrostatic Forces and Their Effects on Capacitive Mechanical Sensors*, Sensors and Actuators, 1996. **A56**: p. 203-210.
162. Eckertova, L., *Physics on Thin Films*. 1977, New York; London: Plenum Press.
163. Sondheimer, E.H., *The Mean Free Path of Electrons in Metals*, Advances in Physics, 1952. **1**(1): p. 1-42.
164. McClanahan, D. and N. Laegreid, *Production of Thin Films by Controlled Deposition of Sputtered Material*, in *Sputtering by Particle Bombardment III*, R. Behrisch and K. Wittmaack, Editors. 1991, Springer-Verlag: Berlin; Heidelberg. p. 339-377.
165. Borghesi, A. and A. Piaggi, *Palladium (Pd)*, in *Handbook of Optical Constants of Solids II*, E.D. Palik, Editor. 1991, Academic Press, Inc.: Boston. p. 469-476.
166. Lynch, C.T., *Practical Handbook of Materials Science*. 1989, Boca Raton, Fla.: CRC Press.
167. Brady, G.S. and H.R. Clauser, *Materials Handbook*. 13th ed. 1991, New York: McGraw-Hill, Inc.
168. Ma, Y.H., *Dense Palladium and Perovskite Memberanes and Membrane Reactors*, MRS Bulletin, 1999. **24**(3): p. 46-49.
169. Weast, R.C. and S.M. Selby, eds. *Handbook of Chemistry and Physics*. 47th ed. . 1966, The Chemical Rubber Co.: Cleveland, Ohio.
170. Valerio, E.L., D.W. Vanosdell, and D.G. Welles, *Chapter 44: Control of Gaseous Indoor Air contaminants*, in *1999 ASHRAE Handbook: Heating, Ventilating and Air-Conditioning Applications*, R.A. Parsons and C.D. Tate, Editors. 1999, American Society of heating, Refrigerating and Air-Conditioning Engineers, Inc.: Atlanta, GA.
171. Alefeld, G. and J. Volkl, eds. *Hydrogen in Metals I: Basic Properties*. Tipics in Applied Physics. Vol. 28. 1978, Springer-Verlag: Berlin, New York.
172. Greenwood, N.N. and A. Earnshaw, *Chemistry of the Elements*. 1984, Oxford; New York: Pergamon Press.
173. Lewis, F.A., *The Palladium Hydrogen System*. 1967, New York, London: Academic Press.
174. Kolachev, B.A., *Hydrogen Embrittlement of Nonferrous Metals*. 1968, Jerusalem: Israel Program for Scientific Translations.
175. Nakatsuji, H. and M. Hada, *Interaction of a Hydrogen Molecule with Palladium*, Journal of American Chemical Society, 1985. **107**: p. 8264-8266.
176. Nakatsuji, H., M. Hada, and T. Yonezawa, *Theoretical Study on the Chemisorption of a Hydrogen Molecule on Palladium*, J. of Am. Chem. Soc., 1987. **109**: p. 1902-1912.
177. Behm, R.J., *et al.*, *Evidence for "Subsurface" Hydrogen on Pd(110): An Intermediate Between Chemisorbed and Dissolved Species*, J. Chem. Phys., 1983. **78**(12): p. 7486-7490.
178. Blackford, B.L., *et al.*, *A Scanning Tunneling Microscope Study of A Palladium Sphere in Hydrogen Gas: Expansion and Surface Topology*, J. Appl. Phys., 1994. **76**(7): p. 4054-4060.
179. Brodowsky, H., *Das System Palladium/Wasserstoff*, Zeitschrift fur Physikalische Chemie Neue Folge, 1965. **1965**(44): p. 129-142.
180. Brodowsky, H. and E. Poeschel, *Wasserstoff in Palladium/Silber-Legierungen*, Zeitschrift fur Physikalische Chemie Neue Folge, 1965. **44**(S): p. 143-159.
181. Cabrera, A.L., *et al.*, *Structural Changes Induced by Hydrogen Absorption in Palladium and Palladium-Ruthenium Alloys*, Appl. Phys. Lett., 1995. **66**(10): p. 1216-1218.
182. Davenport, J.W., G.J. Dienes, and R.A. Johnson, *Surface Effects on the Kinetics of Hydrogen Absorption by Metals*, Physical Review B, 1982. **25**(4): p. 2165-2174.
183. Eberhardt, W., F. Greuter, and E.W. Plummer, *Bonding of H to Ni, Pd, and Pt Surfaces*, Physical Review Letters, 1981. **46**(13, April 20): p. 1085-1088.
184. Elsasser, C., *et al.*, *Vibrational States for Hydrogen in Palladium*, Phys. Rev. B, 1991. **44**(18): p. 10377-10380.

185. Fogelberg, J. and L.-G. Petersson, *Kinetic Modeling of the H_2 - O_2 Reaction on Pd and of its Influence on the Hydrogen Response of a Hydrogen Sensitive Pd Metal-Oxide-Semiconductor Device,* Surface Science, 1996. **350**: p. 91-102.
186. Gronbeck, H., *et al.*, *Hydrogen Induced Melting of Palladium Clusters,* Z. Phys. D, 1997. **40**(1-4): p. 469-471.
187. Gross, A., S. Wilke, and M. Scheffler, *Six-Dimensional Quantum Dynamics of Adsorption and Desorption of H_2 at Pd(100): Steering and Steric Effects,* Physical Revies Letters, 1995. 75(14, Oct. 2): p. 2718-2721.
188. Gross, A. and M. Scheffler, *Ab initio Quantum and Molecular Dynamics of the Dissociative Adsorption of Hydrogen of Pd (100),* Phys. Rev. B, 1998. **57**(4): p. 2493-2506.
189. Halstead, D. and S. Holloway, *The Influence of Potential Energy Surface Topologies on the Dissociation of H_2,* J. Chem. Phys., 1990. **93**(4): p. 2859-2870.
190. Kay, B.D., C.H.F. Peden, and D.W. Goodman, *Kinetics of Hydrogen Absorption by Pd(110),* Phys. Rev. B, 1986. **34**(2): p. 817-822.
191. Ledentu, V., *et al.*, *H-Induced Reconstructions on Pd (110),* Phys. Rev. B, 1998. **57**(19): p. 12482-12491.
192. Nylander, C., M. Armgarth, and C. Sversson, *Hydrogen Induced Drift in Palladium Gate Metal-Oxide-Semiconductor Structures,* J. Appl. Phys., 1984. **56**(4, 15 Aug.): p. 1177-1188.
193. Lundstrom, I., *et al.*, *A Hydrogen-Sensitive MOS Field-effect Transistor,* Appl. Phys. Lett., 1975. **26**(2): p. 55-57.
194. Lundstrom, I., M. Armgarth, and L.-G. Petersson, *Physics With Catalytic Metal Gate Chemical Sensors,* CRC Critical Reviews in Solid State and Materials Sciences, 1989. **15**(3): p. 200-278.
195. Behrisch, R. and K. Wittmaack, eds. *Sputtering by Particle Bombardment II: Characteristics of Sputtered Particles, Technical Appliations.* Tipics in Applied Physics, ed. H.K.V. Lotsch. Vol. 64. 1991, Springer_Verlag: New York, Berlin.
196. Behrisch, R., ed. *Sputtering by Particle Bombardment II: Sputtering of Alloys and Componds, Electron and Neutron Sputtering, Surface Topography.* Tipics in Applied Physics, ed. H.K.V. Lotsch. Vol. 52. 1983, Springer_Verlag: New York, Berlin.
197. Behrisch, R., ed. *Sputtering by Particle Bombardment I: Physical Sputtering of Single-Element Solids.* Topics in Applied Physics, ed. H.K.V. Lotsch. Vol. 47. 1981, Springer-Verlag: New York, Berlin.
198. Kaur, I., w. gust, and L. Kozma, *Palladium/Hydrogen Diffusion Coefficients,* in *Handbook of Grain and Interphase Boundary Diffusion Data.* 1989, Ziegler Press: Stuttgart. p. 1197.
199. Shanabarger, M.R., *Absolute Desorption Rate Measurements for H_2 Chemisorbed on Nickel,* Solid State Commun., 1974. **14**: p. 1015-1019.
200. Barrer, R.M., *Stationary and Non-stationary States of Flow of Hydrogen in Palladium and IronTrans. Faraday Soc.,* Trans. Faraday Soc., 1940. **36**: p. 1235-1248.
201. Alguero, M., *et al.*, *In situ Measurement of the Rate of H Absorption by a Pd Cathode during the Electrolysis of Aqueous Solutions,* Rev. Sci. Instrum., 1997. **68**(2): p. 1324-1330.
202. Ballantine, D.S.J., *et al.*, *Acustic Wave Sensors: Theory, Design, and Physico-Chemical Applications.* Applications of Modern Acoustics, ed. R. Stern and M. Levy. 1997, San Diego: Academic Press.
203. Adam, N.K., *The Physics and Chemistry of Surfaces.* 1968, New York: Dover Publications Inc.
204. Bruch, L.W., M.W. Cole, and E. Zaremba, *Physical Adsorption: Forces and Phenomena.* 1st ed. The International Series of Monographs on Chemistry, ed. J.S.F. Rowlinson. 1997, New York: Oxford University Press Inc.
205. Canjar, L.N. and J.A. Kostecki, *Physical Adsorption Processes and Principles.* Chemical Engineering Progress Symposium Series. Vol. 63. 1967, New York: American Institute of Chemical Engineers.
206. Dash, J.G., *Films on Solid Surfaces: The Physics and Chemistry of Physical Adsorption.* 1975, New York: Academic Press.
207. Smith, J.R., ed. *Theory of Chemisorption.* Topics in Current Physics. Vol. 19. 1980, Spring-Verlag: New York.

208. Armgarth, M. and C. Nylander, *A Stable Hydrogen-Sensitive Pd Gate Metal-Oxide Semiconduction Capacitor,* Appl. Phys. Lett., 1981. **39**(1): p. 91-92.
209. Lee, M.-W. and R. Glosser, *Pressure Concentration Isotherms of Thin Films of the Palladium-Hydrogen System as Modified by Film Thickness, Hydrogen Cycling, and Stress,* J. Appl. Phys., 1985. **57**(12): p. 5236-5239.
210. Armor, J.N., *Challenges in Membrane Catalysis,* ChemTech, 1992. **Sept.**: p. 557-563.
211. Hughes, R.C. and R. Bastasz, *Low-energy Proton Detection by Pd Metal-Insulator-Semiconductor Diodes,* J. Appl. Phys., 1988. **64**(12): p. 6839-6844.
212. Tomanek, D., S. Wilke, and M. Scheffler, *Hydrogen-Induced Polymorphism of the Pd(110) Surface,* Phys. Rev. Lett., 1997. **79**(7): p. 1329-1332.
213. Butler, M.A. and R.J. Buss, *Kinetics of the Miromirror Chemical Sensor,* Sensors and Acutators, 1993. **B**(11): p. 161-166.
214. Martinelli, G., *et al.*, *Screen-Printed Perovskite-Type Thick Films as Gas Sensors for Environmental Monitoring,* Sensors and Actuators, 1999. **B**(55): p. 99-110.
215. Poteat, T.L. and B. Lalevic, *Transition Metal-Gate MOS Gaseous Detectors,* IEEE Trans. Electron Devices, 1982. **ED-29**(1): p. 123-129.
216. Sessler, G.M., *Acoustic Sensors,* Sensors and Actuators, 1991. **A**(25-27): p. 323-330.
217. Stiblert, L. and C. Svensson, *Hydrogen Leak Detector Uisng a Pd-Gate MOS Transistor,* Rev. Sci. Instrum., 1975. **46**(9): p. 1206-1208.
218. Williams, R.A., *Handbook of The Atomic Elements.* 1970, New York: Philosophical Library.
219. Sittig, M., *Mercury,* in *Environmental Sources and Emissions Handbook,* M. Sittig, Editor. 1975, Noves Data Co.: Park Ridge, NJ. p. 88-97.
220. Johnson, D.L. and R.S. Braman, *Distribution of Atmospheric Mercury Species Near Ground,* Environ. Sci. Technol., 1974. **8**(12): p. 1003-1009.
221. Beinrohr, E., *et al.*, *Flow-thought Stripping Chronopotentiometry for the Monitoring of mercury in Waste Water,* Fresenius J. Anal. Chem., 1998. **362**: p. 201-204.
222. Battistoni, C., *et al.*, *Interaction of mercury Vapour with Thin Films of Gold,* Appl. Surf. Sci., 1996. **103**: p. 107-111.
223. Inukai, J., S. Sugita, and K. Itaya, *Underpotential Deposition of Mercury of Au(111) Investigated by insitu Scanning Tunelling Microscopy,* J. Electroan. Chem., 1996. **403**: p. 159-168.
224. Yang, X.M., *et al.*, *In-situ Observation of the Electrochemical Hg/Au amalgam Process on an Au Electrode Surface by Atomic Force Microscopy,* Surface Science, 1994. **319**: p. L17-L22.
225. Levlin, M., E. Ikavalko, and T. Laitinen, *Adsorption of Mercury on Gold and Silver Surfaces,* Fresenius J. Anal. Chem., 1999. **365**: p. 577-586.
226. Scheide, E.P. and J.K. Taylor, *Piezoelectric Sensor for Mercury in Air,* Environ. Sci. Technol., 1974. **8**(13): p. 1097-1099.
227. Braman, R.S. and D.L. Johnson, *Selective Absorption Tubes and Emission Technique for Detemination of Ambient Form of Mercury in Air,* Environ. Sci. Technol., 1974. **8**(12): p. 996-1003.
228. Castilhos, Z.C., E.D. Bidone, and L.D. Lacerda, *Increase of the Background Human Exposure to Mercury Through Fish Consumption due to Gold Mining at the Tapajos River Region, Prar State, Amazon,* Bull. Enviorn. Contam. Toxicol., 1998. **61**: p. 202-209.
229. George, M.A., *et al.*, *Electrical, Spectroscopic, and Morphological Invesitgation of Chromium Diffusion Through Gold Films,* This Solid Films, 1990. **189**: p. 59-72.
230. George, M.A., *Electrical, Spectroscopic and Morphological Investigation of Mercury Adsorption on Thin Gold Films,* in *Dept. of Chemistry* 1991, Arizona State University: Tempe, AZ.
231. Joyner, R.W. and M.W. Roberts, *Auger Electron Spectroscopy Studies of Clean Polycrystalline Gold and of the Adsorption of Mercury on Gold,* J. Chem. Soc. Faraday Trans. I, 1973. **69**: p. 1242-1250.
232. Levlin, M., *et al.*, *Evaporation of Gold Thin Films on Mica: Effect of Evaporation Parameters,* Appl. Surf. Sci., 1997. **115**: p. 31-38.
233. Nowakowski, R., *et al.*, *Atomic Force Microscopy of Au/Hg Alloy Formation on Thin Au Films,* Appl. Surf. Sci., 1997. **115**: p. 217-231.

234. Chen, C.-h. and A.A. Gewirth, *In Situ Observation of Monolayer Structures of Underpotentially Deposited Hg on Au(111) with the Atomic Force Microscope*, Phys. Rev. Lett., 1992. **68**(10): p. 157-1574.
235. Main, C. and J.M.A. Lenihan, *A Compact Mercury Vapor Concentration Meter*, J. Phys. E: Sci. Instrum., 1978. **11**: p. 1123-1124.
236. Stoney, G.G., *The Tension of Metallic Films Deposited by Electrolysis*, Proc. Royal Soc. London A, 1909. **82**: p. 172-175.
237. Ciria, M., *et al.*, *Determination of Magnetostrictive Stresses in Magnetic Rare-Earth Superlattices by a Cantilever Method*, Physical Review Letters, 1995. **75**(8, Aug. 21): p. 1634-1637.
238. Thundat, T., *et al.*, *Thermal and Ambient-Induced Deflections of Scanning Force Microscope Cantilevers*, Applied Physics Letters, 1994. **64**: p. 2894-96.
239. Langmuir, I., *The Constitution and Fundamental Properties of Solids and Liquids I. Solid*, J. Am. Chem. Soc., 1916. **38**: p. 2221-2295.
240. Langmuir, I., *The Evaporation, Condensation and Reflection of Molecules and The Mechanism of Adsorption*, Phys. Rev., 1916. **8**: p. 149-176.
241. Langmuir, I., *The Dissociation of Hydrogen Into Atoms. III. The Mechanism of the Reaction*, J. Am. Chem. Soc., 1916. **38**(6): p. 1146-1156.
242. Langmuir, I., *The Constitution and Fundamental Properties of Solids and liquids. II. Liquids*, J. Am. Chem. Soc., 1917. **39**: p. 1848-1906.
243. Langmuir, I., *The Adsorption if Gases on Plane Surfaces of Glass, Mica and Platinum*, J. Am. Chem. Soc., 1918. **40**: p. 1361-1403.
244. Morris, M.A., M. Bowker, and D. King, *Kinetics of Adsorption, Desorption and Diffusion at Metal Surfaces*, in *Comprehensive Chemical Kinetics*, C.H. Bamford, C.F.H. Tipper, and R.G. Compton, Editors. 1984, Elsevier: Amsterdam; New York. p. 1-179.
245. Tromp, R.M., *Personal Communication*, 1999.
246. Tromp, R.M., *Surface Stress and Interface Formation*, Phys. Rev. B, 1993. **47**(12): p. 7125-7127.
247. Ibach, H., *Adsorbate-induced Surface Stress*, J. Vac. Sci. Technol., 1994. **A 12**(4): p. 2240-2245.

Appendices

Appendix A

MATHCAD EVALUATION FOR A PLATE SHEET DIFFUSION

(Mathcad 8 Professional Program)

Case 1: *Hydrogen diffuses into a plant sheet when initial hydrogen concentration distribution is $C = f(x) = 0$ (when $t = 0$) in the region $0 < x < l$ and the concentrations at two surfaces are constants for all $t \geq 0$.*

Initial conditions (normalized concentration)

$C1 := 1$ for all t at x = 0

$C2 := 1$ for all t at x = l

Substrate thickness (cm) $l := 5 \cdot 10^{-6}$

Diffusion distance (cm) $x := 0, l \cdot 0.02 .. l$

Diffusion coefficient (cm^2/s) $D := 1 \cdot 10^{-7}$

Time (s) $t := 10^{-4}$

$t1 := 0.005 \cdot t;\ t2 := 0.02 \cdot t;\ t3 := 0.1 \cdot t;\ t4 := 0.25 \cdot t;\ t5 := 0.6 \cdot t;\ t6 := 1 \cdot t$

Concentration inside the palladium

$$\psi 1(x) := C1 + (C2 - C1)\cdot\frac{x}{l} + \frac{2}{\pi}\cdot\sum_{n=1}^{100}\frac{C2\cdot\cos(n\cdot\pi) - C1}{n}\cdot\sin\left(n\cdot\pi\cdot\frac{x}{l}\right)\cdot\exp\left(-D\cdot n^2\cdot\pi^2\cdot\frac{t1}{l^2}\right)$$

$$\psi 2(x) := C1 + (C2 - C1)\cdot\frac{x}{l} + \frac{2}{\pi}\cdot\sum_{n=1}^{100}\frac{C2\cdot\cos(n\cdot\pi) - C1}{n}\cdot\sin\left(n\cdot\pi\cdot\frac{x}{l}\right)\cdot\exp\left(-D\cdot n^2\cdot\pi^2\cdot\frac{t2}{l^2}\right)$$

$$\psi 3(x) := C1 + (C2 - C1)\cdot\frac{x}{l} + \frac{2}{\pi}\cdot\sum_{n=1}^{100}\frac{C2\cdot\cos(n\cdot\pi) - C1}{n}\cdot\sin\left(n\cdot\pi\cdot\frac{x}{l}\right)\cdot\exp\left(-D\cdot n^2\cdot\pi^2\cdot\frac{t3}{l^2}\right)$$

$$\psi 4(x) := C1 + (C2 - C1)\cdot\frac{x}{l} + \frac{2}{\pi}\cdot\sum_{n=1}^{100}\frac{C2\cdot\cos(n\cdot\pi) - C1}{n}\cdot\sin\left(n\cdot\pi\cdot\frac{x}{l}\right)\cdot\exp\left(-D\cdot n^2\cdot\pi^2\cdot\frac{t4}{l^2}\right)$$

$$\psi 5(x) := C1 + (C2 - C1)\cdot\frac{x}{l} + \frac{2}{\pi}\cdot\sum_{n=1}^{100}\frac{C2\cdot\cos(n\cdot\pi) - C1}{n}\cdot\sin\left(n\cdot\pi\cdot\frac{x}{l}\right)\cdot\exp\left(-D\cdot n^2\cdot\pi^2\cdot\frac{t5}{l^2}\right)$$

$$\psi 6(x) := C1 + (C2 - C1)\cdot\frac{x}{l} + \frac{2}{\pi}\cdot\sum_{n=1}^{100}\frac{C2\cdot\cos(n\cdot\pi) - C1}{n}\cdot\sin\left(n\cdot\pi\cdot\frac{x}{l}\right)\cdot\exp\left(-D\cdot n^2\cdot\pi^2\cdot\frac{t6}{l^2}\right)$$

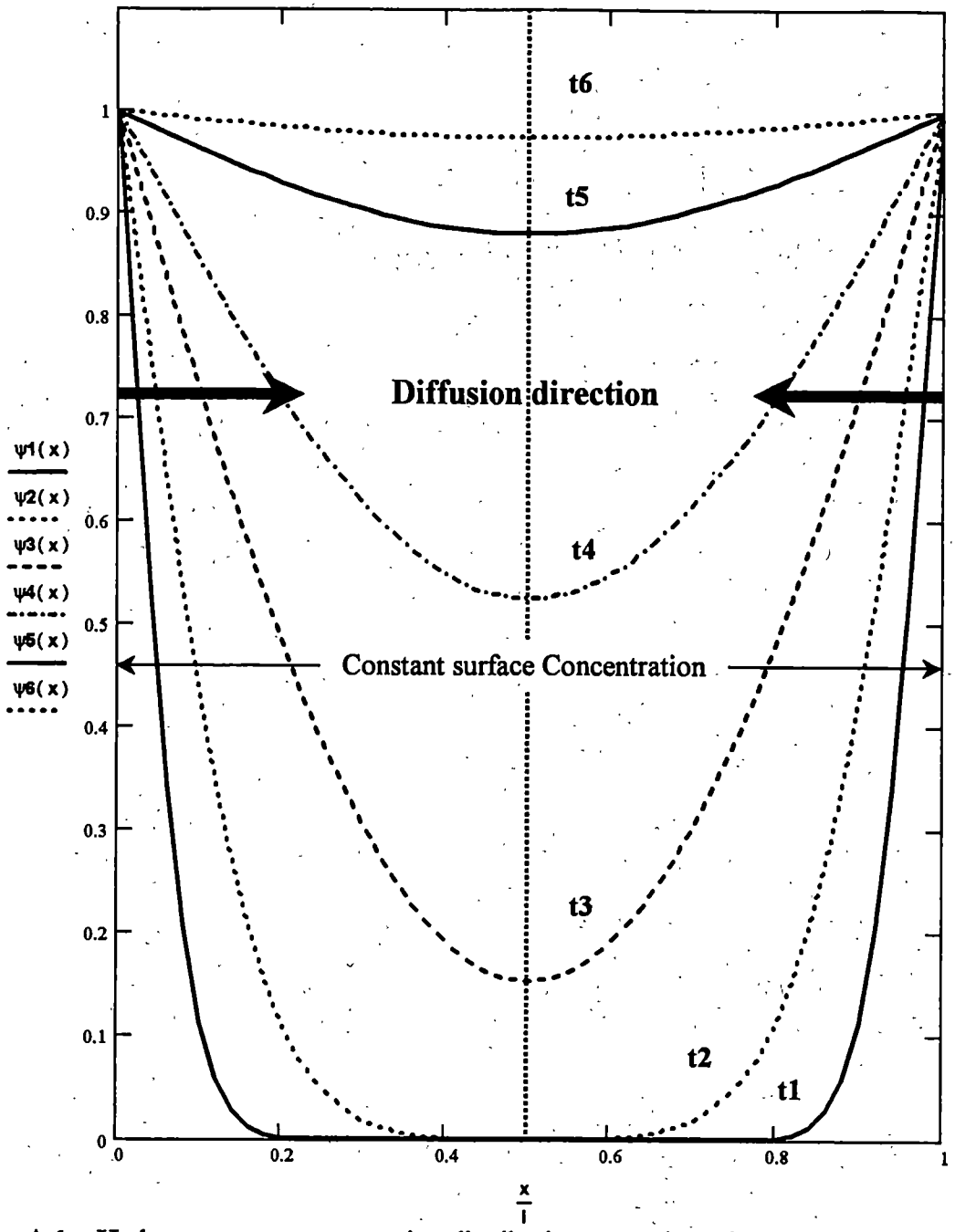


Figure A.1. Hydrogen atom concentration distributions at various times in a plate sheet. Both surfaces of the sheet have constant surface concentrations.

Case 2: *Hydrogen introduced into palladium with various concentrations on one surface and impermeable on another one; diffusion coefficient is a constant.*

If normalized concentration

$$C01 := 1;\quad C02 := 0.8;\quad C03 := 0.6;\quad C04 := 0.4;\quad C05 := 0.2;\quad C06 := 0.1$$

Substrate thickness (cm) $\quad d := 5 \cdot 10^{-6};\quad l := 10 \cdot 10^{-6}$

Diffusion distance (cm) $\quad x := l$

Diffusion coefficient (cm^2/s) $\quad D := 1 \cdot 10^{-7}$

Time (s) $\quad t := 0, 2 \cdot 10^{-5} .. 10^{-3}$

Concentration distribution inside palladium film as a function of time *t* on the impermeable surface (where *x* = *l*)

$$C1(t) := C01 \cdot \left(\frac{d}{l} + \frac{2}{\pi} \cdot \sum_{n=1}^{100} \frac{1}{n} \cdot \sin\left(n \cdot \pi \cdot \frac{d}{l}\right) \cdot \exp\left(-D \cdot n^2 \cdot \pi^2 \cdot \frac{t}{l^2}\right) \cdot \cos\left(n \cdot \pi \cdot \frac{x}{l}\right) \right)$$

$$C2(t) := C02 \cdot \left(\frac{d}{l} + \frac{2}{\pi} \cdot \sum_{n=1}^{100} \frac{1}{n} \cdot \sin\left(n \cdot \pi \cdot \frac{d}{l}\right) \cdot \exp\left(-D \cdot n^2 \cdot \pi^2 \cdot \frac{t}{l^2}\right) \cdot \cos\left(n \cdot \pi \cdot \frac{x}{l}\right) \right)$$

$$C3(t) := C03 \cdot \left(\frac{d}{l} + \frac{2}{\pi} \cdot \sum_{n=1}^{100} \frac{1}{n} \cdot \sin\left(n \cdot \pi \cdot \frac{d}{l}\right) \cdot \exp\left(-D \cdot n^2 \cdot \pi^2 \cdot \frac{t}{l^2}\right) \cdot \cos\left(n \cdot \pi \cdot \frac{x}{l}\right) \right)$$

$$C4(t) := C04 \cdot \left(\frac{d}{l} + \frac{2}{\pi} \cdot \sum_{n=1}^{100} \frac{1}{n} \cdot \sin\left(n \cdot \pi \cdot \frac{d}{l}\right) \cdot \exp\left(-D \cdot n^2 \cdot \pi^2 \cdot \frac{t}{l^2}\right) \cdot \cos\left(n \cdot \pi \cdot \frac{x}{l}\right) \right)$$

$$C5(t) := C05 \cdot \left(\frac{d}{l} + \frac{2}{\pi} \cdot \sum_{n=1}^{100} \frac{1}{n} \cdot \sin\left(n \cdot \pi \cdot \frac{d}{l}\right) \cdot \exp\left(-D \cdot n^2 \cdot \pi^2 \cdot \frac{t}{l^2}\right) \cdot \cos\left(n \cdot \pi \cdot \frac{x}{l}\right) \right)$$

$$C6(t) := C06 \cdot \left(\frac{d}{l} + \frac{2}{\pi} \cdot \sum_{n=1}^{100} \frac{1}{n} \cdot \sin\left(n \cdot \pi \cdot \frac{d}{l}\right) \cdot \exp\left(-D \cdot n^2 \cdot \pi^2 \cdot \frac{t}{l^2}\right) \cdot \cos\left(n \cdot \pi \cdot \frac{x}{l}\right) \right)$$

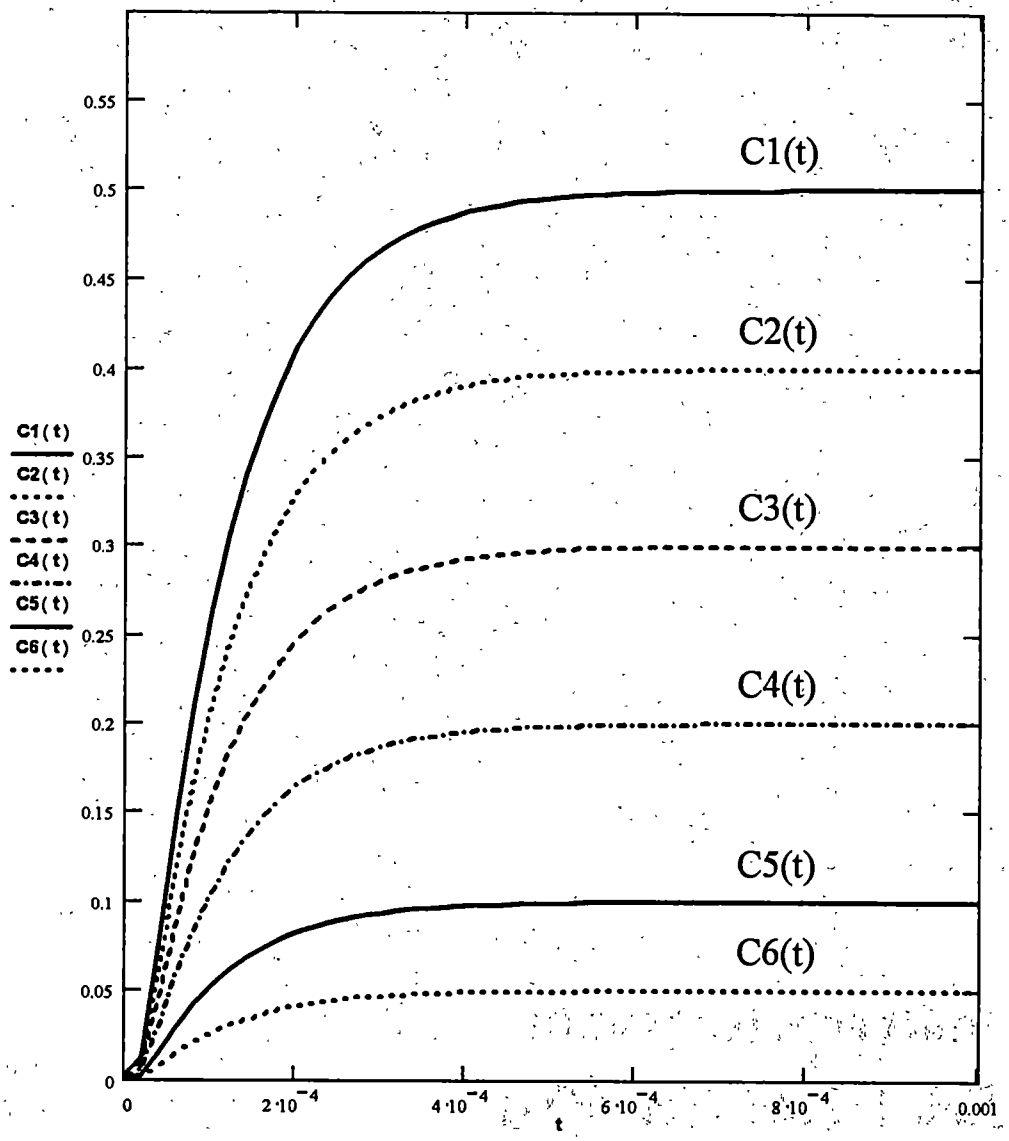


Figure A.2. Concentration distributions inside palladium film as a function of time t on the impermeable surface ($x = l$) for various concentrations at gas-solid surface ($x = d$).

Case 3: *Hydrogen adsorbs into palladium with various concentrations on one surface and impermeable on another one; diffusion coefficients vary with concentrations.*

If normalized concentration

$$C01 := 1;\quad C02 := 0.8;\quad C03 := 0.6;\quad C04 := 0.4;\quad C05 := 0.2;\quad C06 := 0.1$$

Substrate thickness (cm) $\quad d := 5 \cdot 10^{-6};\quad l := 10 \cdot 10^{-6}$

Diffusion distance (cm) $\quad x := l$

Diffusion coefficient (cm^2/s) $\quad D := 1 \cdot 10^{-7}$

If diffusion coefficient depends on hydrogen pressure (cm^2/s)

$$D1 := D;\quad D2 := 0.8 \cdot D;\quad D3 := 0.6 \cdot D;\quad D4 := 0.4 \cdot D;\quad D5 := 0.2 \cdot D;\quad D6 := 0.1 \cdot D$$

Time (s) $\quad t := 0, 2 \cdot 10^{-5} .. 4 \cdot 10^{-3}$

Concentration distribution inside palladium film as a function of time *t* on the impermeable surface (where *x* = *l*)

$$C1(t) := C01 \cdot \left(\frac{d}{l} + \frac{2}{\pi} \cdot \sum_{n=1}^{100} \frac{1}{n} \cdot \sin\left(n \cdot \pi \cdot \frac{d}{l}\right) \cdot \exp\left(-D1 \cdot n^2 \cdot \pi^2 \cdot \frac{t}{l^2}\right) \cdot \cos\left(n \cdot \pi \cdot \frac{x}{l}\right) \right)$$

$$C2(t) := C02 \cdot \left(\frac{d}{l} + \frac{2}{\pi} \cdot \sum_{n=1}^{100} \frac{1}{n} \cdot \sin\left(n \cdot \pi \cdot \frac{d}{l}\right) \cdot \exp\left(-D2 \cdot n^2 \cdot \pi^2 \cdot \frac{t}{l^2}\right) \cdot \cos\left(n \cdot \pi \cdot \frac{x}{l}\right) \right)$$

$$C3(t) := C03 \cdot \left(\frac{d}{l} + \frac{2}{\pi} \cdot \sum_{n=1}^{100} \frac{1}{n} \cdot \sin\left(n \cdot \pi \cdot \frac{d}{l}\right) \cdot \exp\left(-D3 \cdot n^2 \cdot \pi^2 \cdot \frac{t}{l^2}\right) \cdot \cos\left(n \cdot \pi \cdot \frac{x}{l}\right) \right)$$

$$C4(t) := C04 \cdot \left(\frac{d}{l} + \frac{2}{\pi} \cdot \sum_{n=1}^{100} \frac{1}{n} \cdot \sin\left(n \cdot \pi \cdot \frac{d}{l}\right) \cdot \exp\left(-D4 \cdot n^2 \cdot \pi^2 \cdot \frac{t}{l^2}\right) \cdot \cos\left(n \cdot \pi \cdot \frac{x}{l}\right) \right)$$

$$C5(t) := C05 \cdot \left(\frac{d}{l} + \frac{2}{\pi} \cdot \sum_{n=1}^{100} \frac{1}{n} \cdot \sin\left(n \cdot \pi \cdot \frac{d}{l}\right) \cdot \exp\left(-D5 \cdot n^2 \cdot \pi^2 \cdot \frac{t}{l^2}\right) \cdot \cos\left(n \cdot \pi \cdot \frac{x}{l}\right) \right)$$

$$C6(t) := C06 \cdot \left(\frac{d}{l} + \frac{2}{\pi} \cdot \sum_{n=1}^{100} \frac{1}{n} \cdot \sin\left(n \cdot \pi \cdot \frac{d}{l}\right) \cdot \exp\left(-D6 \cdot n^2 \cdot \pi^2 \cdot \frac{t}{l^2}\right) \cdot \cos\left(n \cdot \pi \cdot \frac{x}{l}\right) \right)$$

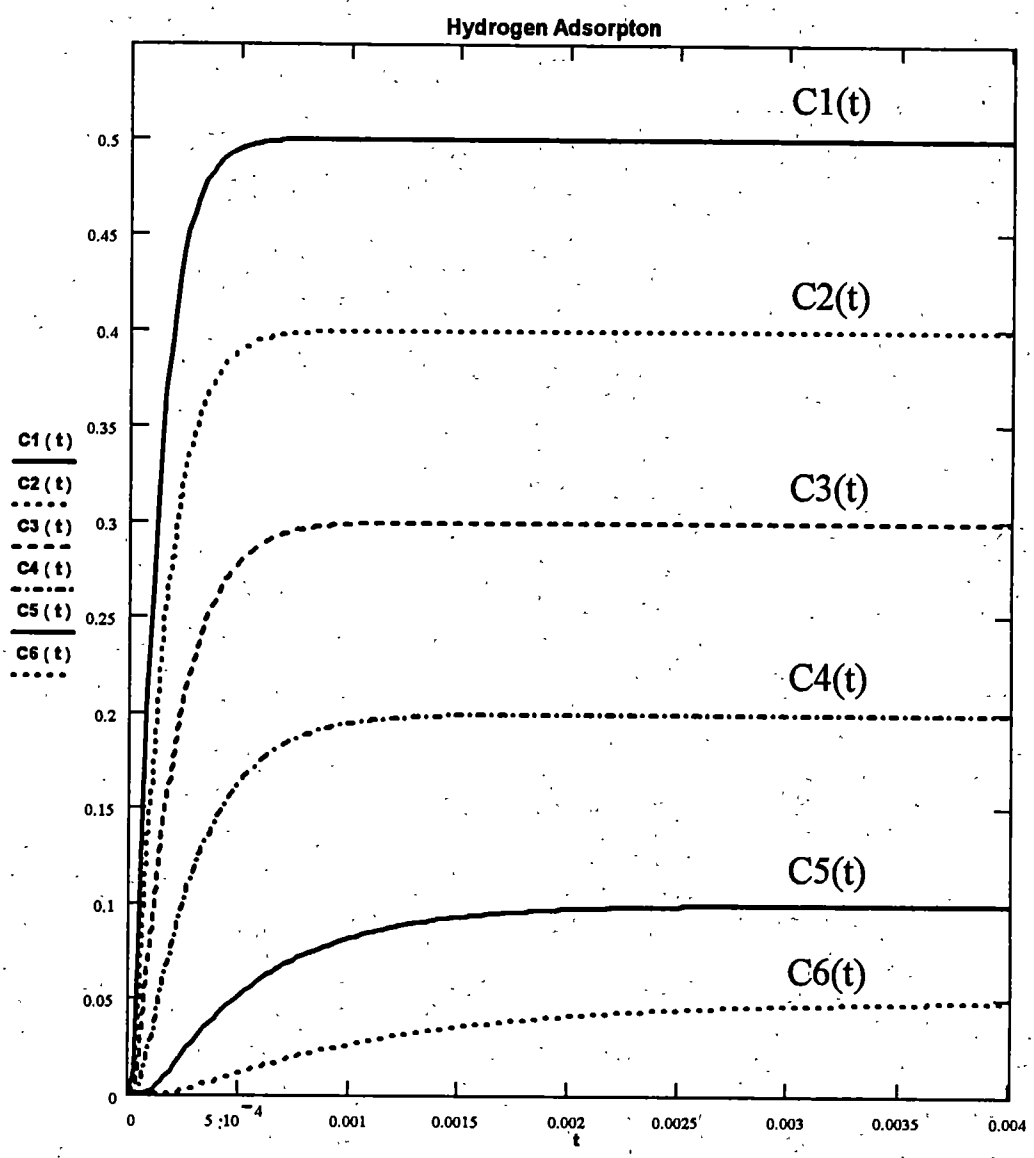


Figure A.3. Hydrogen introduced into palladium when diffusion coefficients vary with concentrations. Notice the lower diffusion coefficient is, the longer time needed to reach equilibrium position.

Case 4: *Hydrogen desorbs from palladium with various concentrations at one surface and impermeable on another one; diffusion coefficient is a constant.*

If normalized concentration

$$C01 := 1;\quad C02 := 0.8;\quad C03 := 0.6;\quad C04 := 0.4;\quad C05 := 0.2;\quad C06 := 0.1$$

Substrate thickness (cm) $\quad d := 5\cdot 10^{-6};\quad l := 10\cdot 10^{-6}$

Diffusion distance (cm) $\quad x := l$

Diffusion coefficient (cm^2/s) $\quad D := 1\cdot 10^{-7}$

If diffusion coefficient depends on hydrogen pressure (cm^2/s)

$$D1 := D;\quad D2 := 0.8\cdot D;\quad D3 := 0.6\cdot D;\quad D4 := 0.4\cdot D;\quad D5 := 0.2\cdot D;\quad D6 := 0.1\cdot D$$

Time (s) $\quad t := 0, 2\cdot 10^{-5} .. 3\cdot 10^{-3}$

Concentration inside the palladium (evolution process) film as a function of time *t* on the impermeable surface (where *x* = *l*)

$$Cd1(t) := \frac{C01}{2} - C01\cdot\left(\frac{d}{l} + \frac{2}{\pi}\cdot\sum_{n=1}^{100}\frac{1}{n}\cdot\sin\left(n\cdot\pi\cdot\frac{d}{l}\right)\cdot\exp\left(-D1\cdot n^2\cdot\pi^2\cdot\frac{t}{l^2}\right)\cdot\cos\left(n\cdot\pi\cdot\frac{x}{l}\right)\right)$$

$$Cd2(t) := \frac{C02}{2} - C02\cdot\left(\frac{d}{l} + \frac{2}{\pi}\cdot\sum_{n=1}^{100}\frac{1}{n}\cdot\sin\left(n\cdot\pi\cdot\frac{d}{l}\right)\cdot\exp\left(-D2\cdot n^2\cdot\pi^2\cdot\frac{t}{l^2}\right)\cdot\cos\left(n\cdot\pi\cdot\frac{x}{l}\right)\right)$$

$$Cd3(t) := \frac{C03}{2} - C03\cdot\left(\frac{d}{l} + \frac{2}{\pi}\cdot\sum_{n=1}^{100}\frac{1}{n}\cdot\sin\left(n\cdot\pi\cdot\frac{d}{l}\right)\cdot\exp\left(-D3\cdot n^2\cdot\pi^2\cdot\frac{t}{l^2}\right)\cdot\cos\left(n\cdot\pi\cdot\frac{x}{l}\right)\right)$$

$$Cd4(t) := \frac{C04}{2} - C04\cdot\left(\frac{d}{l} + \frac{2}{\pi}\cdot\sum_{n=1}^{100}\frac{1}{n}\cdot\sin\left(n\cdot\pi\cdot\frac{d}{l}\right)\cdot\exp\left(-D4\cdot n^2\cdot\pi^2\cdot\frac{t}{l^2}\right)\cdot\cos\left(n\cdot\pi\cdot\frac{x}{l}\right)\right)$$

$$Cd5(t) := \frac{C05}{2} - C05\cdot\left(\frac{d}{l} + \frac{2}{\pi}\cdot\sum_{n=1}^{100}\frac{1}{n}\cdot\sin\left(n\cdot\pi\cdot\frac{d}{l}\right)\cdot\exp\left(-D5\cdot n^2\cdot\pi^2\cdot\frac{t}{l^2}\right)\cdot\cos\left(n\cdot\pi\cdot\frac{x}{l}\right)\right)$$

$$Cd6(t) := \frac{C06}{2} - C06\cdot\left(\frac{d}{l} + \frac{2}{\pi}\cdot\sum_{n=1}^{100}\frac{1}{n}\cdot\sin\left(n\cdot\pi\cdot\frac{d}{l}\right)\cdot\exp\left(-D6\cdot n^2\cdot\pi^2\cdot\frac{t}{l^2}\right)\cdot\cos\left(n\cdot\pi\cdot\frac{x}{l}\right)\right)$$

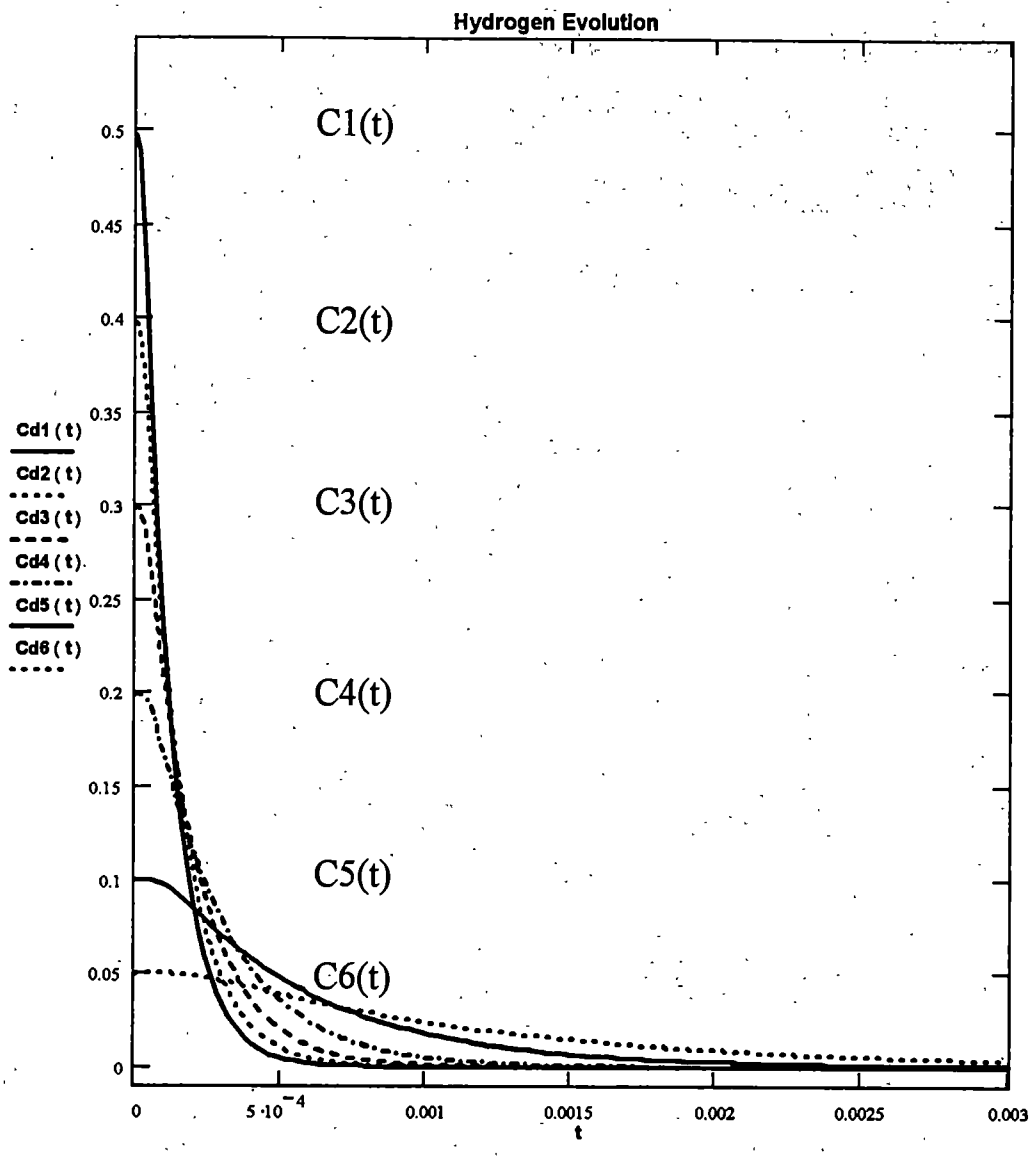


Figure A.4. Hydrogen diffusion-out palladium when diffusion coefficients vary with concentrations. Notice same as diffusion-in process, the lower diffusion coefficient is, the longer time needed to reach equilibrium position

Appendix B

CALCULATION OF CANTILEVER BEAM NATURAL FREQUENCY

In this appendix the vibration resonance frequency of a distributed-mass rectangular cantilever beam with a concentrated mass is determined. The beam has a total mass m_b and length L. The flexural rigidity of the beam is EI and the concentrated mass at its end is m, as shown in Figure B.1(a).

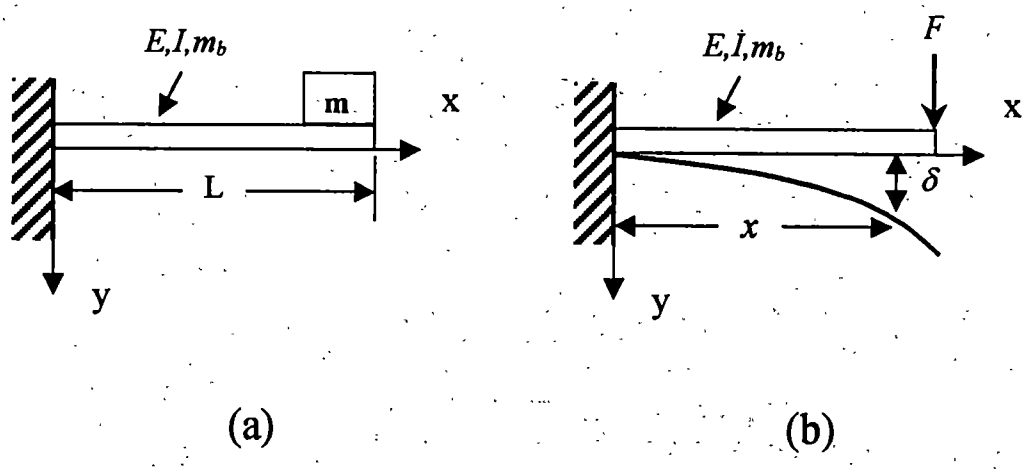


Figure B.1: Cantilever deflection. (a) Cantilever beam of uniform mass with a mass concentrated at its tip. (b) Assumed deflection curve.

Assuming the shape of deflection curve of the beam is that of the beam acted upon by a concentrated force F applied at the free end as shown in Figure B.1(b). For this static load the deflection at a distance x from the support is

$$\delta = \frac{3y}{L^3}\left(\frac{Lx^2}{2} - \frac{x^3}{6}\right), \tag{B.1}$$

where y = *deflection* at the free end of the beam. Upon substitution into eq.(B.1) of $y = C \sin(\omega t + \alpha)$, which is the harmonic deflection of the free end, we obtain

$$\delta = \frac{3x^2L - x^3}{2L^3} C \sin(\omega t + \alpha). \tag{B.2}$$

The potential energy is equated to the work done by the force $F = ma = m\ddot{y}$ as it gradually increases from zero to the final value F. This work is equal to $\frac{1}{2}Fy$, and its maximum value that is equal to the maximum potential energy is then

$$V_{\max} = \frac{1}{2}FC = \frac{3EI}{2L^3}C^2, \tag{B.3}$$

since the force F is related to the maximum deflection by the formula from elementary strength of materials,

$$y_{\max} = C = \frac{FL^3}{3EI}. \tag{B.4}$$

The kinetic energy due to the distributed mass of the beam is given by

$$T = \int_0^L \frac{1}{2}\left(\frac{m_b}{L}\right)\dot{\delta}^2 \, dx, \tag{B.5}$$

and using eq.(B.2) the maximum value for total kinetic energy will then by

$$T_{\max} = \frac{m_b}{2L}\int_0^L \left(\frac{3x^2L - x^3}{2L^3}\omega C\right)^2 dx + \frac{m}{2}\omega^2 C^2. \tag{B.6}$$

After integrating eq.(B.6) and equating it with eq.(B.3), we obtain

$$\frac{3EI}{2L^3}C^2 = \frac{1}{2}\omega^2 C^2\left(m + \frac{33}{140}m_b\right), \tag{B.7}$$

and the resonance frequency becomes

$$f = \frac{\omega}{2\pi} = \frac{1}{2\pi}\sqrt{\frac{3EI}{L^3(m + \frac{33}{140}m_b)}}. \qquad \text{(B.8)}$$

This can be approximated as:

$$f \approx \frac{1}{2\pi}\sqrt{\frac{3EI}{L^3(m + 0.24m_b)}}. \qquad \text{(B.9)}$$

The approximation given by eq.(B.9) is still good when $m = 0$ and the errors are within 1.5% compared to the exact solution (Eq. B.8).

Appendix C

MICROCANTILEVER DATA SHEET

(The two cantilevers listed here were purchased from Park Scientific Instruments, CA)

C.1 Ultralevers (Maximum Resolution Cantilevers)

- Silicon cantilever with silicon conical tip.
- Sharp, high aspect ratio tip.
- Four different cantilevers on every chip.
- Gold coated for high reflectivity.
- Boron doped silicon, 0.001 ohm/cm
- Wide range of spring constants.
- Available for tipless cantilever.

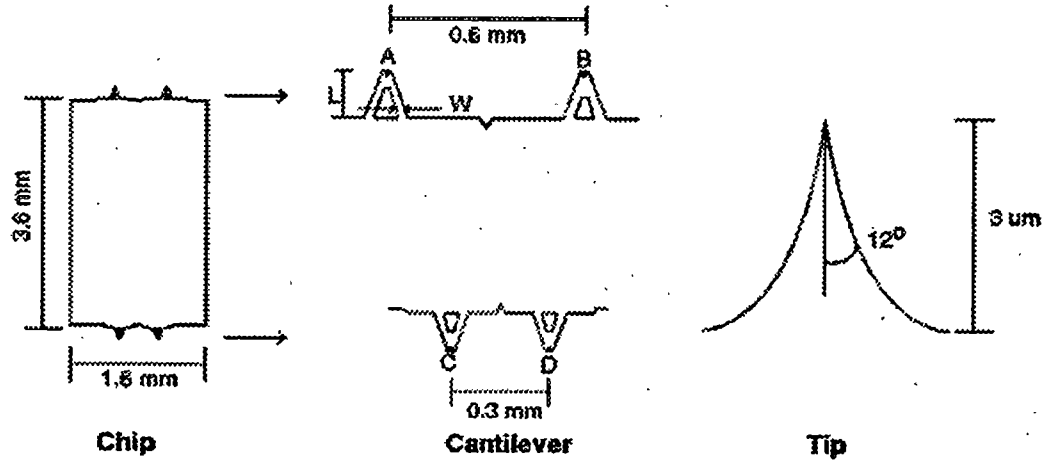


Figure C.1: Ultralever Diagram.

Table C.1: Ultralever Properties

Cantilever Type	A	B	C	D
Length (μm)	180	180	85	85
Width (μm)	25	38	18	28
Thickness (μm)	1	1	1	1
Force Constant (N/m)	0.26	0.40	1.6	2.1
Resonant Frequency (kHz)	40	45	140	160
Deflection Sensitivity* (nm/V)	88.8	74.9	62.0	63.9

C.2 Microlevers (General Purpose Cantilevers)

- Silicon Nitride (Si_3N_4) cantilever.
- Typical radius of curvature of the tip: ~ 50 nm (Microlevers), ~ 20 nm (Sharpened Microlevers).
- Six different cantilevers on every chip.
- Gold coated for high reflectivity.
- Recessed corners for easy sample approach.
- Wide range of spring constants.

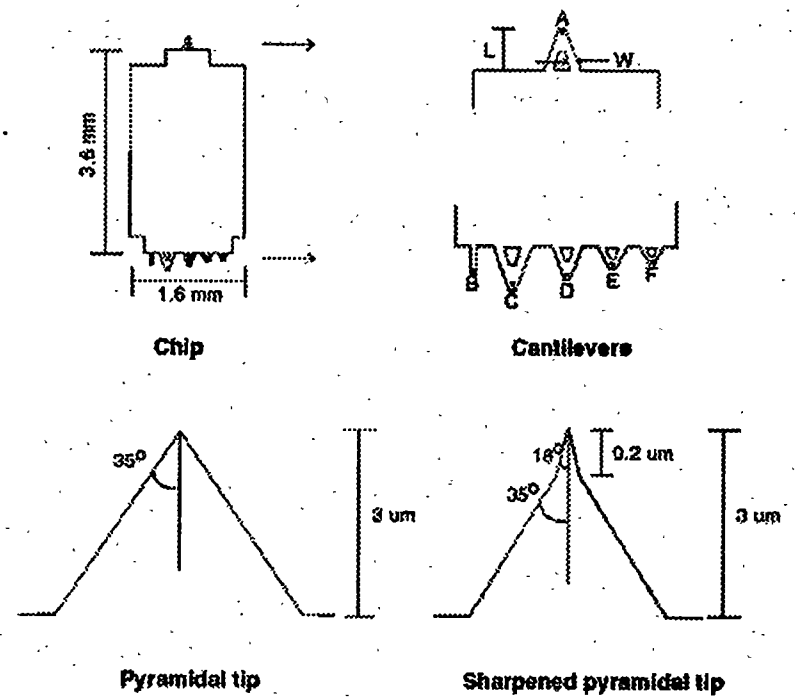


Figure C.2: Microlever Diagram.

Table C.2: Microlever Properties

Cantilever Type	A	B	C	D	E	F
Length (μm)	180	200	320	220	140	85
Width (μm)	18	20	22	22	18	18
Thickness (μm)	0.6	0.6	0.6	0.6	0.6	0.6
Force Constant (N/m)	0.05	0.02	0.01	0.03	0.10	0.50
Resonant Frequency (kHz)	22	15	7	15	38	120
Deflection Sensitivity* (nm/V)	--	48.8	90.5	68.6	48.6	31.1

* Measured in our laboratory using NanoScope III (Digital Instrument, CA).

Appendix D

MUMPS MICROCANTILEVER AND READOUT SYSTEM

There were many different types of surface micromachined cantilevers tested at Oak Ridge National Laboratory (ORNL). These were done on test chips from several different MUMPS fabrication runs in 1997 and 1999 including MUMPS17, MUMPS18, MUMPS20, MUMPS22 and MUMPS24. The results described in this thesis are for microcantilevers fabricated on the MUMPS22 and MUMPS24 runs. The dimensions of MUMPS22 and MUMPS22 are identical and they are listed in Table D.1. Over the various runs many different types and sizes of cantilevers were fabricated and tested. The layout of these cantilevers was done using the integrated circuit layout program MAGIC.

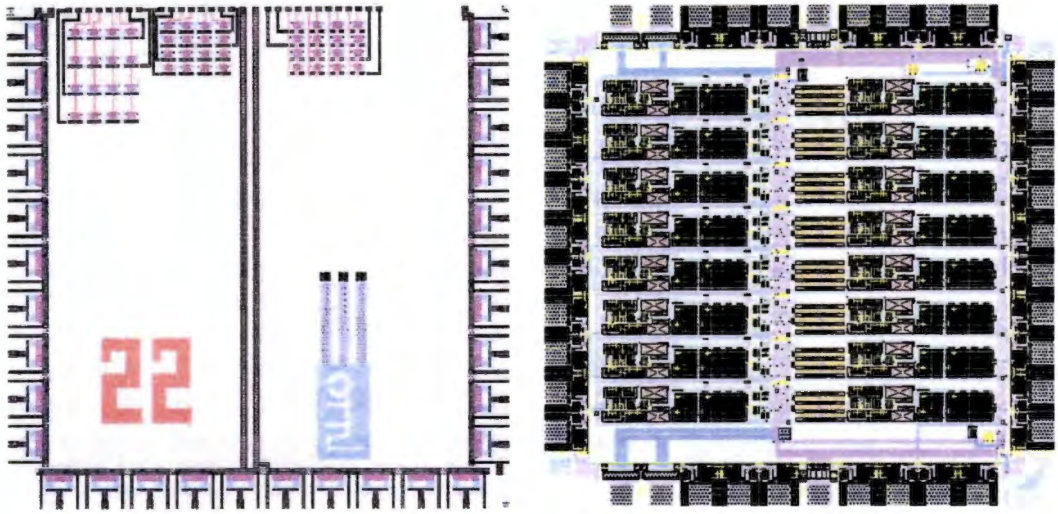
Table D.1: Dimensions of MUMPS Cantilever

	Length	Width
Cantilever Plate	112 μm	500 μm
Reflective Ears	40 μm	35 μm
Legs	150 μm	100 μm
Anchor	40 μm	500 μm

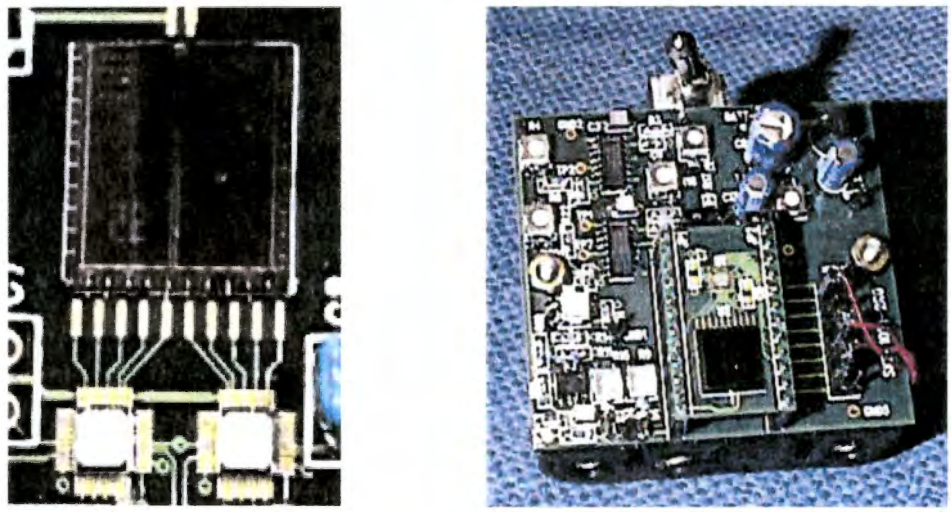
MAGIC enables the user to draw each individual layer of the desired design. Each of these layers is represented on a screen by a different color. The software is then capable of taking the designer's layout and generating a file, containing all the

layout information. This file is then used to determine all the processing steps and masks needed to produce the desired design.

Figure D.1(a) is a photograph of MUMPS22 cantilever chip. The chip is 1 cm square with 10 cantilevers on three sides. The cantilevers at the bottom of the chip were used for testing. The input drive signals come from the opposite side of the chip to minimize parasitic coupling of the drive signal into the cantilever output. A photograph of the readout chip from the MUMPS chips is shown in Figure D.1(b). Each readout chip contains eight-channel readout circuits. As we were in the testing period and modifications were always needed after each test. Normally, we only used one MUMPS chip with one readout chip for our tests. Therefore, we were capable to monitor up to eight MUMPS microcantilevers simultaneously. By adding more readout chips on the circuit board, we can test more cantilevers on the MUMPS chip. Shown in Figure D.1(c), two readout chips were connected to one side of a MUMPS 22 chip and signals were readable from all ten cantilevers on that side. Entire unit can easily fit into ones palm, and four AA-size batteries were used to power the whole circuit board (including MUMPS chip, readout chip and test boards). After attached a RF circuit board, detection signals from the MUMPS microcantilevers can be wirelessly transmitted and we have successfully conducted a four-channel wireless test in our laboratory.



(a) (b)



(c) (d)

Figure D.1: MUMPS chip and readout circuit. (a) MUMPS microcantilever arrays (10 microcantilever on each three sides); (b) 8-channel signal readout chip; (c) MUMPS chip mounted on the circuit board; (d) palm-size test unit powered by 4-AA batteries.

Appendix E

PROPERTIES OF PALLADIUM, HYDROGEN, MERCURY AND GOLD

Table E.1: Properties of Palladium, Hydrogen, Mercury and Gold*

Element	Palladium	Hydrogen	Mercury	Gold
Principal Quantum No.	5	1	6	6
Atomic No.	46	1	80	79
Atomic Wt.	106.14	1.00797	200.59	196.967
X-Ray Notation	Q	K	P	P
Group	VIII A	1 A	II B	I B
Category	Heavy transitional metal	Gas	Heavy transitional metal	Heavy transitional metal
State	Solid	Gas	Liquid	Solid
Valence	+ 2; + 4	+ 1; - 1	+ 1; + 2	+ 1; + 2; + 3
Atomic Radius	1.37 Å	--	1.57 Å	1.44 Å
Covalent Radius	--	0.37 Å	1.49 Å	1.50 Å
Ionic Radius	0.50 Å	2.08 Å (- 1)	1.10 Å (+ 2)	1.37 Å (+ 1)
Atomic Vol.	8.9 W/D	14.1 W/D	14.8 W/D	10.2 W/D
Valence Electrons	$4d^{10}$	$1s^1$	$6s^2$ (+ 2)	$6s^1$ (+ 1)
Core	Krypton	--	Krypton	Amphoteric
Density	12.0 g/ml	0.071 g/ml	13.6 g/ml	19.3 g/ml
Crystal Structure	FCC	Hexagonal	Rhombohedral	FCC
Electro-negativity	2.2	2.1	1.9	2.4
Electrical Conductance	0.093 μohm	--	0.011 μohm	0.42 μohm
First Ionization Energy	192 kcal/g-mole	313 kcal/g-mole	241 kcal/g-mole	213 kcal/g-mole
Ionization Potential	8.3 eV	13.6 eV	10.4 eV	9.2 eV
Boiling Point	3980 °C	- 252.7 °C	357 °C	2970 °C
Melting Point	1552 °C	- 259.2 °C	- 38.4 °C	1063 °C
Electronic configuration	$1s^2 2s^2 2p^6 3s^2 3p^6 3d^{10} 4s^2 4p^6 4d^{10}$	$1s^1$	$(Pd) 4f^{14} 5s^2 5p^6 5d^{10} 5f^0 5g^0 6s^2$	$(Pd) 4f^{14} 5s^2 5p^6 5d^{10} 5f^0 5g^0 6s^1$

*Listed data obtained from *Handbook of The Atomic Elements* by R. A. Williams, Philosophical Library, New York, 1970.

Appendix F

SURFACE ADSORPTION MODEL

F.1 Surface Adsorption Model

Based on above known phenomena and our observations, we propose a model for the surface adsorption mechanism that can be applied for the mercury vapor adsorption on the gold surface. There have been several adsorption models were introduced since Langmuir proposed his model for gas adsorption in 1910s. However, all these models have their limitations and cannot be directly used to explain our mercury/gold system without modifications. Considering the particular system we have here, we propose a surface adsorption model based on the following assumptions. In our model, mercury is the adsorbate (in vapor) and gold is the adsorbent (substrate). The assumptions for our model include the following terms:

1. When an adsorbate atom arrives at an acceptable site on the adsorbent surface, it has a sticking coefficient of one (100% adsorption).
2. Adsorbate atoms only adsorb on the top layer of adsorbent surface.
3. Once adsorbate atoms are adsorbed (trapped) on the adsorbent surface, they remain fixed.
4. Adsorbate atoms only simply sit on the top or the side of adsorbent atoms with no other interactions between them.

5. Only one adsorbent atom can associate with one adsorbate atom (one adsorption site per atom).
6. If a particular (adsorbent) position is already occupied by one adsorbate atom, the same position cannot be occupied by another adsorbate atom.
7. If an adsorbate atom arrives to a position that has already been occupied by another adsorbate atom, it will be reflected back to vapor or it will replace the occupied atom and send the occupied atom back to ambient.
8. Once one monolayer of adsorbate atoms is formed on the adsorbent surface, no additional adsorption can take place on that surface.

F.2 Surface Rejection Coefficient

According to our assumptions, the adsorbent surface rejection factor $J(t)$ actually is the possibility that an adsorbate atom arrives at a occupied site. $J(t)$ is equal to the ratio of the occupied sites $N_{occupied}$ at that time divided by the total acceptable positions N_{Stotal} on the adsorbent surface as

$$J(t) = \frac{N_{occupied}}{N_{Stotal}} . \qquad \text{(F.1)}$$

As mentioned in the Chapter 5, it is necessary to consider the adsorption history in order to determine the occupied positions $N_{occupied}$. If we have a non-steady flow and variable (vapor) concentrations, the number of the arriving adsorbate atoms $N_{arrive}^{(m)}$ is different and its value depends on the flow rate and (vapor) concentration. If

we have a steady flow and constant (vapor) concentration, the number of the arriving adsorbate atom $N_{arrive}^{(m)}$ is a constant, $N_{arrive}^{(m)} = N_0$, during each unit time t_0. Then we can evaluate Eq. (F.2) further. Consider the following events during an accumulation time t:

$1^{st}\ t_0,\quad t = t_0,\quad N_{occupied}^{(1)} = N_0;$

$2^{nd}\ t_0,\quad t = 2t_0,\quad N_{occupied}^{(2)} = (1 - \frac{N_{occupied}^{(1)}}{N_{Stotal}})N_0;$

$3^{rd}\ t_0,\quad t = 3t_0,\quad N_{occupied}^{(3)} = (1 - \frac{N_{occupied}^{(1)} + N_{occupied}^{(2)}}{N_{Stotal}})N_0;$

$4^{th}\ t_0,\quad t = 4t_0,\quad N_{occupied}^{(4)} = (1 - \frac{N_{occupied}^{(1)} + N_{occupied}^{(2)} + N_{occupied}^{(3)}}{N_{Stotal}})N_0;$

$\vdots \qquad\qquad \vdots$

$\vdots \qquad\qquad \vdots$

$m^{th}\ t_0,\quad t = mt_0,\quad N_{occupied}^{(m)} = (1 - \frac{N_{occupied}^{(1)} + N_{occupied}^{(2)} + \cdots + N_{occupied}^{(m)}}{N_{Stotal}})N_0;$

where $N_{occupied}^{(i)}$ is the accumulated atoms during the i^{th} unit time. Therefore, after a total of m-time accumulations, the total adsorbed atoms (occupied positions) $N_{occupied}$ is equal to

$$N_{occupied} = N_{occupied}^{(1)} + N_{occupied}^{(2)} + N_{occupied}^{(3)} + \cdots + N_{occupied}^{(m)}$$

$$= [m - \frac{(m-1)N_{occupied}^{(1)} + (m-2)N_{occupied}^{(2)} + \cdots + N_{occupied}^{(m)}}{N_{Stotal}}]N_0 \qquad \text{(F.2)}$$

Or
$$N_{occupied} = [m - \frac{\sum_{i=1}^{m-1}(m-i)N_{occupied}^{(i)}}{N_{Stotal}}]N_0 \quad \text{(F.3)}$$

Substituting Eq.(F.3) into Eq. (F.1), for m-time accumulations the adsorbent surface rejection factor $J(t)$ is equal to

$$J(t)^{(m)} = [m - \frac{\sum_{i=1}^{m-1}(m-i)N_{occupied}^{(i)}}{N_{Stotal}}]\frac{N_0}{N_{Stotal}} \quad \text{(F.4)}$$

If we use integration to replace the sum in Eq. (F.4), and rewrite Eq. (F.1) as

$$J(T_{total}) = \frac{AT_{total}}{1 + AT_{total}}, \quad \text{(F.5)}$$

where $A = \frac{N_0}{N_{Stotal}}$ and T_{total} is the total exposure time. Since A is a constant for a given concentration and flow rate, at beginning $T_{total} = 0$ then $J(T_{total}) = 0$. After a gold surface is exposed to mercury vapor for long time ($AT_{total} >> 1$), then $J(T_{total}) \approx 1$. The surface rejection coefficient $J(T_{total})$ as a function of the total exposure time T_{total} is plotted in Figure F.1 in which $A = 0.05$ per unit time t_0.

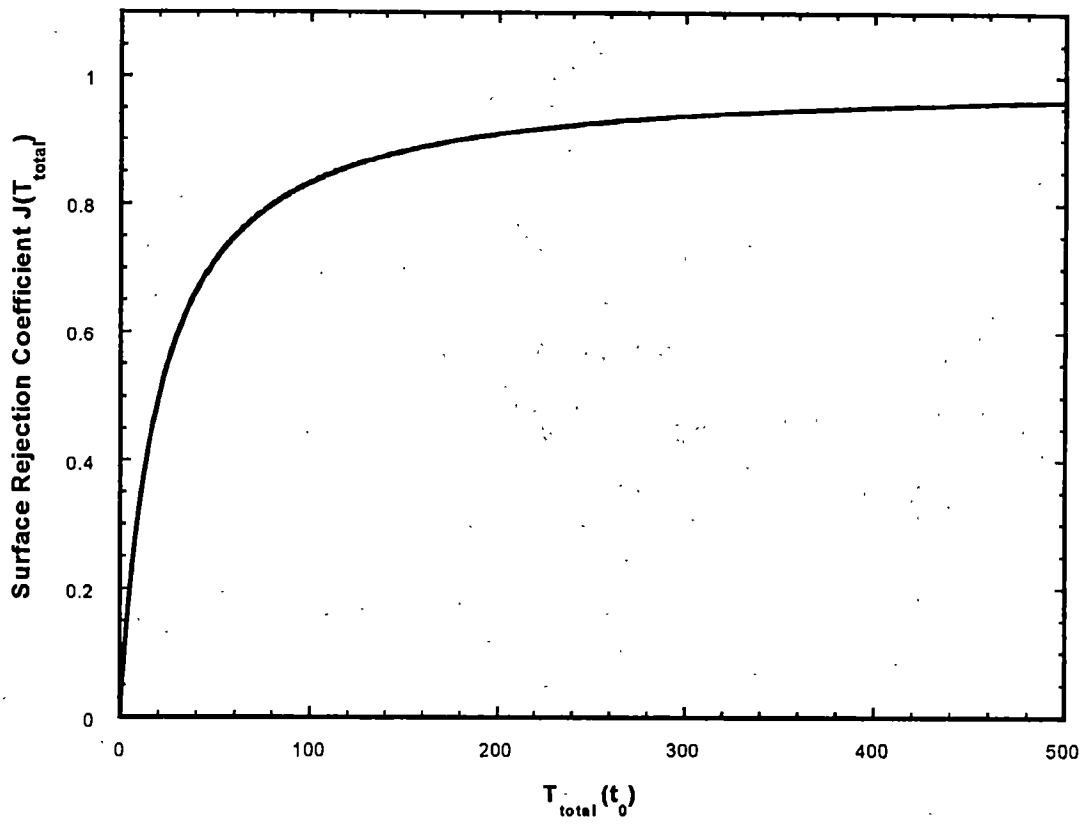


Figure F.1: Surface Rejection coefficient vs. the total exposure time ($A = 0.05$ per unit time t_0)

VITA

Zhiyu (Jerry) Hu was born in Kunming, China on June 30, 1965: He graduated from the Department of Physics at Yunnan University with a Bachelor of Sciences degree, in 1986. After serving as an instructor in the Laboratory of Electron Microscopy at Kunming Institute of Technology for four years, he came to the United States in and worked as a researcher in the Department of Molecular Physiology and Biophysics at the University of Virginia. In September 1993, he enrolled in the Physics Department of Fisk University where he was awarded the Master of Arts degree in Physics in 1995. In the same year he came to the University of Tennessee Knoxville to continue his graduate education. He received the Doctor of Philosophy in Physics in May 2000.